VASCULAR CHANGES IN TYPE 2 DIABETES MELLITUS: APPLICATION TO RESTENOSIS AFTER STENTING

Hongfeng Wang
Marquette University

VASCULAR CHANGES IN TYPE 2 DIABETES MELLITUS: APPLICATION TO RESTENOSIS AFTER STENTING

By

Hongfeng Wang, M.S., D.V.M.

A Dissertation submitted to the Faculty of the Graduate School,
Marquette University,
in Partial Fulfillment of the Requirements for
the Degree of Doctor of Philosophy

Milwaukee, Wisconsin

May 2013

ABSTRACT
VASCULAR CHANGES IN TYPE 2 DIABETES MELLITUS: APPLICATION TO RESTENOSIS AFTER STENTING

Hongfeng Wang, M.S., D.V.M.

Marquette University, 2013

Stents used to decrease cardiovascular risk in patients with type 2 diabetes mellitus (T2DM) are prone to increased rates of restenosis. The mechanisms are incompletely elucidated, but low wall shear stress (WSS) and altered intracellular signaling likely contribute. We tested the hypothesis that neointimal hyperplasia (NH) after bare-metal stenting is due to vascular remodeling (enhanced formation of advanced glycation end-products (AGEs), increased downstream vascular resistance (DVR), and decreased WSS), and that decreasing AGEs with ALT-711 (Alagebrium) mitigates this response.

Stents were implanted into the abdominal aorta of Zucker lean (ZL), obese (ZO), and diabetic (ZD) rats. After 21 days, the stented region was sectioned for NH quantification or casted and imaged for regional estimation of WSS and local intrastrut WSS by computational fluid dynamics. The thoracic and abdominal aorta, carotid, iliac, femoral and arterioles in cremaster muscle were harvested to detect AGEs related collagen cross-linking, and protein expression including transforming growth factor beta (TGFβ) and receptor for AGE (RAGE).

A trend toward elevated DVR was observed, whereas blood flow (BF) and intrastrut TAWSS were significantly decreased in ZD compared to ZL and ZO rats (eg. TAWSS: 14.5 ± 1.9 vs 30.6 ± 1.6 and 25.4 ± 2.2 dyn/cm^2, respectively; mean±SEM $P<0.05$). Intrastrut NH was increased in ZO but not ZD rats. ALT-711 reduced DVR in ZD rats (15.6±2.5x10^5 to 8.39±0.6x10^5 dyn·s/cm^5), while decreasing NH (ZL: 7.7±1.0 to 4.3±0.9%; ZO: 12.0±1.5 to 4.9±0.8%; ZD: 9.4±0.7 to 3.7±0.4%) and causing similar regional TAWSS results in all groups. AGEs related collagen cross-linking was elevated in the arterioles of ZD rats, but alleviated by ALT-711. No consistent differences in RAGE or TGFβ expression were observed in treated versus untreated rats.

Remodeling of the distal vasculature appears to play an important role in modulating WSS in T2DM, but WSS alone does not predict NH response as observed under normoglycemia. ALT-711 led to similar values for AGEs related arteriolar collagen cross-linking, BF through the stent, and regional WSS, while decreasing NH in all rats. Although TGFβ and RAGE expression did not appear to be modified by ALT-711, other intracellular signaling pathways remain to be explored.

ACKNOWLEDGMENTS

Hongfeng Wang, M.S., D.V.M.

This work is dedicated to my family: Lu Li, Lucas Wang (2 years old), and William Wang (6 months) who gave me lots of support during my research. In addition, I want to thank my parents, Xueqin Chen and Haiqing Wang, for their kindness and for supporting my studies and research. I would not be where I am today without their support and understanding all these years. I want to especially thank my mother-in-law, Qingxia Xu, and my mother who helped take care of my children so that I could devote the necessary time to my studies and research. Their kindness and patience served as a model for me of how to nurture the next generation of potential scientists and engineers.

I would like to extend my sincere appreciation to my graduate mentor, Dr. John LaDisa. I encountered numerous challenges during my graduate project. Dr. LaDisa put a lot of effort into this project. He patiently demonstrated surgical details to me, and even made a special visit to Germany to learn the stent deploying technique used with our research, which he then taught to me. During my education, I learned surgical techniques, animal monitoring, post-surgical care, and data acquisition and analysis. Besides my project, I have built models for other projects including those with data from human Marfan and diabetic patients. Through this process, I had the opportunity to learn several software tools under his guidance including Cygwin, Simvascular, Matlab and SolidWorks. Beyond teaching me best practices pertaining to research, Dr. LaDisa also spent a tremendous amount of time with me in an effort improve my writing in a way that

clearly demonstrates the findings of this dissertation as a scientific paper. During our five years closely working together, Dr. LaDisa inspired me with his critical thinking, curiosity related to new ideas, and active working ethics. To me, Dr. LaDisa is not only a mentor, but also a close friend.

I also sincerely appreciated the time and effort of my committee members, Drs. Jeffrey Toth, Judy Kersten, Said Audi, and Thomas Eddinger. Without their guidance during the past five years, this project would not have been successful. For example, when our microtome was broken, Dr. Toth allowed me to bring it to his laboratory and provided other equipment and solutions for completing quantification of neointimal hyperplasia Dr. Toth was very kind and warmhearted during our interactions, always willing to offer technical advice, show me new software packages, and offer ideas to solve problems pertaining to histology. Dr. Judy Kersten put lots of effort into organizing this project through the American Diabetes Association grant from which it started, as well as in helping to analyze and interpret the data. Dr. Eddinger allowed me to test different antibodies for use in Western blotting and helped me to analyze the protein expression results. Dr. Audi helped to reinforce my understanding of the biomedical engineering aspects of the project.

This work is also largely dependent on collaboration from colleagues in different laboratories. I want specially thank Dr. Dorothee Weihrauch, John Tessmer and David Schwabe in Anesthesiology Research at Medical College of Wisconsin. Dr. Weihrauch kindly permitted the use of antibodies from her research for this project. John Tessmer and David Schwabe often assisted when I was in the middle of surgeries, especially when deploying stents. I also want to extend my appreciation to Drs. Steven Haworth and

Robert Molthen in the Department of Pulmonary and Critical Care Medicine at Medical College of Wisconsin, as well as Dr. Anne Clough in the Department of Mathematics at Marquette University for experimental, technical and imaging guidance. I also want to extend my appreciation to Dr. Scharath Chedella and Sara Landschoot in the Biomaterials laboratory at Marquette University, who were tremendously helpful when sectioning stented vessels and optimizing the staining process.

Lastly, I want to thank all my colleagues in the CV T.E.C. laboratory: Dr. Laura Ellwein, Dr. David Wendell, Dr. Arjun Menon, Timothy Gundert, Ronak Dholakia, Sung Kwon, Sara Nomeland, D.J. Quam, and Andrew Williams. Especially, I want to thank Dr. Laura Ellwein who optimized the process of extracting the geometry of reconstructed vessels from microfocal x-ray computed tomography imaging data for use with computational fluid dynamics modeling. Without this previous work, I would have spent a great deal of additional time on this portion of the project.

TABLE OF CONTENTS

ACKNOWLEDGMENTS i

LIST OF TABLES viii

LIST OF FIGURES ix

COMMON ABBREVIATIONS & ACRONYMS xv

CHAPTER 1: SPECIFIC AIMS 1

Specific Aim #1: 7

Specific Aim #2: 7

CHAPTER 2: BACKGROUND 9

2.1 Metabolic Syndrome 9

2.2 Carbohydrate Metabolism and Type 1 and 2 Diabetes Mellitus 9

2.3 NH Formation Process and T2DM 12

2.4 Blood material interface (BMI) 15

2.5 Application of Abdominal Aortic Stenting in Rats for Evaluation of Restenosis in T2DM 17

2.6 AGEs and Collagen Cross-linking 17

2.7 Applicable Principles of Vascular Biomechanics 19

2.8 Arterioles 23

2.9 AGEs Change Impedance and Arterial Function 24

2.10 Windkessel Approximation of Impedance Spectra 26

2.11 Computational Fluid Dynamics 29

2.12 Indices of WSS Contributing to NH 30

2.13 Molecular Pathways Impacting NH Formation 32

2.14 Mechanisms of NH after Stenting..... 36

2.15 AGEs Related Collagen Cross-linking Breaker: ALT-711 37

2.16 Impact of Downstream Vascular Changing on Upstream Stenting..... 38

CHAPTER 3: METHODS COMMON TO ALL AIMS 40

3.1 Experimental Protocol 40

3.2 Experimental Preparation..... 41

3.3 Stent Implantation..... 42

3.4 Surgical and Post-operative Care..... 44

3.5 ALT-711 Treatment..... 44

3.6 Osmotic Pump Vehicle 46

3.7 Statistical Analysis..... 47

CHAPTER 4. SPECIFIC AIM 1: QUANTIFY THE ABILITY OF AGE-MEDIATED VASCULAR CHANGES TO INCREASE DVR AND ALTER MECHANICAL INDICES KNOWN TO PROMOTE NH IN TYPE 2 DIABETES, AND DETERMINE WHETHER THESE ADVERSE CHANGES CAN BE ALLEVIATED BY ALT-711.. 48

4.1 Review of Rationale Applicable to Aim 1..... 48

4.2 Methods Unique to the Current Aim 48

4.2.1 Hemodynamic Data Acquisition..... 48

4.2.2 Plastic Casting of the Stented Flow Domain 50

4.2.3 Microfocal X-ray CT and Vascular Reconstruction 51

4.2.4 Determination of Windkessel Parameters..... 56

4.2.5 CFD Simulations..... 57

4.2.6 Quantification of TAWSS..... 58

4.2.7 Statistical Procedures for Data Analysis..... 60

4.3 Results..... 61

4.3.1 Osmotic Pump Control 61

4.3.2 Body Weight, HR, Mean BP and Blood Glucose 62

4.3.3 Reconstructed Vessels from SolidWorks 67

4.3.4 Intrastrut TAWSS 68

4.3.5 Circumferential Smoothing Verification 69

4.4 Summary 72

4.5 Potential Limitations 73

CHAPTER 5. SPECIFIC AIM 2: QUANTIFY AGES RELATED COLLAGEN CROSS-LINKING AND PROTEIN EXPRESSION IN MULTIPLE ARTERIAL LOCATIONS TO ELUCIDATE MOLECULAR CHANGES CONTRIBUTING TO NH AFTER STENTING FOR T2DM, AND DETERMINE WHETHER THESE ADVERSE CHANGES CAN BE ALLEVIATED BY ALT-711. 78

5.1 Review of Rationale Applicable to Aim 2 78

5.2 Methods Unique to the Current Aim 79

5.2.1 Harvest of Arteries 79

5.2.2 Isolation of Cremaster Arterioles 79

5.2.3 Stented Vessel Embedding 81

5.2.4 Hematoxylin and Eosin Staining and Image Acquisition 82

5.2.5 NH Quantification 83

5.2.6 AGEs Related Collagen Cross-linking Analysis 86

5.2.7 Protein Isolation from Arteries 87

5.2.8 Western Blot Analysis 88

5.2.9 Housekeeping Gene 90

5.2.10 Statistical Procedures for Data Analysis 90

5.3 Results 91

5.3.1 Osmotic Pump Control 91

5.3.2 AGEs Related Collagen Cross-linking 92

5.3.3 NH Quantification..... 94

5.3.4 Vascular Mean Injury Score Analysis 102

5.3.5 Protein Expression 104

5.4 Summary..... 111

5.5 Potential Limitations..... 112

CHAPTER 6: DISCUSSION..... 114

6.1 Discussion of Aim 1 and 2..... 114

6.2 Unique Methodological Contributions of the Current Investigation 119

6.3 Glucose, Insulin, NH formation and ALT-711 Treatment 122

6.3.1 Glucose and NH Formation 122

6.3.2 Glucose and ALT-711..... 122

6.3.3 Insulin and NH Formation 123

6.3.4 Insulin and ALT-711..... 123

CHAPTER 7: FUTURE DIRECTIONS AND CONCLUSIONS 125

7.1 Future Directions 125

7.1.1 PAR-1 Inhibitor and Parstatin..... 125

7.1.2 Metformin 126

7.1.3 Molecular Pathways..... 127

7.2 Conclusions..... 127

REFERENCES 130

LIST OF TABLES

Table 1. Drug-eluting stent developments and current status. Stent platform, geometry (including thickness), coating, and therapeutic agent are major factors impacting DES performance in terms of restenosis and thrombus. (Adapted from Khan et al, [1])……3

Table 2. Arteries of interest for the current investigation along with their general classification and representation by elements of the Windkessel approximation.(Adapted from Zamir et al. [2])…..……....29

Table 3. Approximate values used with osmotic minipump model 1004.Loading values in reservoir varied slightly depending on the weight of a given rat. (Adapted from ALZET, Cupertino, CA)……..……...……...…47

Table 4. Regional TAWSS (dyn/cm^2) from ZL, ZO and ZD stented rats (N=3/group). Mean ± SEM; * = significant difference between ZD and ZL stented rats. No significant difference was found after ALT-711 treatment.……...…….51

Table 5. Mean BP (mmHg) and blood glucose (mg/dL) in the absence (-) or presence (+) of ALT-711 (mean ± SEM) (N=6/group). Significance when P<0.05; * means significantly different from ZL stented rats……...65

Table 6. Smoothing operations evaluated for longitudinal smoothing of reconstructed microfocal x-ray CT data. ……...……..70

Table 7. Distribution of blood flow in humans at rest. (Adapted from Nichols et al, [3])……..75

Table 8. Scoring rubric for assessing stent-induced vessel injury score. (Adapted from Schwartz et al. [4])…….86

Table 9. Primary and secondary antibodies used for Western blot. Beta tubulin was used as control……89

Table 10. Summary of AGEs related collagen cross-linking and protein expression changes for vessels in ZO and ZD rats, relative to respective values in ZL rats. (N=6/group), NC means no change, ↑ means significant increase, diagonal means increase was alleviated by ALT-711……..……..……111

LIST OF FIGURES

Figure 1. Correlation of WSS distributions immediately after stent implantation and the location of neointimal hyperplasia quantified 14 days after stenting. The middle computational model predicts low WSS areas are created adjacent to stent struts. Plots on the right show these areas of low WSS have more NH formation while NH is more modest in higher WSS regions.* indicates the location of stent struts. (Adapted from LaDisa et al, [5])……..5

Figure 2. Illustration of the inflammation and restenosis process after bare metal stent implantation. A, Atherosclerotic plaque has formed inside the vessel. B, Platelets will be deposited immediately after stenting and release cytokines that promote attachment of circulating leukocytes. C, Leukocytes will then infiltrate across the platelet-fibrin layer into the vessel wall, while SMC proliferate and migrate from the media into the neointima. D, This process will lead to thickening of the neointimal layer and change to more extra cellular matrix plaque over time. (Adapted from Welt et al, [6]) ……...…14

Figure 3. Diagram of AGEs formation and collagen cross-linking. Glucose reacts with free amino groups on proteins, is changed to a Schiff base and Amadori product, and ultimately forms AGEs. After AGEs are formed, they have an active site to trap a free amino group on another collagen. Once these two sites bind together, they form glucose-derived cross-links, and we call this process AGEs related collagen cross-linking. (Adapted from Aronson et al, [7])……...…….19

Figure 4. The stress strain curve. Stiffness is the slope of stress strain curve which is the same as the modulus of elasticity. An increase in the vascular circumferential stress results in an increase in the stiffness. (Adapted from Westerhof et al. [8])……...……21

Figure 5. Arterial impedance spectra with relevant physiological portions of the curve labeled (A). The solid line in B was for rats with increased AGEs expression, and the dashed line was for rats treated with a compound to inhibit AGEs expression. By reducing AGEs expression, total arterial resistance was reduced, and characteristic impedance was decreased.(Adapted from Westerhof et al, [9] and Lin et al, [10])..……26

Figure 6. The three-element Windkessel model. Rp describes the peripheral resistance, C is the arterial capacitance, and Rc represents the resistance of the local artery of interest……28

Figure 7. Distributions of normalized WSS in control and stented rabbit iliac arteries. The theoretical distribution of normalized WSS after stenting (i.e. acute) is progressively alleviated after 14 and 21 days to restore values back toward a preferential value. (Adapted from LaDisa et al, [5])……32

Figure 8. AGEs related pathways. The interaction of AGEs and RAGE activates nuclear transcription factors and further influences oxidative stress and nitric oxide (NO) formation (Adapted from Welt et al, [6])……..33

Figure 9. Illustration of the balance between oxidative and reductive stress (Adapted from Kohen et al. [11])……..35

Figure 10. Mechanical and molecular pathways tested as part of the current investigation. The mechanical pathway refers to changes predominantly mediated by AGE formation increasing collagen cross-links and modifying vessel structures that lead to increased peripheral resistance as well as decreased arterial capacitance and WSS. The molecular pathway refers to changes predominantly mediated by increased expression of AGE, RAGE and TGFβ leading to structural vascular alterations. "?" indicates a potential interaction while "X" indicates a location of potential inhibition by ALT-711 that was tested as part of the current investigation.…….....39

Figure 11. Schematic illustration of the experimental protocol. Stent implantation was performed at 12 weeks for lean, obese and diabetic rats in the absence and presence of ALT-711 administered using osmotic minipumps. After 21 days, rats were randomly selected for estimation of wall shear stress (WSS) by computational fluid dynamics (CFD) modeling (N=3/group) where applicable as described below, or quantification of neointimal hyperplasia (NH) and protein expression (N=6/group). An additional group of rats (n=4) underwent stenting and administration of saline alone to reveal any potential influence of the minipump and vehicle for ALT-711.……...……41

Figure 12. 316L stainless steel balloon expandable stent specially suited for small dimensions (2.5x8 mm) and with a known geometric pattern (A) for use with 2.5x12 mm rapid-exchange delivery catheters (B and C) obtained from Polymerex (San Diego, CA) were created in conjunction with Burpee Materials Technology (D; Eatontown, NJ) and crimped (E) prior to sterilization and use. ……..……..43

Figure 13. ALZET Osmotic Miniumps. (Adapted from ALZET, Cupertino, CA)……..47

Figure 14. Blood flow (ml/min, solid line) and blood pressure (mmHg, dashed line) were recorded using WINDAQ software. The software was calibrated first, and settings were adjusted to optimize the dynamic range of the signals……..49

Figure 15. Image of the microfocal x-ray CT imaging system and cast of a rabbit abdominal aorta and iliac arteries. (Adapted from LaDisa et al, [12]) ……..…….…..53

Figure 16. Projection image obtained for the abdominal aorta of a representative rat from the current work. Three hundred and sixty of these images were captured for each casted abdominal aorta in one degree increments to generate isotropic reconstruction volumes. The diameter of the catheter (1.1mm) was used as a scale for calibration..…….....54

Figure 17. Images showing a cross-sectional slice from the reconstruction volume for the abdominal aorta of a representative rat from the current work. The left image shows an artificial second grey ring shadowing effect around the real reconstructed vessel caused by improper steps in the reconstruction process. The right image shows a correct reconstruction without this artifact. This was in the middle of the reconstruction process, and no scale was available. These images were only used for verifying the accuracy of reconstruction process.……...……....56

Figure 18. Diagram showing the locations for instrastrut TAWSS quantification after CFD simulations. A through F represent six locations in the middle of the stented region where 9 nearest neighbor values were averaged to quantify TAWSS for ZL, ZO and ZD stented rats. ……..…….60

Figure 19. Body weight, blood glucose concentration and HR from stented ZL rats. White bars indicate stented ZL rats, and black bars indicate stented ZL rats implanted with osmotic minipumps containing saline (N = 4/group). No significance was found for these indices.……..……62

Figure 20. Body weight and heart rate of ZL, ZO and ZD stented rats. White bars represent rats without treatment, and black bar represent rats that received ALT-711 (N=6/group). Body weight and HR were not different for ZL, ZO and ZD rats in the absence or presence of ALT-711…….....63

Figure 21. Weight difference before the stenting procedure and at harvest for untreated and ALT-711 treated ZL, ZO and ZD rats. No significant differences were observed….64

Figure 22. Mean blood flow and resistance in ZL, ZO, and ZD stented rats in the absence or presence of ALT-711 treatment (N=6/group); * = significantly different from ZL, ∇ = significant difference within group.……...……66

Figure 23. Renderings of the stented region from representative ZL, ZO and ZD rats as produced with SolidWorks after post-processing of reconstructed microfocal x-ray CT data.……67

Figure 24. Representative TAWSS results in the ZL, ZO and ZD stented rats. Results from CFD are shown on the left and corresponding unwrapped versions appear to their right.……...68

Figure 25. Corresponding distributions of TAWSS from intrastrut regions within the middle of stents implanted into the abdominal aorta of ZL, ZO and ZD rats (N=6/group); * = significantly different from ZL, # = significantly different from ZO rats.…….....69

Figure 26. TAWSS CFD results obtained using a filter averaging 5 and 8 points longitudinally as part of the postprocessing operation applied following reconstruction of microfocal x-ray CT data. …….71

Figure 27. TAWSS values from intrastrut regions in the middle of the stent (N=6/group). No TAWSS difference were observed when results from 9 nearest neighbor elements within the center of six intrastrut regions were averaged for CFD models created from postprocessing operations using longitudinal smoothing operations consisting of a 5 or 8 point moving average filter.……...……....72

Figure 28. Arterioles from a rat cremaster muscle. A1 is the main cremaster feeding vessel, A2 is the arterioles branch, and A3 is the branch off the A2-arterioles. (Adapted from http://openi.nlm.nih.gov). A scale is not available for this open source image……81

Figure 29. Stented arteries were embedded in glycol methyl methacrylate (left), and a Sorvall MT2 retracting microtome with tungsten carbide blade shown on the right was used for sectioning.……...…….82

Figure 30. Example of NH quantification methods applied using a representative untreated ZL rat. A shows a montage of a stented vascular section (4X) with a calibration scale on the bottom. B shows the image loaded into ImageJ and converted into an 8-bit grayscale image. C shows an image of NH after digital removal of the vessel outside that bounded by stents struts, blood particles within the vessel region, and stent struts were removed using ImageJ, and D shows thresholding of NH to obtain the area for quantification.……...…….85

Figure 31. NH quantification for ZL stented rats without osmotic minipump (white bars) and ZL stented rats with osmotic minipump containing saline alone (black bar) (N=4/group); No significance was found for either index of NH.……...…….91

Figure 32. AGEs related collagen cross-linking (A) and protein expression (fold-change over beta tubulin) for (B) AGEs, (C) RAGE and (D) TGFβ in ZL stented rats without osmotic minipump (white bar) and ZL stented rats with osmotic minipump loaded saline along (black bar). There were no significant differences between groups of ZL stented rats receiving minipumps loaded with saline alone as compared to untreated ZL stented rats.……...……..92

Figure 33. AGEs related collagen cross-linking in carotid artery, TA and AAo (N=6/group). No significant differences were found. ……..…….93

Figure 34. AGEs related collagen cross-linking in iliac and femoral arteries and arterioles (N=6/group); * = significantly different from ZL stented rats, # = significantly different from ZO stented rats, ∇ = significant difference within group. ……..……...94

Figure 35. Representative photomicrographs of 5 micron aortic sections from the center of the stented region stained with H&E from ZL, ZO and ZD stented rats (N=6/group). The total length of the scale is 1mm.…….……..……..95

Figure 36. Representative H&E staining of ZL rats without treatment (4X). Whole vessel image (top), and zoomed in image (bottom). The total length of the scale is 1mm……..96

Figure 37. Representative H&E staining of ZO rats without treatment (4X). Whole vessel image (top), and zoomed in image (bottom). The total length of the scale is 1mm……..97

Figure 38. Representative H&E staining of ZD rats without treatment (4X). Whole vessel image (top), and zoomed in image (bottom). The total length of the scale is 1mm……..98

Figure 39. Representative H&E staining of treated ZL rats with ALT-711treatment (4X). Whole vessel image (top), and zoomed in image (bottom). The total length of the scale is 1mm……...99

Figure 40. Representative H&E staining of treated ZO rats with ALT-711 treatment (4X). Whole vessel image (top), and zoomed in image (bottom). The total length of the scale is 1mm…….100

Figure 41. Representative H&E staining of treated ZD rats with ALT-711 treatment (4X). Whole vessel image (top), and zoomed in image (bottom). The total length of the scale is 1mm…….101

Figure 42. Histograms depict the percentage of the luminal area bounded by the stent (left) and intrastrut thickness (right) containing neointimal hyperplasia for ZL, ZO and ZD rats (N=6/group); * = significantly different from ZL, ∇ = significant difference within group.……...…….102

Figure 43. Mean injury score quantified in the middle of the stented region from ZL, ZO and ZD before and after ALT-711 treatment (mean and SEM). No significant differences were found between groups of rats or within groups after treatment.…….....103

Figure 44. Representative Western Blot image of AGEs protein expression from three ZL rats without ALT-711 treatment. Numbers 1 to 5 correspond to arteries from carotid, thoracic aorta, AAo, IF, and arterioles from cremaster muscle for each rat…..…….……104

Figure 45. AGEs protein expression (fold-change over beta tubulin) in carotid artery, TA and AAo (N=6); * = significantly different from ZL stented rats, # = significantly different from ZO stented rats, ∇ = significant difference within group.…..……...105

Figure 46. AGEs protein expression (fold-change over beta tubulin) in IF and arterioles (N=6); * = significantly different from ZL stented rats, and ∇ = significant difference within group.……..……..106

Figure 47. RAGE protein expression (fold-change over beta tubulin) in carotid artery, TA and AAo (N=6); * = significantly different from ZL stented rats, # = significantly different from ZO stented rats, ∇ = significant difference within group…….....107

Figure 48. RAGEs protein expression (fold-change over beta tubulin) in IF and arterioles (N=6); * = significantly different from ZL stented rats, # = significantly different from ZO stented rats, ∇ = significant difference within group.……....108

Figure 49. TGFβ protein expression (fold-change over beta tubulin) in carotid artery, TA and AAo (N=6); * = significantly different from ZL stented rats, # = significantly different from ZO stented rats, ∇ = significant difference within group.…….…...109

Figure 50. TGFβ protein expression (fold-change over beta tubulin) in IF and arterioles (N=6); * = significantly different from ZL stented rats, and # = significantly different from ZO stented rats. ……..110

Figure 51. Working scale for the current investigation. The size of the AAo (~1.7 mm) is smaller than the tip of a typical ballpoint pen (~2.4 mm), the diameter of the 8-0 suture employed to close the incision used for stenting in this investigation (0.04 mm) is less than half the size of a human hair, and the actual working area accessed under microscopic guidance is the size of a penny.……...……120

Figure 52. The mechanical and molecular pathways tested for T2DM in this investigation. ALT-711 decreased AGEs related collagen cross-linking and arteriolar stiffness in obese and diabetic rats after stent implantation. “X” indicates a location of inhibition by ALT-711 or difference from previously observed relationships. ALT-711 deceased AGEs related collagen cross-lining, increased local blood flow, decreased DVR, and was not associated with differences in regional distributions of WSS between groups. ALT-711 treatment reduced NH in lean, obese and diabetic rats. No significant differences were noted for RAGE and TGFβ expression. However, other related pathways remain to be tested. …….…...129

COMMON ABBREVIATIONS & ACRONYMS

AAo = abdominal aorta

A/D = analog-to-digital

ADP = adenosine diphosphate

AGEs = advanced glycation end-products

Akt = protein kinase B

ALT-711 = Alagebrium (3-phenacyl-4, 5-dimethylthiazolium chloride)

ANOVA = analysis of variance

BF = blood flow

BMI = blood material interface

BMS = bare-metal stents

BP = blood pressure

BSA = bovine serum albumin

C = the arterial capacitance

CFD = computational fluid dynamics

CVD = cardiovascular disease

D = Distensibility

DES = drug-eluting stents

DVR = distal vascular resistance

E = elasticity

ERK = extracellular signal-regulated kinases

esRAGE = endogenous secretory soluble RAGE

GAPDH = glyceraldehyde-3-phosphate dehydrogenase

GMM = glycol methyl methacrylate

H&E = Hematoxylin and Eosin

HMGB-1 = high-mobility group box-1

HPLC = high-performance liquid chromatography

HR = heart rate

IF = iliac and femoral arteries

IP = Intraperitoneal

IV = Intravenous

LDL = low density lipoprotein

MAPK = mitogen-activated protein kinase

MMP = matrix metalloproteinases

NADPH = nicotinamide adenine dinucleotide phosphate

NF-kB = nuclear factor-kappa B

NH = neointimal hyperplasia

NO = nitric oxide

$P2Y_{12}$ = purinergic receptor

PAR1 = protease-activated receptor

PES = paclitaxel drug-eluting stents

PI3K = phosphoinositide 3-kinase

PKC = protein kinase C

RAGE = receptor of AGEs

Rc = characteristic resistance

ROS = reactive oxygen species

Rp = peripheral resistance

Rt = terminal resistance

SES = sirolimus drug-eluting stents

SMC = smooth muscle cell

sRAGE = soluble RAGE

T1DM = type 1 diabetes mellitus

T2DM = type 2 diabetes mellitus

TA = thoracic aorta

TAWSS = time-averaged WSS

TBS-T = Tris-Buffered Saline and Tween 20

$TBXA_2$ = thromboxane A_2

TGFβ = the transforming growth factor beta

VCAM-1 = vascular cell adhesion protein 1

WSS = wall shear stress

ZD = Zucker diabetic rat

ZDF = Zucker Diabetic Fatty

ZL = Zucker lean rat

ZO = Zucker obese rat

CHAPTER 1: SPECIFIC AIMS

It is estimated that 25.8 million Americans are diabetic (8.3% of the population) and an additional estimated 79 million have the metabolic syndrome, a constellation of clinical findings that substantially increases the risk for developing type 2 diabetes mellitus (T2DM) [13]. Cardiovascular disease (CVD) accounts for 68% of diabetes-related deaths among people aged 65 years or older as these patients have a 2 to 4-fold increased risk of developing coronary and peripheral artery disease [13, 14].

Bare-metal stents (BMS) are permanent metal scaffolds that can be implanted during a minimally-invasive procedure to restore blood flow (BF) beyond a vascular occlusion presenting in CVD. Unfortunately, restenosis occurring primarily as a result of excessive neointimal hyperplasia (NH) limits the success of BMS [6]. These cases require repeat revascularization of the lesion and have cost the U.S. healthcare system over 2.5 billion dollars since 1999 [15].

Drug-eluting stents (DES; **Table 1**) have also been used to combat CVD, but are less effective at reducing restenosis rates in patients with T2DM [16, 17]. Studies have demonstrated that sirolimus and paclitaxel (antiproliferative agents) used with early generation DES did not facilitate healing of the intima after implantation thereby inhibiting coverage of the stent linkages by endothelial cells and making the vessel more prone to late thrombosis [18, 19]. Newer generation DES such as zotarolimus and everolimus inhibit the proliferation of smooth muscle and inflammatory cells [1]. Unfortunately studies comparing the efficiency of everolimus to paclitaxel [20, 21] indicate that improvements in mortality, myocardial infarction, stent thrombosis and target lesion revascularization afforded to normoglycemic patients with these newer DES

have not translated to diabetic patients [20, 21].

	First generation		Second generation			Third generation		Bioabsorbable stents	
Stent name	Cypher®	TAXUS® Express®	TAXUS® Liberté®	Endeavor®	Xience V® and Prime®	ION™ / TAXUS® Element™	PROMUS Element™	ABSORB	DREAMS
Manufacturer	Johnson& Johnson	Boston Scientific	Boston Scientific	Medtronic	Abbott Vascular	Boston Scientific		Abbott Vascular	Biotronik
Stent platform	Stainless steel		Cobalt chromium			Platinum chromium		poly-L-lactide	Magnesium alloy
Strut Thickness (microns)	140	132	96	91	81	81	81	156	120
Coating	durable polymer		Durable polymer persistent			biodegrable polymer		Polymer free	
Therapeutic agent	Sirolimus	Paclitaxel	Paclitaxel	Zotarolimus	Everolimus	Paclitaxel	Everolimus	Everolimus	Paclitaxel
Problems	Late stent thrombosis		Lower late stent thrombosis than first generation			To be determined		To be determined	

Table 1. Drug-eluting stent developments and current status. Stent platform, geometry (including thickness), coating, and therapeutic agent are major factors impacting DES performance in terms of restenosis and thrombus. (Adapted from Khan et al, [1])

Mechanisms for elevated restenosis rates after stenting in T2DM compared to normoglycemic patients have not yet been fully elucidated. It has been suggested that the current paradigm for the use of stents in patients with T2DM applies methods from retrospective revascularization studies conducted in normoglycemic patients to T2DM in hopes that poor outcomes do not occur [22]. In contrast, some investigators have examined pharmacological agents such as antisense oligonucleotides and L-arginine supplementation to improve endothelial function, but these pharmacologic agents failed to alleviate restenosis in T2DM [23, 24]. While local changes in cytokine release and cell signaling undoubtedly play a role in this process, investigation of the inciting changes in local fluid dynamics and vascular biomechanics associated with T2DM, which may also contribute to restenosis, have been relatively ignored. For example, adverse structural modifications are known to occur throughout the arterial system in response to T2DM including increased vascular stiffness due to advanced glycation end-products (AGEs) which are formed through nonenzymatic reaction between glucose and proteins as discussed in more detail below.

It has been reported that AGEs can cause tissue damage in the cardiovascular system by cross-linking with collagen, thus disrupting the vessel wall and altering its compliance (i.e. increasing its stiffness) [25]. These changes may be manifested by an increase in distal vascular resistance (DVR) in arterioles with subsequent alterations in local flow patterns, blood pressure (BP), and wall shear stress (WSS) within the upstream stent, which has previously been correlated with NH (**Figure 1**) [5].

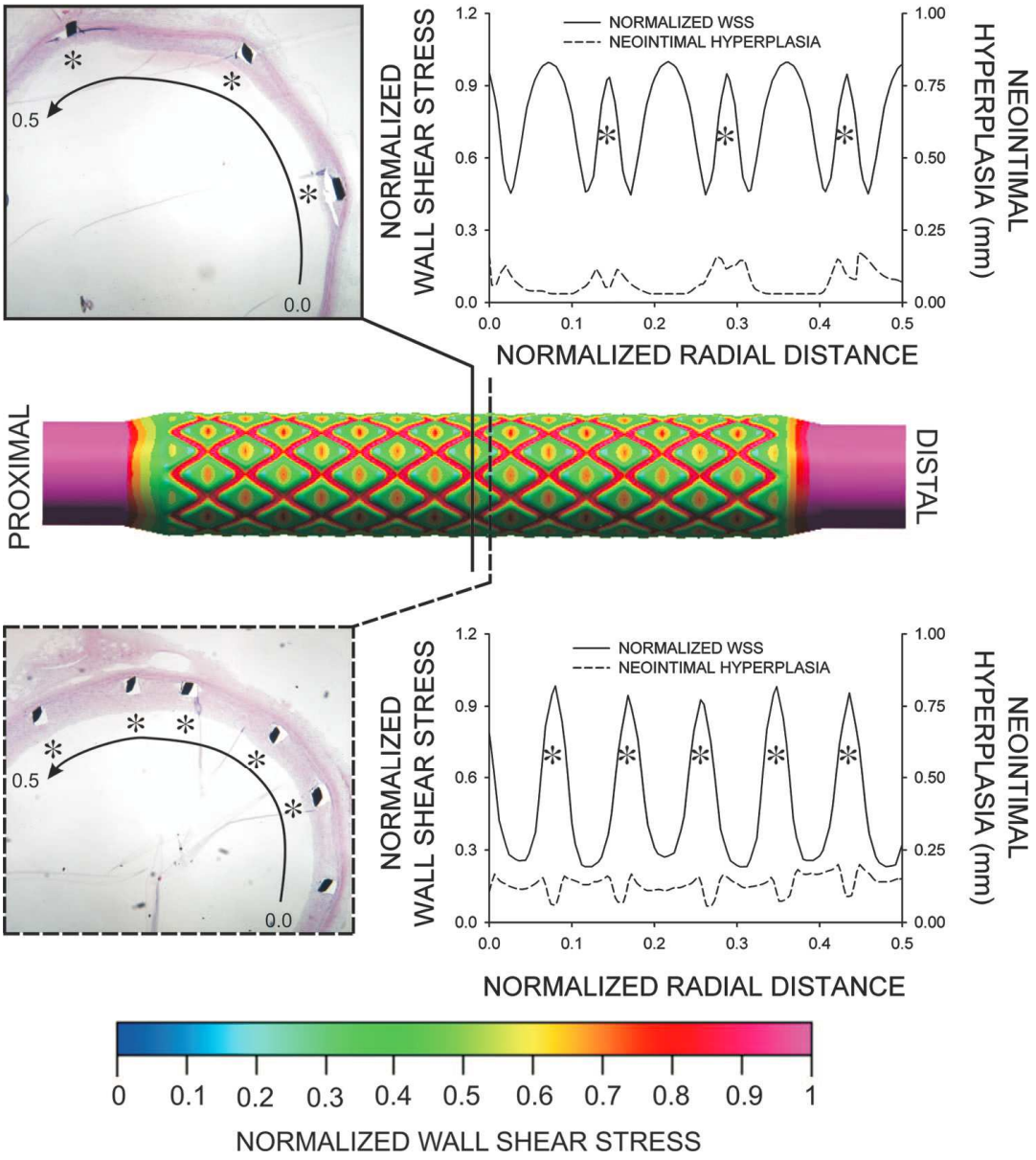

Figure 1. Correlation of WSS distributions immediately after stent implantation and the location of neointimal hyperplasia quantified 14 days after stenting. The middle computational model predicts low WSS areas are created adjacent to stent struts. Plots on the right show these areas of low WSS have more NH formation while NH is more modest in higher WSS regions. indicates the location of stent struts. (Adapted from LaDisa et al, [5])*

It has been shown that AGEs formation is more rapid during diabetes [26, 27], and may also react with a receptor (RAGE) to increase expression of transforming

growth factor beta (TGFβ), oxidative stress, protein kinase C (PKC) activity, and extracellular matrix accumulation [28]. Alagebrium (ALT-711; 3-phenacyl-4, 5-dimethylthiazolium chloride) has been shown to cleave AGEs related collagen cross-linking thereby decreasing vessel resistance and atherosclerosis [29, 30]. ALT-711 has also been shown to decrease TGFβ protein expression [31], and it may therefore decrease NH in the stented region, as well as downstream regions in the setting of T2DM. **Therefore, this project tested the hypothesis that elevated NH observed after BMS implantation in T2DM is mediated by changes in stent BF dynamics that arise secondary to vascular remodeling, increased formation of AGEs, and increased DVR; and that a pharmacological strategy to decrease AGEs reduces NH in T2DM**. This hypothesis was tested in two specific aims during which the mechanical and molecular aspects introduced by T2DM were queried. Specifically, computational fluid dynamics (CFD) modeling was used to quantify the influence of WSS distributions in stented arteries of T2DM rats. Analysis of NH in the stented region was performed using Hematoxylin and Eosin (H&E) for correlation to CFD results. AGEs related collagen cross-linking, and quantification of protein expression was conducted using Western blotting in the carotid arteries, thoracic aorta (TA), abdominal aorta (AAo), iliac and femoral arteries (IF) as well as arterioles in cremaster muscle of stented T2DM rats. This multidisciplinary approach leverages an animal model of T2DM to further elucidate the mechanisms of restenosis that may be applicable to this patient population. The results may ultimately be translated to the clinic for the reduction of restenosis in patients with T2DM.

Specific Aim #1: Quantify the ability of AGE-mediated vascular changes to increase DVR thereby altering mechanical indices known to promote NH in type 2 diabetes, and determine whether these adverse changes can be alleviated by ALT-711.

Approach: Animals from three lines of Zucker diabetic fatty (ZDF) rats (lean (ZL), obese (ZO) and diabetic (ZD) groups) were randomly selected to undergo abdominal aortic stenting. Additional rats from each group underwent the same procedure but also had an osmotic minipump loaded with ALT-711 (1mg/kg/day) or vehicle inserted into the abdomen. Twenty one days after stenting, BP was measured in the carotid artery and BF was measured in the stented region for use in CFD simulations. A computational representative of the geometry within the stented region was then constructed, and measured BF was prescribed at the inlet of the CFD model using a time-varying Womersley profile. A three-element Windkessel model served as outlet boundary conditions [32]. Hence, CFD simulations were performed to match measured BF and BP data, and demonstrate the influence of distal vascular changes occurring in T2DM on time-averaged WSS (TAWSS), and compared to the same indices determined for ALT-711 treated rats.

Specific Aim #2: Quantify AGEs related collagen cross-linking and protein expression in multiple arterial locations to elucidate molecular changes contributing to NH after stenting for T2DM, and determine whether these adverse changes can be alleviated by ALT-711.

Approach: Randomly selected rats from ZL, ZO and ZD groups underwent abdominal aortic stenting. Additional rats from each group were treated with ALT-711 (1mg/kg/day) or vehicle using the osmatic minipump mentioned above implanted into the abdomen. Twenty one days later the stented region was carefully harvested, fixed in 4% paraformaldehyde, and dehydrated using a series concentration of increasing ethanol.

The stented region was embedded in glycol methyl methacrylate and sectioned at 5µm thickness for staining by H&E to quantify NH. Vessels from the central elastic arteries such as the TA, AAo and carotid arteries, peripheral muscular arteries including the IF, and smallest distal arteries (i.e. arterioles) were also harvested. These vessels were used to quantify collagen concentration using a spectrophotometer, and measured for AGEs using a fluorescence photometer. Protein was also isolated and purified from these vessels in preparation for the use of Western blotting techniques to quantify expression.

CHAPTER 2: BACKGROUND

2.1 Metabolic Syndrome

Metabolic syndrome is defined as impaired insulin sensitivity, glucose intolerance or diabetes mellitus associated with abdominal obesity, dyslipidemia and urinary microalbuminuria [33]. Elevated low-density lipoprotein (LDL) cholesterol, low high-density lipoprotein cholesterol, abdominal fat, high triglycerides, and high blood pressure are common with metabolic syndrome [34], but a key factor is insulin resistance. Insulin resistance occurs when enough insulin is produced, but organisms are desensitized to its binding to receptors for function. In addition, T2DM has a negative effect on insulin resistance that is further increased by LDL, triglyceride, and blood glucose levels [34]. Recent research found the metabolic syndrome can predict CVD and coronary heart disease [35]. In addition, Lorenzo et al. reported that the metabolic syndrome can be a predictor for T2DM [36]. By fully understanding regulation of metabolic syndrome, the risk of developing into T2DM and the potential for poor outcomes after stenting for CVD may be minimized.

2.2 Carbohydrate Metabolism and Type 1 and 2 Diabetes Mellitus

Carbohydrate metabolism is important to provide an energy source and materials for maintaining physiological functions, and biosynthetic reactions such as constructive processes that form amino acids from proteins. The most common carbohydrate in humans and animals that provides energy is glucose. When glucose is not immediately required for energy, extra glucose may be stored as glycogen. Once cells approach saturation with glycogen, the additional glucose is then converted to fat in the liver and

stored in fat cells. The liver is therefore the major glucose metabolism regulation organ, and contains large amounts of glycogen for rapid release into circulation [37]. In normal glucose metabolism, blood glucose concentration is determined and regulated by hormones such as insulin and glucagon, which are released from the islets of Langerhans within the pancreas. There are two types of cells in the islets of Langerhans: α-cells (40%) and β-cells (60%). Alpha-cells are responsible for synthesizing and secreting the glucagon, which elevates blood glucose concentration. Beta-cells are responsible for storing and releasing insulin, which works to reduce blood glucose concentration. There is another 16kDa hormone called leptin which is primarily secreted by adipocytes [38]. Leptin was identified in 1994 and it has since been discovered that it directly influences the energy homeostasis process. A lack of leptin was found to be directly related to diabetes [39, 40]. When the hormones above work properly, extra glucose in the blood stream will be stored in the liver, or fat and protein will be broken down to maintain glucose levels. However, glucose metabolism is not regulated well under diabetic conditions, resulting in hyperglycemia. Diabetes mellitus is therefore a metabolic disorder of carbohydrate, fat and protein metabolism due to improper insulin secretion or action [37]. The two types of diabetes mellitus are discussed below.

Type 1 diabetes mellitus (T1DM) is characterized by the presence of anti-glutamic acid decarboxylase, islet cell or insulin antibodies. In general, T1DM includes immune-mediated diabetes and idiopathic diabetes. Immune-mediated T1DM is the result of T-cell mediated autoimmunity and causes destruction of β-cells located in the islets of Langerhans within the pancreas [33]. The rate of β-cell destruction varies from rapid in children to slow in adults. It is therefore necessary to provide insulin in order to prevent

the development of ketoacidosis, coma and death. Idiopathic T1DM is a specific type that lacks β-cell autoimmunity, and has a strong genetic component, especially in people of African and Asian ancestry.

T2DM is characterized by disorders of insulin action and secretion [33]. This includes insulin resistance and relative insulin deficiency, but β-cell autoimmune destruction does not usually present. Most patients with T2DM display obesity, especially in the abdominal region. T2DM is usually undiagnosed for many years because hyperglycemia increases gradually so that the associated symptoms are not immediately noticeable [41]. T2DM does not require treatment of insulin for earlier stage patients; however, it has been associated with CVD, and pronounced NH that contributes to restenosis after stent implantation [6].

Insulin level in T1DM is significant decreased because the body cannot produce insulin as result of β-cells destruction. The insulin level is usually lower as compared to that in an average normal person before a meal, and the insulin secretion is not increased within 1 hour after a meal as well. In the severe T1DM patients, insulin level even cannot be detected as the result of large amount of β-cells destruction. This T1DM is characterized by an absolute insulin deficiency [42]. Insulin level in T2DM is depended on the length of the disease and obesity status. The insulin level is usually higher than that in an average normal person, and the highest secretion is happened in 2 hour or even delayed rather than normally happened within 1 hour after a meal. The clinical measurement usually found that insulin is increased in T2DM. However, this high insulin level is still not able to decrease glucose. The T2DM is often linked to impaired insulin

sensitivity (insulin resistance), and is characterized by a relative insulin deficiency [42, 43].

Insulin usually regulates and deliveries glucose into cells to provide energy. Insulin resistance is that cells surface receptors are changed so that the normal level of insulin cannot regulate those on adipocyte, muscle cell, and hepatocyte. In adipocytes, insulin resistance results in reduced uptake of circulating lipids and increased the hydrolysis of triglycerides, and elevates the amount of free fatty acids in plasma [44]. In muscle cells, insulin resistance reduces glucose absorption; while in hepatocyte, insulin resistance decreases glycogen synthesis and storage [45, 46]. Insulin resistance causes increasing insulin and glucose which will further contribute to the development of metabolic syndrome and T2DM. The degree of insulin resistance is high in T2DM because cells cannot be fully regulated by insulin which usually is even higher than normal amount. However, the degree of insulin resistance is low in T1DM because the function of adipocyte, muscle cell, and hepatocyte cells is still normal.

2.3 NH Formation Process and T2DM

The process of stenting causes damage to the endothelial cell layer, and stimulates smooth muscle cell (SMC) proliferation and migration to form NH. Welt et al. previously described the process of NH occurring after BMS [6] to cause a mature atherosclerotic plaque as shown in **Figure 2**. After stenting, vascular endothelial cell denudation will cause platelet and fibrinogen deposition (**Figure 2 B**). Shortly after platelet activation, adhesion molecules will begin to cause the attachment of circulating leukocytes via platelet receptors. Under the influence of cytokines released from SMC and resident leukocytes, circulating leukocytes will migrate across the platelet-fibrin

layer and into the vessel wall (**Figure 2 C**). Platelets, leukocytes and SMC will then release growth factors causing migration of SMC from the media into the neointima (**Figure 2 C and D**) ultimately consisting of SMC, extracellular matrix, and macrophages.

Although stents can be implanted during a minimally-invasive procedure to restore BF, restenosis continues to limit their success, particularly in T2DM. DES were designed to decrease rates of restenosis. However, late thrombosis was a major problem for first generation DES. Recently Stone et al. compared normoglycemic patients to those with T2DM receiving newer-generation DES [21]. Although the newer generation DES have been found to improve mortality, myocardial infarction and stent thrombosis, these rates are still not improved for T2DM patients [20, 21]. Previous researchers have found that the wound healing process is delayed in diabetes mellitus [47], which also plays a role in the vascular response to stenting in these patients . The collective mechanisms of this pathological process during restenosis after stenting for diabetic patients is still not clear, but it is reasonable to surmise that mechanical factors such as increased DVR and low WSS as well as molecular factors such as AGEs, RAGE and the TGFβ interactions may play a role.

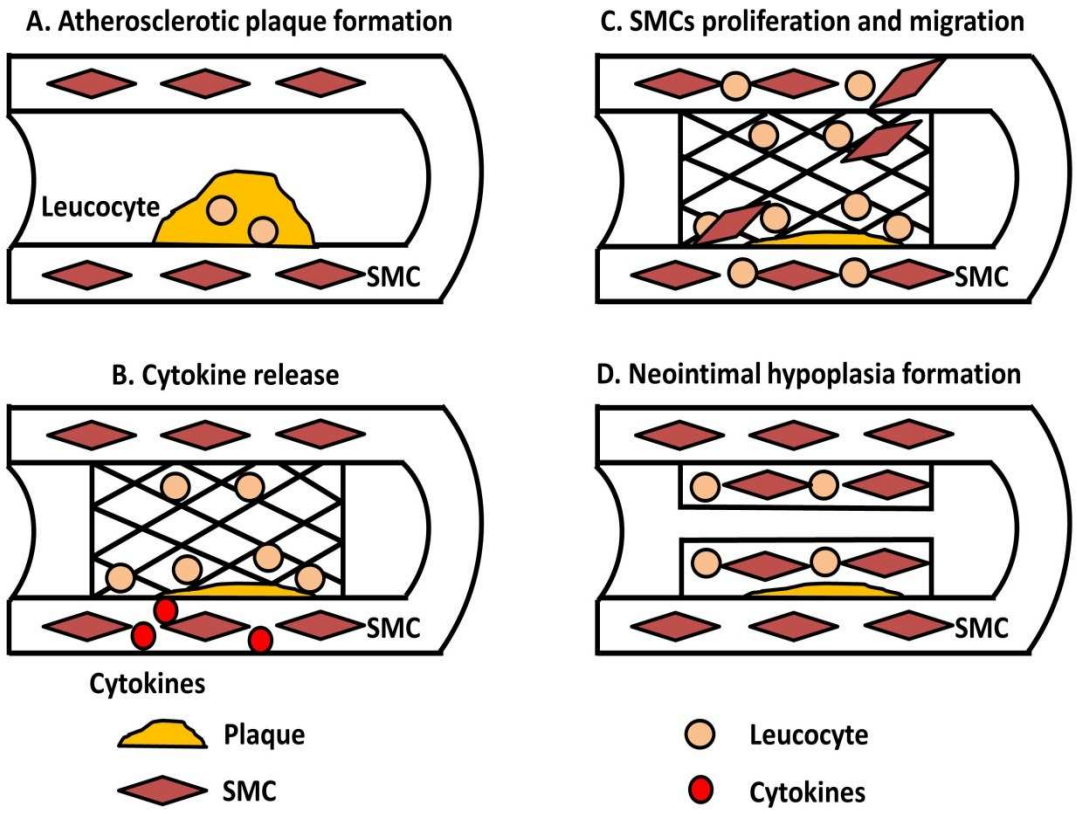

Figure 2. Illustration of the inflammation and restenosis process after bare metal stent implantation. A, Atherosclerotic plaque has formed inside the vessel. B, Platelets will be deposited immediately after stenting and release cytokines that promote attachment of circulating leukocytes. C, Leukocytes will then infiltrate across the platelet-fibrin layer into the vessel wall, while SMC proliferate and migrate from the media into the neointima. D, This process will lead to thickening of the neointimal layer and change to more extra cellular matrix plaque over time. (Adapted from Welt et al, [6])

2.4 Blood material interface (BMI)

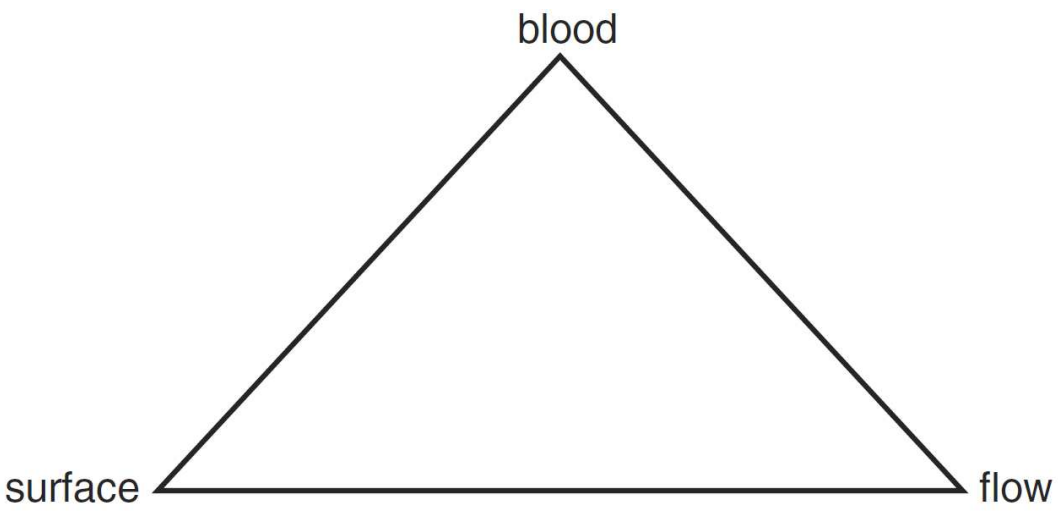

Virchow's triad adapted from Ratner et al. [48]

There are three key factors generally influencing BMI: properties of blood, local flow conditions, and the contacting surface. These are collectively known as Virchow's triad, which was introduced in 1856 by Rudolph Virchow [48]. Virchow's triad is still considered as the standard guideline for BMI evaluation.

Blood properties are different in humans as compared to animals. In addition, blood coagulation properties are different *in vivo* as compared to *in vitro*. It is often unrealistic to test real human blood for BMI in large amounts. In general, most researchers only use blood from a single animal to detect hemocompatibility, which may lead to differences when the material is used in larger populations. *In vitro* tests generally require anticoagulants, which are also used in *in vivo* tests involving extracorporeal circuits. These anticoagulants may change the behavior of BMI. Despite these limitations present in animal blood testing for BMI, this approach still has value as it provides scale and reference results for later testing in humans.

The function of blood flow is to transport nutrients along with associated cells to the BMI, which could initiate an inflammatory reaction within the arterial wall. Low WSS will influence the platelet adhesion, platelet aggregation and thrombus formation on the artificial interface. In general, thrombus formation requires the transport of platelets and coagulation proteins as well as activation of platelets that may be influenced by blood flow patterns.

The surface of materials also needs to be considered for BMI, including material surface properties and blood cell surfaces. Artificial interfaces form a layer of adsorbed proteins after contact with blood, and this layer mediates the attachment of platelets, proteins and other blood cells. However, the relationship between material properties and propensity of a material to cause thrombosis is still not fully understood because of the complexity of cell or protein-surface reaction that may present [48]. Researchers have used heparin binding materials to decrease the thrombogenicity, and weak negatively-charged materials have also been used to prevent negativelycharged blood cells from coagulating [49, 50].

The response of an artery to DES can also be appreciated relative to Virchow's triad. As antiproliferative drugs are slowly released from the DES, they interrupt the migration and proliferation of SMC to reduce NH [51] as compared to BMS [52]. Human coronary artery postmortem analysis has shown a delayed endothelialization on the surface of some DES which may be the reason for late thrombosis [53, 54]. Previously, both polymer-based sirolimus (SES) and paclitaxel (PES) eluting stents demonstrated a significant amount of late thrombosis [55]. The SES has been shown to decrease the rate of thrombosis as compared to PES because sirolimus promotes the contractile SMC

phenotype while paclitaxel promotes the synthetic SMC phenotype that is involved in SMC migration and proliferation [55, 56]. Factors such as incomplete lesion coverage and plaque protrusion may be important for late thrombosis as well [57]. Previous researchers have found that the wound healing process is delayed in diabetes mellitus [47], which also plays a role in the vascular response to stenting in these patients.

2.5 Application of Abdominal Aortic Stenting in Rats for Evaluation of Restenosis in T2DM

As mentioned above, restenosis has been a persistent complication since the onset of stenting [58]. Rabbit iliac and porcine coronary arteries are widely used preclinical models to evaluate restenosis [5, 59-61]. However, a rabbit model for T2DM is not readily available and therefore would require substantial time and effort to create. The size and costs of the porcine model also present serious limitations. A rat carotid artery stented model has been reported previously [62-65]. However, due to the size of the rat carotid artery, a special miniature stent with delivery system would be required. To address this limitation, a rat abdominal aorta stent model with a native diameter similar to the most common coronary artery undergoing stenting in humans has been studied [66] and perfected for use with the current work.

2.6 AGEs and Collagen Cross-linking

Diabetic patients have increased arterial stiffness at a younger age compared to normal individuals [67-69]. Although hyperglycemia has been considered to have an important role in the pathogenesis of diabetes, the mechanisms related to NH still remain unclear. AGEs formation is one of the theories as to how chronic hyperglycemia contributes to morbidity in diabetes. AGEs are formed by the nonenzymatic reaction

between glucose and carbohydrates with amino acids [27, 70]. Glucose reacts with NH_2 chains on amino groups of proteins to produce Schiff bases. For example, glucose often works with the N-terminal valine amino group to form hemoglobin A_{1C}. The unstable Schiff bases will then rearrange to form stable Amadori products over a few days. Although this is a slow reaction, it is much faster than the reverse reaction, and Amadori products subsequently accumulate on proteins. The process of forming Amadori products is called glycosylation [71], and eventually Amadori products can convert into stable, and virtually irreversible, AGEs.

AGEs can react with free amino groups on collagen proteins to form firm cross-links which are known to decrease large vessel compliance (**Figure 3**) [7]. Although this is a normal process within the body with aging, it is accelerated in diabetes [72]. It has been reported that AGEs can cause tissue damage in the cardiovascular system by working with collagen to form cross-links that disrupt the vessel wall structure and increase stiffness [25].

AGEs have an active site which can trap amino groups to form permanent glucose-derived cross-links. This process is referred to as AGEs induced collagen cross-linking in this investigation. Together these findings suggest that AGEs may accelerate collagen cross-linking, increase vessel stiffness, and change DVR in the setting of T2DM.

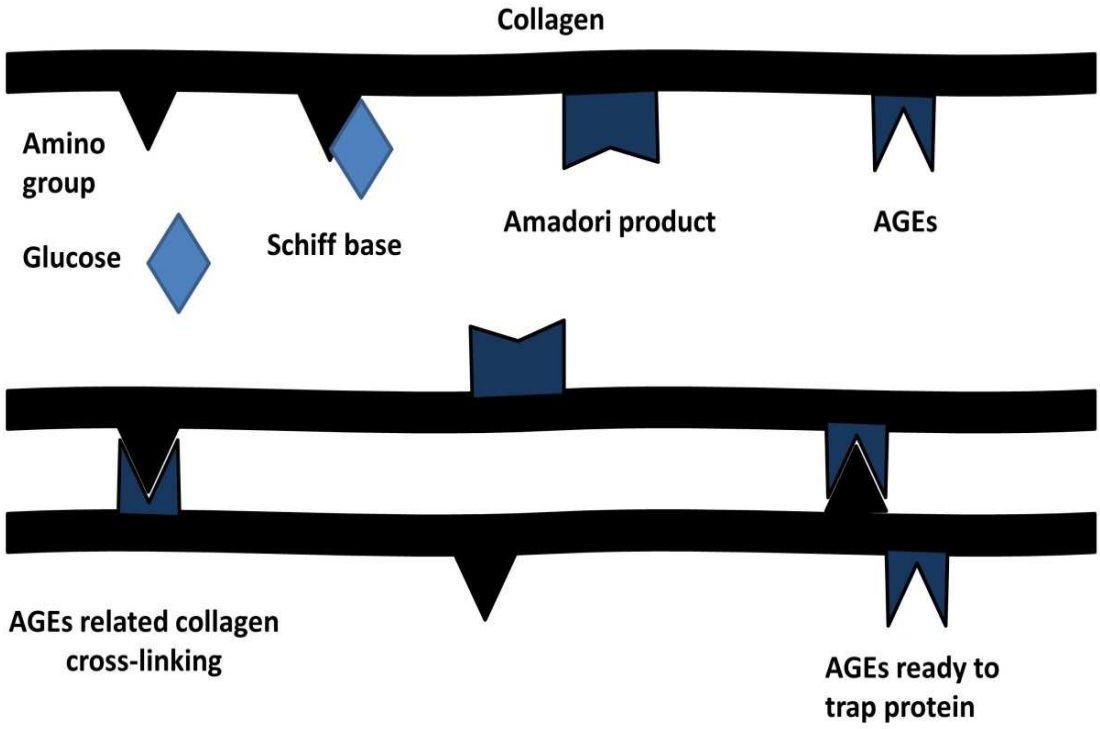

Figure 3. Diagram of AGEs formation and collagen cross-linking. Glucose reacts with free amino groups on proteins, is changed to a Schiff base and Amadori product, and ultimately forms AGEs. After AGEs are formed, they have an active site to trap a free amino group on another collagen. Once these two sites bind together, they form glucose-derived cross-links, and we call this process AGEs related collagen cross-linking. (Adapted from Aronson et al, [7])

2.7 Applicable Principles of Vascular Biomechanics

Vessels in the cardiovascular system have varying diameters and material properties to serve a number of functions. The aorta has the largest diameter of arterial vessels which is necessary for bulk transport over long distances, while the muscular vessels maintain blood pressure and contribute to blood flow and pressure waveform transmission. Arterioles are associated with high resistance to flow, and capillaries have the smallest diameter but with only a single cell layer that allows rapid exchange of water,

oxygen, carbon dioxide and nutrients. The histological structure of the arterial wall was described previously [73]. The predominant materials of the arterial wall are elastin and collagen. The material properties change as the percentage of elastin decreases from central arteries to arterioles. Another major factor contribute the properties of arterial wall is SMC, which contributes to arterial wall tension [73].

The material properties described above are reflected in several indices including compliance (C) [8], which is defined as the change in arterial blood volume (ΔV) due to a given change in arterial blood pressure (ΔP) ($C = \Delta V / \Delta P$) [74]; although this is often reflected in clinical studies as change in area for a given change in pressure. When using this later notation, the capacitance may be a more appropriate expression and can be thought of as the collection of compliances along the length of the vessels of interest.

In contrast to the use of elastic arteries which describe those vessels with high elastin content, elasticity (E) [8] is an engineering term describing the ability of tissue that has been strained or deformed to return to its original shape. In the cardiovascular system, it is the inverse of the compliance. $E = \Delta P/\Delta V$. Stiffness [8] is reflected in the slope of the stress strain curve which is the same as the modulus of elasticity as shown in **Figure 4**.

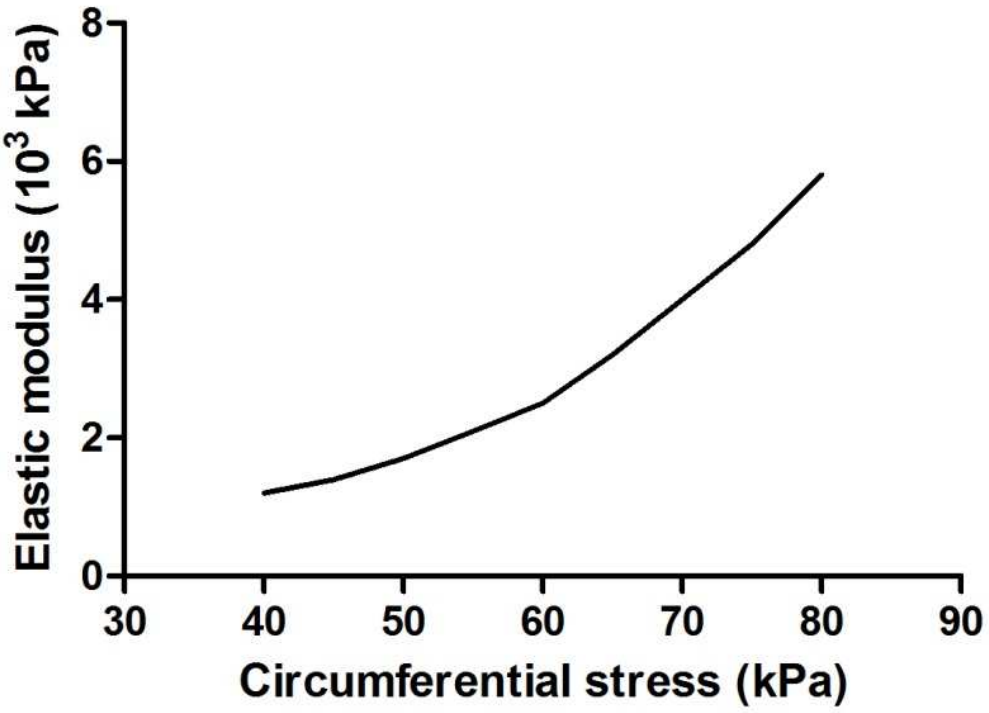

Figure 4. The stress strain curve. Stiffness is the slope of stress strain curve which is the same as the modulus of elasticity. An increase in the vascular circumferential stress results in an increase in the stiffness. (Adapted from Westerhof et al. [8])

Distensibility (D) [8] is a related term that takes vessel stiffness into consideration and is therefore defined as the compliance relative to the initial volume.

$$D = \frac{\Delta \mathrm{V}}{\Delta \mathrm{P}} \times V$$

The relationship between vessels in the arterial tree can be described using asymmetry index, power law index, and area ratio [2]. Asymmetry index is used to describe the relative calibers of daughter segments. Area ratio is used to describe differences in cross-sectional area in daughter segments as compared to the parent

segment. Power law index is a measure of efficiency with respect to vessel branching [2]. General expressions for each of these indices are shown below

Asymmetry index, α, is expressed as:

$$\alpha=\frac{d_2}{d_1},\ \ d_2 \le d_1;\ \ 0<\alpha\le 1$$

Area ratio, β, is expressed as:

$$\beta = \frac{d_1^2 + d_2^2}{d_0^2}$$

Power law index, k, can be determined from:

$$d_0^k = d_1^k + d_2^k$$

Where d_0 is the parent artery, d_1 and d_2 are daughter arteries.

From the above asymmetry index, power law index, and area ratio equations, we can appreciate that for a simple bifurcation from one parent vessel to two daughter vessels, $k<2$ ($\beta<1$) represents area contraction, $k = 2$ ($\beta = 1$) represents area preservation, and $k > 2$ ($\beta >1$) represents an area increasing network. A k value of 3 (i.e. cube law) is associated with a special condition called the principle of minimum work. This concept describes the balance between small vessels and, hence more collective area, requiring more work to drive blood through them, and large vessels requiring large blood volume and higher metabolic energy to maintain. When the k value is 2 (i.e. square law) the branching vessels follow the principle of area preservation as manifested in minimal pressure wave reflection at a bifurcation and maximal wave transmission.

Resistance is a measure of the opposition to blood flow presented by the cardiovascular system or a portion of it. It cannot be directly measured, but can be estimated as mean BP divided by mean blood flow. According to Poiseuille's law, vascular resistance in a cylindrical tube can be calculated as [75]:

$$R = \frac{8\mu l}{\pi r^4}$$

where μ is the blood viscosity, l is the arterial length, and r is the arterial internal radius.

This expression indicates that vascular resistance is largely dependent on the radius of a vessel, and to a lesser extent, the viscosity of blood. Blood is a non-Newtonian shear thinning fluid, indicating that viscosity decreases as the shear rates increases. It has been found that at shear rates above approximately 100 s^{-1}, the viscosity of blood approaches a constant value [75] for a given hematocrit [76]. In contrast, erythrocyte aggregation influences blood viscosity at low shear rates.

2.8 Arterioles

Arteries and arterioles contain three layers: intima, media and adventitia [77]. The intimal layer contains endothelial cells which are involved in intracellular signaling pathways to release vasoactive factors. In addition, studies have found that these endothelial specific cytoskeletal structures play an important role to transduce mechanical forces to neighboring SMC [78]. The medial layer predominantly contains vascular SMC. The major function of these SMC is to control vascular caliber via relaxation and contraction. SMC are surrounded by collagen, fibronectin and collagenous fibrils [79], and these structures may also be involved in transduction of mechanical forces into cellular responses. The adventitia layer contains a mix of fibroblasts and collagen fibers

in extracellular matrix. It has been found that the adventitia layer not only provides structural support to the vessel, but also releases reactive oxygen species (ROS) and TGFβ, and is involved in the vascular repair process [80, 81].

2.9 AGEs Change Impedance and Arterial Function

AGEs have been found to accumulate excessively *in vivo* which may be associated with diabetic complications [82, 83]. The formation of AGEs on matrix components and collagen may cause complications including vascular narrowing and arterial stiffness [82, 84-86]. These changes can influence mechanical indices such as capacitance, as well as systemic and local vascular resistances reflected in an impedance spectra (**Figure 5 A**) [87]. The impedance spectra describes the relationship between the pressure and flow of a linear system, for sinusoidal or oscillatory signals [75]. When impedance is known, a given flow can be used to calculate pressure and vice versa. Impedance is the relationship between pulsatile pressure and pulsatile flow (in the frequency domain) with in an artery system. The basic assumptions are a steady state, time-invariant, and linear system. Impedance can be calculated based on measured pressure and flow at the same vascular location; however, it is almost impossible to measure flow and pressure everywhere in the whole cardiovascular system, so impedances calculated in the human and mammals reflective of downstream vessels provides a method of understanding of arterial function [75]. There are several types of impedance such as longitudinal impedance which describes Womersley's oscillatory flow theory, transverse impedance which describes the oscillatory pressure between a lumen and external environment, and input impedance. Systemic arterial input impedance is a comprehensive description of the entire arterial tree.

Figure 5 A below [9] shows portions of the impedance spectra known to account for total vascular resistance, capacitance, and characteristic impedance. Lin et al. [10] compared impedance spectra of male Wistar rats using Fructose, an agent to induce forming of AGEs, or Aminoguanidine, an inhibitor of AGEs. After two weeks, rats with Fructose and Aminoguanidine (inhibited AGEs expression rats) showed decreased ascending aortic pressure and blood flow, and their impedance spectra showed changes reflective of decreased total resistance and characteristic impedance (**Figure 5 B**). These findings suggest that when AGEs induced collagen cross-linking increases in response to T2DM in the current investigation, it will likely increase total vascular resistance, decrease capacitance, and increase characteristic impedance. These changes would manifest as a shift to the right and upward for the waveform representing the modulus of the input impedance.

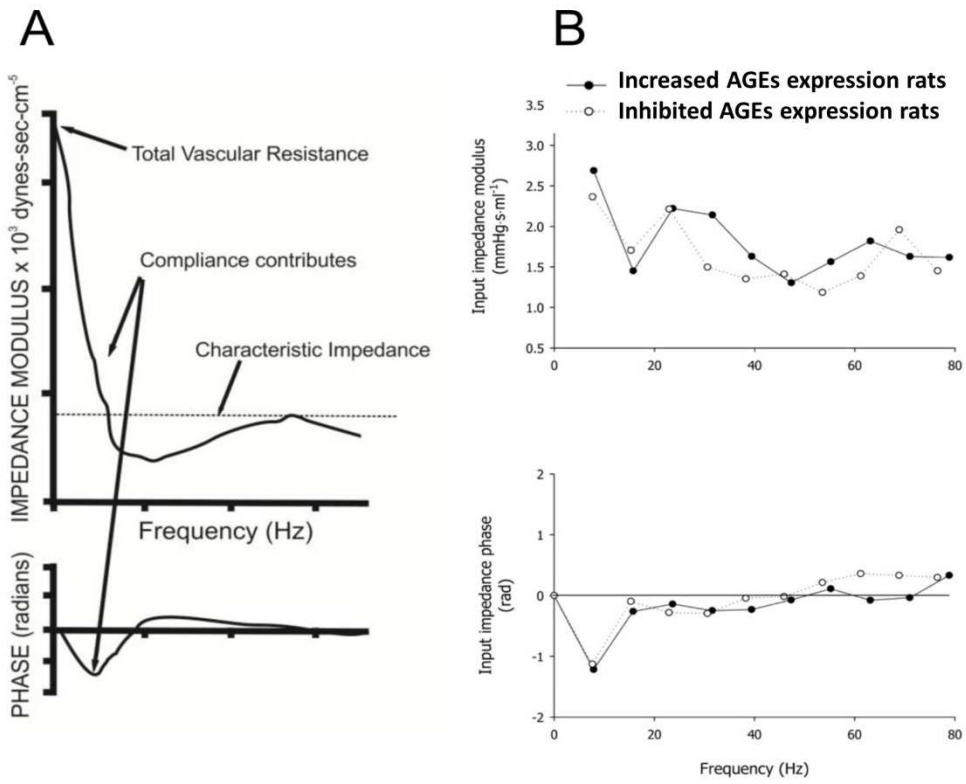

Figure 5. Arterial impedance spectra with relevant physiological portions of the curve labeled (A). The solid line in B was for rats with increased AGEs expression, and the dashed line was for rats treated with a compound to inhibit AGEs expression. By reducing AGEs expression, total arterial resistance was reduced, and characteristic impedance was decreased.(Adapted from Westerhof et al, [9] and Lin et al, [10])

2.10 Windkessel Approximation of Impedance Spectra

The three-element Windkessel approximation can serve as an estimate of the arterial impedance spectra thereby providing an estimate of an entire systemic arterial tree beyond where pressure and flow are measured [9]. The three parameters (i.e. elements) have physiological meaning (**Figure 6**). Rc represents the combined influence of the resistance, compliance and inertance for the proximal artery of interest. For the purposes of the current project, Rc is the local resistance of the vessel undergoing

stenting. C is the arterial capacitance defined as the relationship between blood volume in a segment of vasculature and the pressure distending the vascular walls, and accounts for the sum of the compliance of all arteries beyond the region of interest. For intermediate frequencies the modulus decreases, and the phase angle is negative because of the compliance contribution. At higher frequencies, the modulus approaches a constant value and the phase angle is close to zero. Rp describes the total peripheral resistance, predominantly at the level of the arterioles having their greatest impact at zero frequency. Systemic resistance or total vascular resistance represents the opposition to blood flow within the entire systemic vasculature and is primarily determined by arterioles in the absence of pronounced vascular stenoses, and is therefore the sum of Rc and Rp. When determined downstream of the ascending aorta, total vascular resistance is often called the terminal resistance, and is expressed as the ratio of mean pressure divided by mean flow for the given location.

The three-element Windkessel approximation extends the two-element Windkessel by adding the characteristic impedance [88]. The reason this element has been introduced is because at high frequencies, a constant impedance modulus and a phase angle of about zero degrees have been observed during measurement that is not represented well by the two-element Windkessel approximation showing a continuously decreasing modulus and phase angle to -90°.

The Windkessel parameters will be used to represent the behavior of a vascular network in the current investigation including the function of central elastic arteries (referred to as arteries with a large amount of elastin filaments such as the thoracic aorta and carotid arteries), muscular and conduit arteries (abdominal aorta, iliac and femoral

arteries) and resistance arteries (**Table 2)**. For example, Rp in the Windkessel approximation can represent arterioles since they are the source of most of the resistance in the cardiovascular system.

As mentioned in publications from our laboratory and others, Rc, C, and Rp can be determined from clinical or experimental techniques and then applied at the outlet of CFD models of the stented region to quantify how changes in DVR occurring in response to T2DM may adversely alter hemodynamics and correlate with NH [89, 90].

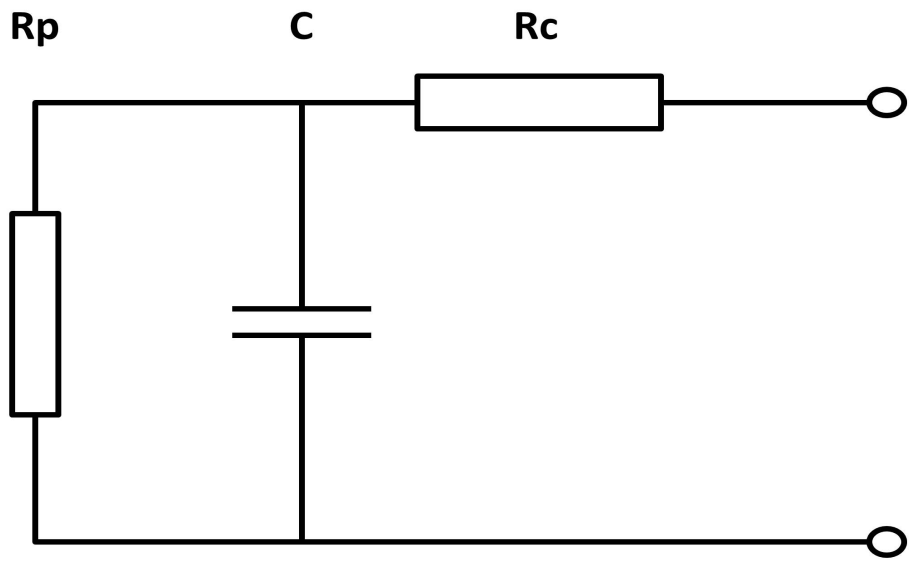

Figure 6. The three-element Windkessel model. Rp describes the peripheral resistance, C is the arterial capacitance, and Rc represents the resistance of the local artery of interest.

Arteries	Radius (mm)	Range of k	Classification	Represent
Thoracic aorta Carotid arteries	0.5~20	2.4~2.65	Central elastic arteries	C
Abdominal aorta Iliac and femoral arteries	0.25~0.5	2.65~2.9	Muscular and conduit arteries	Rc
Arterioles	0.005~0.25	2.75~3	Resistance arteries	Rp

Table 2. Arteries of interest for the current investigation along with their general classification and representation by elements of the Windkessel approximation.(Adapted from Zamir et al. [2])

2.11 Computational Fluid Dynamics

CFD is a simulation tool that can be used with vascular models created from medical imaging data to compute and visualize hemodynamic indices including WSS. There are several steps involved, such as creating a representation of a vessel's geometry (subject-specific or idealized), meshing this vessel geometry, specifying rheological properties such as blood density and viscosity, prescribing the hemodynamics state at the entrance and exit of vessels (known as boundary conditions), and using a powerful computer to solve equations for the conservation of mass (continuity equation) and balance of fluid momentum (equation of motion).

An expression for conservation of mass [91] can be developed by performing a mass balance over a stationary volume element through which a fluid is flowing.

It can be expressed mathematically as:

$$\frac{\partial \rho}{\partial t} + \frac{\partial (\rho u_x)}{\partial x} + \frac{\partial (\rho u_y)}{\partial y} + \frac{\partial (\rho u_z)}{\partial z} = 0$$

Where ρ is the fluid density, and u_x, u_y, u_z are the directional x, y, and z components of the velocity vector.

The equations of motion for an incompressible Newtonian fluid are referred to as Navier-Stokes [92].

The Navier-Stokes equations in cylindrical coordinates can be expressed as:

$$\rho\left(\frac{\partial u_x}{\partial t} + u_x\frac{\partial u_x}{\partial x} + u_y\frac{\partial u_x}{\partial y} + u_z\frac{\partial u_x}{\partial z}\right) = -\frac{\partial p}{\partial x} + \rho g_x + \mu\left(\frac{\partial^2 u_x}{\partial x^2} + \frac{\partial^2 u_x}{\partial y^2} + \frac{\partial^2 u_x}{\partial z^2}\right)$$

$$\rho\left(\frac{\partial u_y}{\partial t} + u_x\frac{\partial u_y}{\partial x} + u_y\frac{\partial u_y}{\partial y} + u_z\frac{\partial u_y}{\partial z}\right) = -\frac{\partial p}{\partial y} + \rho g_y + \mu\left(\frac{\partial^2 u_y}{\partial x^2} + \frac{\partial^2 u_y}{\partial y^2} + \frac{\partial^2 u_y}{\partial z^2}\right)$$

$$\rho\left(\frac{\partial u_z}{\partial t} + u_x\frac{\partial u_z}{\partial x} + u_y\frac{\partial u_z}{\partial y} + u_z\frac{\partial u_z}{\partial z}\right) = -\frac{\partial p}{\partial z} + \rho g_z + \mu\left(\frac{\partial^2 u_z}{\partial x^2} + \frac{\partial^2 u_z}{\partial y^2} + \frac{\partial^2 u_z}{\partial z^2}\right)$$

Where g represents the gravitational acceleration, p is the fluid pressure, and ρ is the fluid density.

2.12 Indices of WSS Contributing to NH

WSS represents the tangential component of shear force exerted on a vessel wall by the flow of a viscous fluid. WSS is an important factor that impacts endothelial cell function and flow-induced remodeling. This process allows WSS to be maintained within a preferential range for a given portion of the vasculature under normal conditions[93]. Low WSS is thought to promote atherogenesis and NH. Together with members of the current dissertation committee, our lab has demonstrated that areas of low WSS

established after stenting modulate the development of NH in rabbit iliac arteries [5]. As NH occurs within a stent, the geometry and associated WSS distributions change over time in a way that progressively alleviates the deleterious WSS distributions that were created initially by stenting (**Figure 7**). Additional studies by the same team complemented these findings by further demonstrating that geometric properties of an implanted stent may contribute to adverse WSS that is associated with NH [5]. These findings suggest that WSS can impact NH locations, but this relationship may also be influenced by associated vascular changes driven by AGEs.

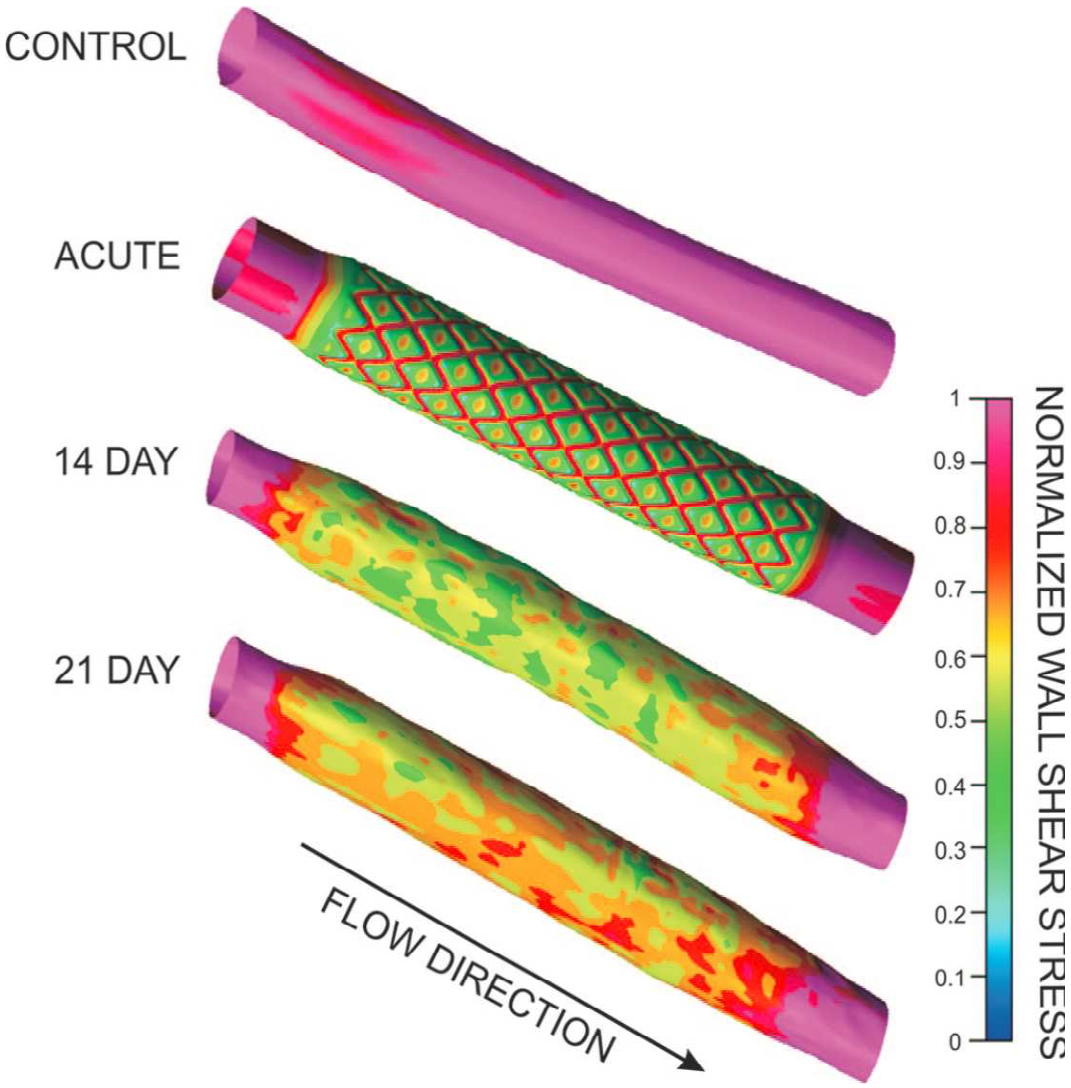

Figure 7. Distributions of normalized WSS in control and stented rabbit iliac arteries. The theoretical distribution of normalized WSS after stenting (i.e. acute) is progressively alleviated after 14 and 21 days to restore values back toward a preferential value. (Adapted from LaDisa et al, [5])

2.13 Molecular Pathways Impacting NH Formation

TGFβ is a growth factor having widespread cytokines related effects on cell growth and development. TGFβ is involved in the wound healing process, and the TGFβ gene has been shown to be activated in human restenotic lesions as well as after porcine coronary artery stenting [94, 95]. Similarly, when the TGFβ gene was transferred into

normal porcine arteries, NH was enhanced [96]. Together these findings suggest that monitoring the protein expression of AGEs, RAGE, and TGFβ may identify the contributions of these molecular mediators to the mechanisms of restenosis in T2DM.

RAGE is a signal transduction receptor in the immunoglobulin superfamily that is expressed in endothelial cells, monocytes, and renal mesangial cells [97]. The interaction of AGEs and RAGE activates phosphorylation of nicotinamide adenine dinucleotide phosphate oxidase subunits and intracellular signaling molecules: PKC, nuclear factor-kappa B (NF-kB), and TGFβ influence ROS and nitric oxide (NO) formation (**Figure 8**) [6, 98]. Because reactions between AGEs and RAGE may increase inflammation, RAGE is a major pharmacological target for inhibition of AGEs.

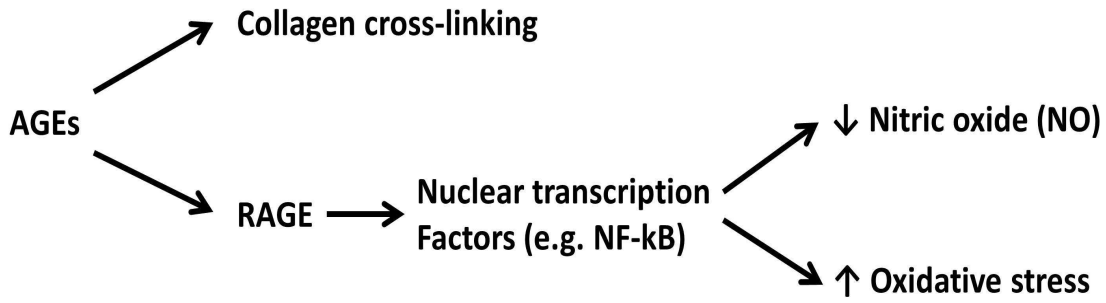

Figure 8. AGEs related pathways. The interaction of AGEs and RAGE activates nuclear transcription factors and further influences oxidative stress and nitric oxide (NO) formation (Adapted from Welt et al, [6])

ROS are chemicals containing oxygen ions and peroxides which are highly reactive due to the presence of unpaired electrons such as oxygen radical, superoxide ion radical, hydroxyl radical, and nitric oxide radical [11], as these are formed as an unavoidable byproduct of cellular respiration. However, under conditions of

environmental stress, ROS levels can significantly increase resulting in damage to cellular structure. Compared to ROS, antioxidants are a group of chemicals such as ascorbic acid (vitamin C), α-tocopherol (vitamin E) and superoxide dismutase that prevent pro-oxidation processes or biological oxidative damage [99]. More specifically, there are several intrinsic radical scavenger systems in organisms which occur through enzymatic and non-enzymatic reactions. Enzymatic antioxidants include superoxide dismutase, glutathione peroxidase, and catalase which will convert superoxide radicals to water [100-102]. Non-enzymatic antioxidants include vitamin C, vitamin E, glutathione and β-carotene [103, 104]. Glutathione is a major endogenous antioxidant produced by the cells as it directly participated in neutralizing ROS and maintaining vitamin C and E in their reduced forms [105]. Organisms need to maintain a balance between ROS and antioxidants as shown in **Figure 9**. If more ROS are generated, this is defined as oxidative stress and leads to oxidative damage. Conversely, if more antioxidants are produced, this is defined as reductive stress and could cause damage as well.

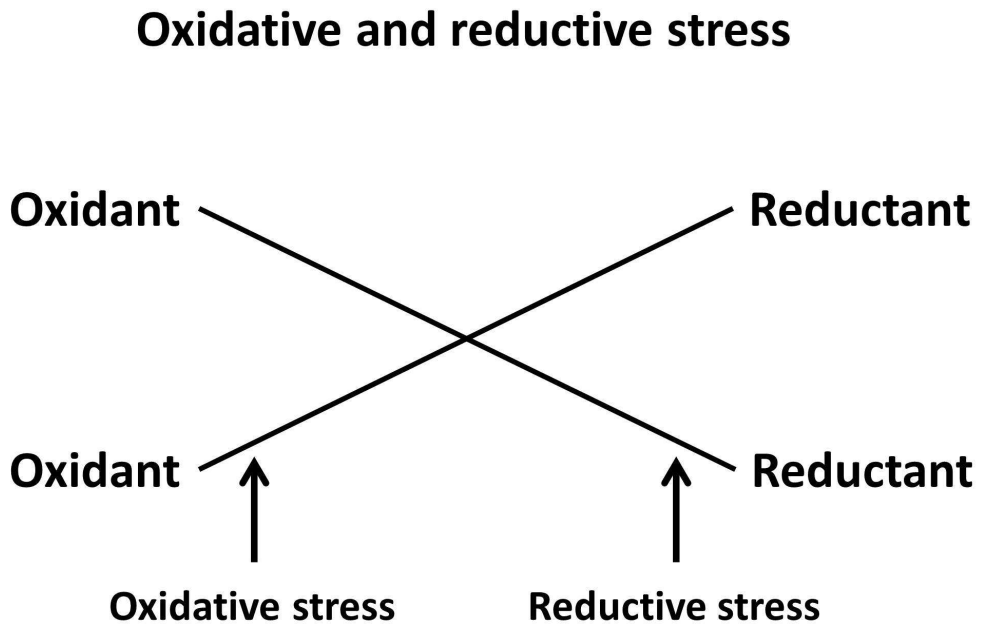

Figure 9. Illustration of the balance between oxidative and reductive stress (Adapted from Kohen et al. [11])

Studies revealed that AGEs and RAGE interaction can influence ROS and nitric oxide (NO) pathways, which are related to preferential endothelial coverage after a stenting procedure [6]. It has also been found that high extracellular glucose conditions significantly increase ROS and AGEs formation in human cardiac myocytes [106], and ROS might significantly influence cellular functions [107]. Yan et al. [108] found that reducing ROS production and improving endothelial NO synthase protein and activation will chronically increase local BF. Glucose oxidation is a major pathway for producing free radicals [109]. In addition, another important source of free radicals is from the reaction process of glucose with proteins to form Amadori products, AGEs and the interaction of AGEs with RAGE [110, 111]. Increased oxidative stress is associated with

the progression of diabetes and its complications [110, 112]. Although ROS and NO are undoubtedly related to the stenting process, they were not included in this research because of its main focus on detecting upstream NH by changes in downstream AGEs and RAGE reactions specific to T2DM.

2.14 Mechanisms of NH after Stenting

There are several mechanisms that have been shown to be involved with NH to date. These pathways are briefly discussed for completeness and to convey awareness of mechanisms that are beyond the scope of those queried in the current investigation. The first is the TGFβ pathway mentioned above [113]. TGFβ family is highly conserved with TGFβ 1-5 having similar functions. Only the first three isoforms are expressed in mammals. During the stenting process, it is very important that the balance between TGFβ activation and inhibition be maintained. Anti-TGFβ has been used to treat restenosis such as the cell-membrane molecule mannose-6-phosphate being injected at the time of stenting. Reduced scarring, decreased inflammatory cell infiltrate, and angiogenesis were observed [114].

The mitogen-activated protein kinase (MAPK) pathway has also been shown to contribute to NH. It has been shown that hyperinsulinemia activates the MAPK pathway inducing NH after balloon injury in diabetics [115]. Additional research found that vessel smooth muscle proliferation by AGEs was due to the phosphorylation of extracellular signal-regulated kinases (ERK) and p-38 which are important factors in MAPK pathways [116].

In the NH process, there is a balance between medial SMC growth and apoptosis in media. After injury due to stenting, medial SMC migrate into the intima by matrix

metalloproteinases (MMP2 and MMP9) [117]. G-proteins subunits have also been found to significantly increase in this early reaction to stenting, which coincides with the period of medial SMC mitogenesis and NH formation [118]. G-protein pathways are important during the membrane transduction process with many receptors involved, and they can also active MAPK which are associated with SMC proliferation during stenting injury process as mentioned above [118].

2.15 AGEs Related Collagen Cross-linking Breaker: ALT-711

ALT-711 is the first drug in a new class of thiazolium therapeutic agents to break established AGEs related collagen cross-linking [119]. Animal investigations have shown that AGEs cross-linking is one of the factors in vascular stiffening, and ALT-711 can reduce artery stiffness and left ventricular mass, while enhancing cardiac output, [120, 121] suggesting this compound may have the ability to reduce NH in response to stenting in T2DM.

Freidja et al. [122] used the AGE-breaker ALT-711 with T2DM rats, and the authors found that breaking AGEs through ALT-711 not only improved endothelial function, but also improved local BF supply and hence prevented end organ damage. ALT-711 can target the biochemical pathway by breaking the –C=O – O=C- bond in AGEs and prevent this connection from forming again. It is therefore expected that ALT-711 can also reduce at least a part of early AGEs formation in arteries of ZDF rats, which will likely decrease arterial stiffness.

2.16 Impact of Downstream Vascular Changing on Upstream Stenting

Since AGEs formation occurs more rapidly in diabetic conditions, it will likely increase collagen cross-linking and modify vessel structures leading to increased distal resistance, as well as decreased arterial capacitance. As alluded to in the Specific Aims, these changes are referred to as the mechanical pathway for the current work (**Figure 10**). As AGEs increases, it may interact with RAGE to further induce nuclear factor activation and TGFβ expression, and these changes will likely impact vessel structure and cause NH. These changes are referred to as the molecular pathway of the current work. Although previous studies have shown that TGFβ expression is correlated with NH formation [95], it is still not clear whether AGEs induced collagen cross-linking and structural modification that primarily influences vessels downstream is responsible for exacerbating NH in the stented region. **Figure 10** depicts this interaction and the potential for molecular as well as mechanical contributions applicable to the current investigation. ALT-711 was used as a potential agent to mitigate NH, and determine whether its actions work by decreasing collagen cross-linking or through decreasing AGEs and RAGE interaction.

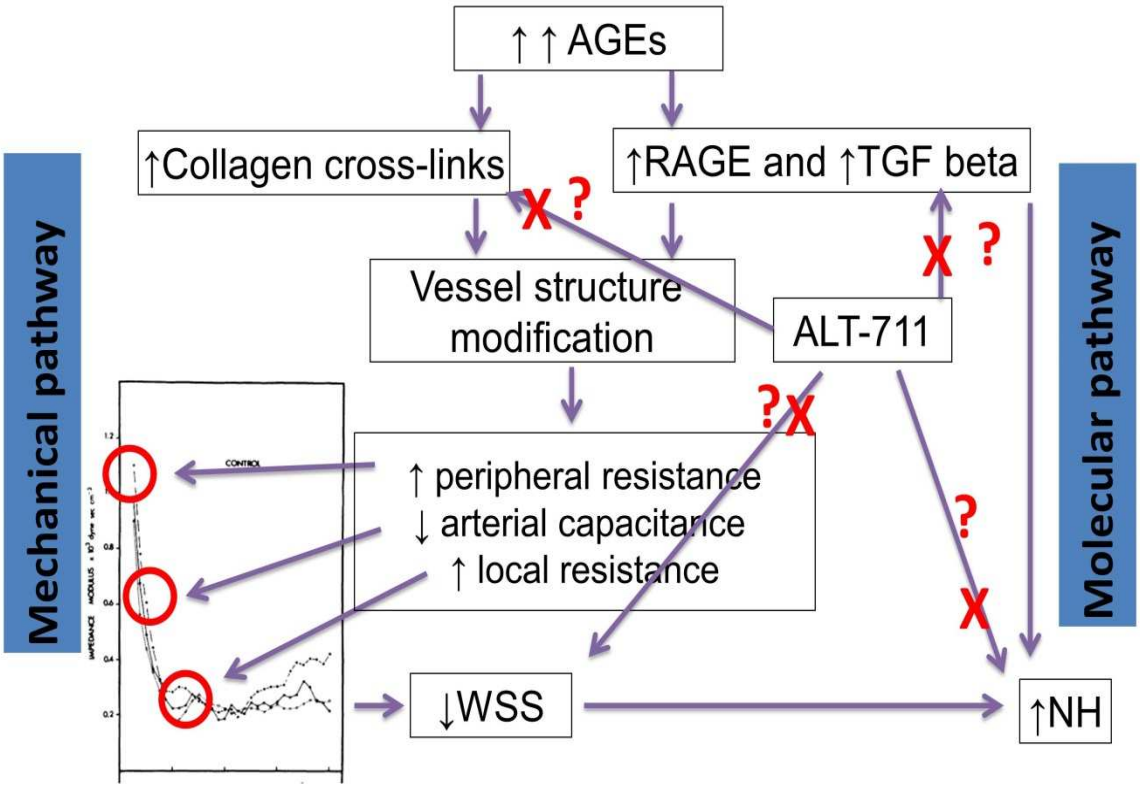

Figure 10. Mechanical and molecular pathways tested as part of the current investigation. The mechanical pathway refers to changes predominantly mediated by AGE formation increasing collagen cross-links and modifying vessel structures that lead to increased peripheral resistance as well as decreased arterial capacitance and WSS. The molecular pathway refers to changes predominantly mediated by increased expression of AGE, RAGE and TGFβ leading to structural vascular alterations. "?" indicates a potential interaction while "X" indicates a location of potential inhibition by ALT-711 that was tested as part of the current investigation.

CHAPTER 3: METHODS COMMON TO ALL AIMS

3.1 Experimental Protocol

Zucker diabetic rats were obtained from Charles River Laboratories International Inc., (Wilmington, MA). These rats were created from inbreeding of hyperglycaemic Zucker obese rats having a *fa* gene mutation in the extracellular domain of the leptin receptor [123], which leads to impaired leptin signaling resulting in obesity as well as elevated plasma cholesterol and triglyceride levels [124]. These symptoms closely replicate the regular T2DM disease process which results from insulin-resistant to insulin-deficient states [125]. To isolate the influence of T2DM on NH, obese rats were studied as well, resulting in groups of ZL, ZO, and ZD rats.

All experimental procedures and protocols used in this work were approved by the Animal Care and Use Committee of Marquette University (AR-200; PI: J. LaDisa) and the Medical College of Wisconsin (AUA-672; PI: J. Kersten). The experimental protocol is shown in **Figure 11**. Stents were deployed into the AAo of male ZL, ZO and ZD rats in the absence (N=9/group) or presence of ALT-711 (i.e. treatment; N=9/group). After 21 days, three rats from each group were randomly selected to have their AAo undergo casting, microfocal x-ray CT imaging and reconstruction for potential use with CFD simulations. Remaining rats in each group underwent quantification of NH, AGEs related collagen cross-linking, and protein expression by Western blotting. Additional details are provided below.

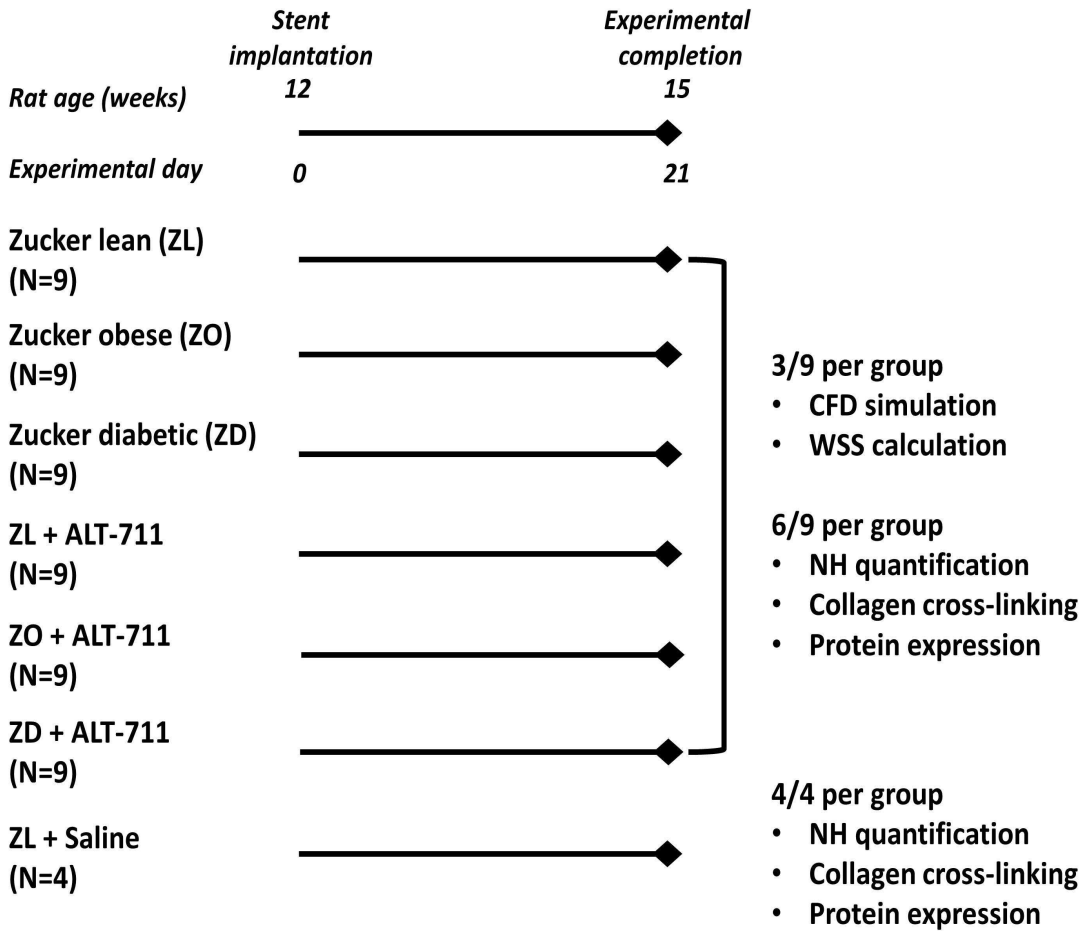

Figure 11. Schematic illustration of the experimental protocol. Stent implantation was performed at 12 weeks for lean, obese and diabetic rats in the absence and presence of ALT-711 administered using osmotic minipumps. After 21 days, rats were randomly selected for estimation of wall shear stress (WSS) by computational fluid dynamics (CFD) modeling (N=3/group) where applicable as described below, or quantification of neointimal hyperplasia (NH) and protein expression (N=6/group). An additional group of rats (n=4) underwent stenting and administration of saline alone to reveal any potential influence of the minipump and vehicle for ALT-711.

3.2 Experimental Preparation

ZL, ZO and ZD rats were allowed a minimum of 48 hours to acclimate after arrival, and rats were selected randomly for stenting at 12 weeks of age. Stent implantation was performed under anesthesia and sterile conditions as discussed below.

Rats were anesthetized in a transparent induction chamber using isoflurane through a vaporizer. Once the rat was anesthetized, it was removed from the chamber, placed on a warm surface and fitted with a nose cone attached to an anesthetic vaporizer and oxygen source. The concentration of anesthesia was then reduced to a level which maintains the proper plane of anesthesia; typically between 0.5 and 3% of isoflurane.

3.3 Stent Implantation

AAo stenting was performed under anesthesia and sterile conditions similar to that described previously [66, 126]. Local blood flow patterns, and the subsequent severity of NH, are influenced by geometric attributes of an implanted stent [5]. Therefore, 316L stainless steel balloon expandable stents specially suited for the rat AAo (2.5x8mm) and with a known geometric pattern (**Figure 12**) were purchased from Burpee Materials Technology (Eatontown, NJ) and crimped on 2.5x12mm rapid-exchange delivery catheters (Polymerex; San Diego, CA).

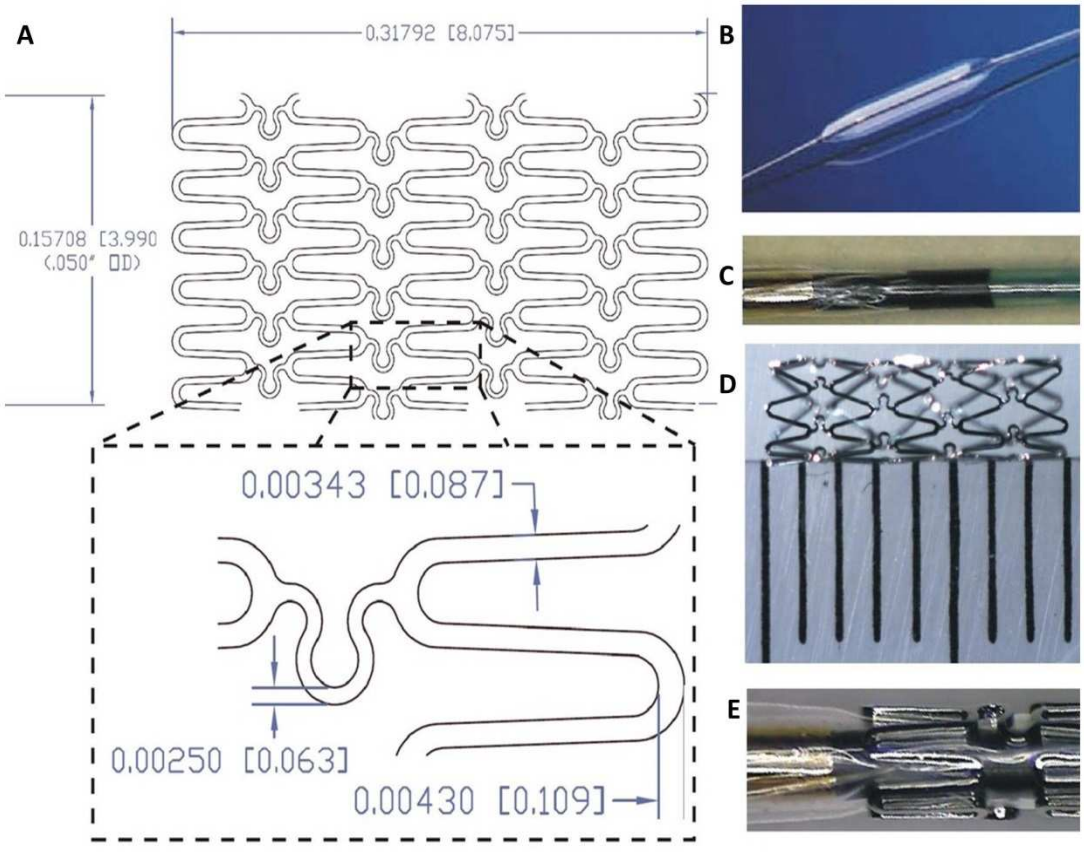

Figure 12. 316L stainless steel balloon expandable stent specially suited for small dimensions (2.5x8 mm) and with a known geometric pattern (A) for use with 2.5x12 mm rapid-exchange delivery catheters (B and C) obtained from Polymerex (San Diego, CA) were created in conjunction with Burpee Materials Technology (D; Eatontown, NJ) and crimped (E) prior to sterilization and use.

In preparation for stenting, the site over the AAo and iliac arteries was shaved and cleaned. The skin was then entered by a mid-sagittal incision. Under microscopic view, the AAo and iliac arteries were carefully separated free from surrounding vessels and tissue using sterile applicators. Small aortic side branches were temporarily clamped to limit the backflow of blood. Two vascular clips were placed to isolate the region undergoing stenting close to the aorta-iliac bifurcation. A small incision was made in the end of the isolated segment and blood in this section was removed by rinsing with

heparinized saline (100U/kg) to prevent acute thrombosis. The tip of a delivery catheter and associated guide wire were inserted. Aortic clamps were then briefly removed as necessary to thread the stent to an infrarenal segment of the AAo. The stent delivery catheter was then inflated to securely anchor the stent against the AAo wall using a stent-to-artery size ratio range of 1.1 to 1.2:1 [127]. Successful deployment was confirmed visually as the stent could be viewed through the aortic wall. After removal of the stent delivery catheter, the incision was closed using an 8-0 suture. The vascular clips were then removed; the abdomen was closed with 4-0 silk suture while the skin was closed with 4-0 dissolvable Vicryl suture using stitches just below the skin.

3.4 Surgical and Post-operative Care

Quantitative criteria including oxygen saturation, respiration rate, temperature, heart rate, mucous membrane color and capillary refill time were continuously monitored during the surgical procedure and for 3-4 hours after its completion. Buprenorphine (0.05 mg/kg, intraperitoneal (IP)) was used as analgesia for 2 days. Animals also received antibiotic prophylaxis (20 mg/kg cefazolin, IP) for 4 days, and aspirin in their food or drinking water (20 mg/day) for the duration of the experimental protocol to inhibit thrombus formation.

3.5 ALT-711 Treatment

ALT-711 is the first drug in a relatively new class of thiazolium therapeutic agents to separate established AGEs related collagen cross-linking [119]. This chemical was developed by Alteon Corporation, who later exhausted their operating cash forcing the chemical to halt testing in Phase II clinical trials [128]. There is no official

documentation on the half-life of ALT-711; however, discussions with the manufacturer (Iron-dragon, Newport Beach, CA; www.iron-dragon.com), from whom the compound was purchased, suggests the half-life of this chemical is approximately 6 hours. Hence, the concentration of ALT-711 in the blood would decrease to 6% within 24 hours. There are two ways ALT-711 has been administered to rats by previous researchers: IP injections or direct feeding. Since the IP method (1mg/kg/day) is difficult to administer in rats, other researchers administered ALT-711 to rats by feeding (10mg/kg/day) [31, 129, 130].

In this investigation, treated rats from each group were given ALT-711 (1mg/kg/day) by ALZET osmotic minipump (model 1004; Cupertino, CA) based on previous research [131]. The ALZET osmotic minipump has been used previously in drug delivery studies [132, 133], and it works to deliver drugs at a constant rate to the intended site based on establishing an osmotic pressure gradient from within the minipump. Cooper et al. [132] found that the osmotic minipump system for microdialysis samples can generate flow rates that are similar to a microdialysis syringe pump. In addition, Cooper et al. [132] tested the chemical released from the osmotic minipump and confirmed that osmotic minipump is a viable method for microdialysis sampling.

Because the osmotic minipump releases the drug continuously, it will maintain the ALT-711 blood concentration at a uniform level throughout the day relative to the IP injection method for which the drug concentration is decreased by half every 6 hours. Osmotic minipumps were therefore used according to the manufacture's literature and data specification (**Figure 13 and Table 3**). Briefly, saline was used to solve ALT-711 at a high concentration using the 100 μL limit of the minipump. The ALT-711 amount was

calculated based on the pumping rate (0.11μL/hour), the weight of rats, desired 1mg/kg/day dose and an experimental duration of 21 days. The total amount of chemical for 28 days was loaded into osmotic minipump as calculated below to ensure enough ALT-711 was present for the full experimental duration.

$$Saline\ amount = 0.11\frac{\mu L}{hour} \times 24\ hour \times 28\ day$$

$$ALT-711\ amount = \frac{dose}{day} \times Rat\ weight\ in\ kg \times 28\ day$$

All minipumps were equilibrated for 24 hours before implantation according to the manufacture's literature to ensure the drug was released and effective immediately after surgery. Prior to closing the skin at the conclusion of the stenting procedure, a minipump was filled, placed just beneath the first muscle layer in the abdomen, and positioned with its delivery portal facing toward the cranial end of the animal. All other procedures were the equivalent to those described above.

3.6 Osmotic Pump Vehicle

In addition to using osmotic minipumps loaded with ALT-711, four additional ZL rats were subjected to minipumps loaded with vehicle (i.e. saline), which was used as the solvent for ALT-711, to account for the possible effect of the osmatic minipump in the treatment group and confirm the feasibility of delivering ALT-711 by this approach. **Figure 11** shows the experimental procedures with osmotic minipump control.

Figure 13. ALZET Osmotic Miniumps. (Adapted from ALZET, Cupertino, CA)

ALZET Osmotic Minipump	
Model Number	1004
Reservoir Volume (µl)	100
Length (cm)	1.5
Diameter (cm)	0.6
Approximate Minipump Weight (g)	0.4
Total Minipump Displaced Volume (ml)	0.5

Table 3. Approximate values used with osmotic minipump model 1004. Loading values in reservoir varied slightly depending on the weight of a given rat. (Adapted from ALZET, Cupertino, CA)

3.7 Statistical Analysis

Statistical analysis was conducted using one-way multiple analysis of variance (ANOVA) followed by Tukey-Kramer multiple comparison test. Changes within and between groups were considered statistically significant when $P<0.05$. Data are expressed as means ± standard error of the mean (SEM).

CHAPTER 4. SPECIFIC AIM 1: QUANTIFY THE ABILITY OF AGE-MEDIATED VASCULAR CHANGES TO INCREASE DVR AND ALTER MECHANICAL INDICES KNOWN TO PROMOTE NH IN TYPE 2 DIABETES, AND DETERMINE WHETHER THESE ADVERSE CHANGES CAN BE ALLEVIATED BY ALT-711.

4.1 Review of Rationale Applicable to Aim 1

Adverse vascular adaptations are known to occur in response to T2DM. These changes can manifest as increased central and peripheral vascular stiffness, and elevated DVR if the distal vasculature is similarly affected. This aim tests the hypothesis that increases in AGEs related collagen cross-linking and DVR cause alterations in BF dynamics within the upstream stented region in ZD rats compared to normoglycemic controls. ALT-711 is an AGEs related collagen cross-linking breaker shown to decrease vessel resistance and atherosclerosis [29, 30]. This aim therefore further tests the hypothesis that giving ALT-711 to stented ZD rats decreased DVR and elevated WSS compared to untreated ZD rats. CFD simulations were conducted to compare TAWSS of ALT-711 treated ZDF stented rats with corresponding untreated groups.

4.2 Methods Unique to the Current Aim

4.2.1 Hemodynamic Data Acquisition

Twenty-one days after stenting, rats were anesthetized as described in the general methods section and the right carotid artery was isolated. A fluid-filled catheter connected to a BP transducer (APT300; Harvard Apparatus, Holliston, MA) was calibrated and inserted from the carotid artery into the aorta for measurement of BP and subsequent potential use in the CFD modeling process. The AAo was also dissected free from connective tissue and the vena cava. BF proximal to the stent was recorded with a

transit-time flow probe connected to a flow meter (Model T106, Transonic Systems, Ithaca, NY). BP and BF data was sampled at 120Hz simultaneously using an analog-to-digital (A/D) converter (model DI-158, DATAQ instruments, Akron, OH) interfacing with a laptop running WINDAQ software (DATAQ instruments) **(Figure 14)**. Rats were then euthanized by overdose of pentobarbital sodium (100 mg/kg, Intravenous (IV)).

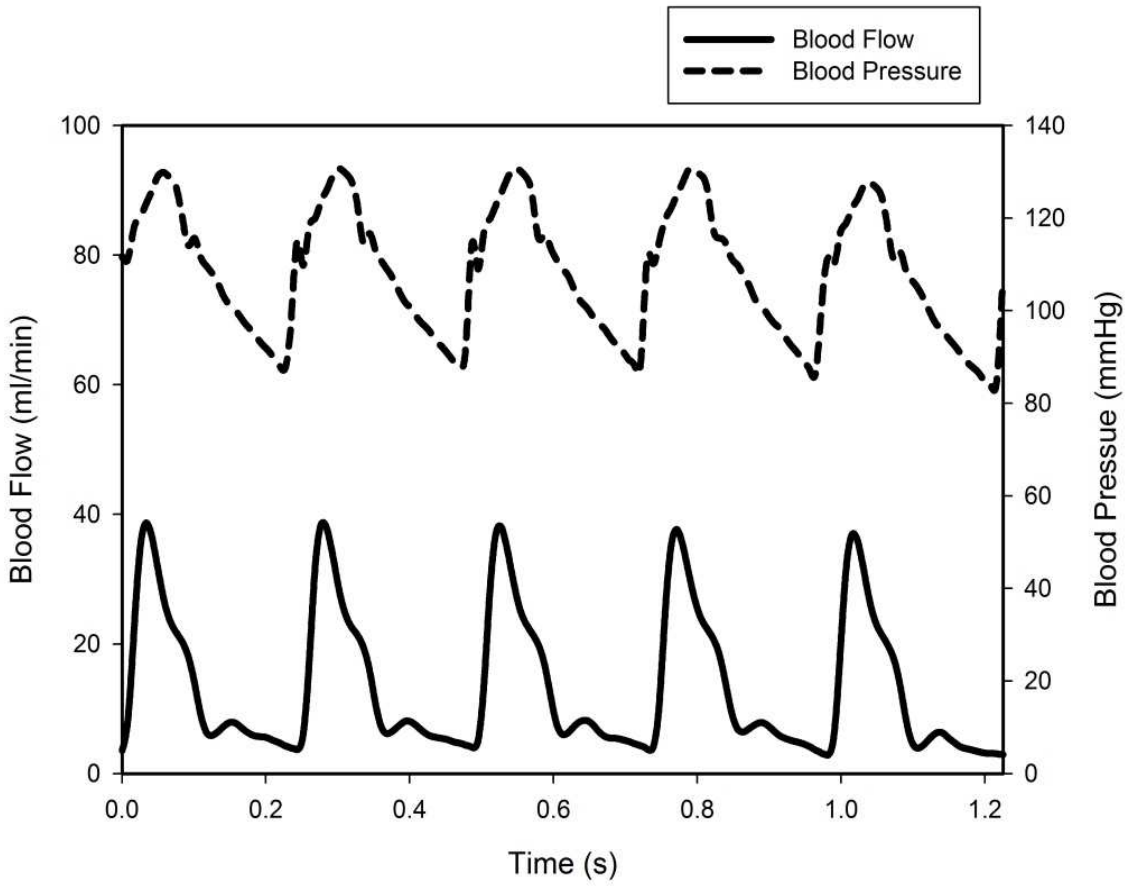

Figure 14. Blood flow (ml/min, solid line) and blood pressure (mmHg, dashed line) were recorded using WINDAQ software. The software was calibrated first, and settings were adjusted to optimize the dynamic range of the signals.

4.2.2 Plastic Casting of the Stented Flow Domain

Computational modeling of regional BF through arterial segments requires high resolution morphological data to represent the vascular flow domain of interest. Microfocal x-ray computed tomography can capture detailed geometric information through plastic casting of the stented flow domain, and this technique has previously been used to examine the correlation between altered indices of TAWSS and NH after stent implantation in rabbit iliac arteries [5].

The AAo above the stented region was therefore carefully dissected from connective tissue of rats in the current investigation after euthanasia. A small incision was made in the suprarenal AAo under microscopic guidance and a catheter containing Batson's No. 17 Corrosion Compound (Polysciences, Warrington, PA) was secured within the vessel [5]. A four way stopcock was connected to the catheter and the BP transducer mentioned above. A syringe was then connected to the open end of the stopcock to flush the vessel with saline before the plastic compound was injected and maintained at the measured mean BP for each rat. Care was taken to ensure no bubbles were injected and a constant mean BP was maintained thereby capturing the geometric intricacies of the flow domain. After curing (2-3 hours), the artery and connective tissue were caustically removed with Batson's #17 Maceration solution. At this point the stent can be freely removed since the external vessel against which it had been implanted, and the tissue that had grown within it since implantation, have been removed leaving a cast of the flow domain.

TAWSS was calculated by two methods using the casted flow domain representations: regional TAWSS and intrastrut TAWSS. Regional TAWSS was

calculated as indicated below assuming blood behaves as a Newtonian fluid and the vessel wall is rigid after stenting.

$$\text{Regional TAWSS} = \frac{4\mu Q}{\pi r^3}$$

where *Q* is the mean measured flow rate, viscosity was assumed to be 6.2 cP [76], and *r* is the radius determined from an average of three digital micrometer measurements of the casted stented region. To preserve funding resources, intrastrut TAWSS was also calculated using microfocal x-ray CT imaging, but this approach was only performed for the collection of treated or untreated rats for which the estimate of regional TAWSS yielded results that were significantly different from those of untreated ZL rats (**Table 4**).

TAWSS (dyn/cm^2)	ZL	ZO	ZD
No treatment	22.0 ± 1.48	12.8 ± 1.52	9.72 ± 3.68*
ALT-711	18.0 ± 2.19	17.8 ± 2.82	17.5 ± 1.43

*Table 4. Regional TAWSS (dyn/cm^2) from ZL, ZO and ZD stented rats (N=3/group). Mean ± SEM; * = significant difference between ZD and ZL stented rats. No significant difference was found after ALT-711 treatment.*

4.2.3 Microfocal X-ray CT and Vascular Reconstruction

Casts of the stented region were imaged using a microfocal x-ray CT imaging system as previously described [5] where applicable. Briefly, casts were placed on a rotating and translating stage within an X-ray beam **(Figure 15)**. Thirty images were captured and averaged to generate a single image (512 X 512 pixels) at each of 360 rotation angles obtained in one-degree increments (**Figure 16**). The images were then

aligned along the center of rotation and processed to remove any spatial and temporal heterogeneity within the x-ray beam.

The averaged and processed images from each rotation were rendered to produce isotropic volumes (497^3) [117]. Optimal settings for collecting data were 40 mV and 140 μA based on previous experiments. The source to artery distance and the X-ray source to the image intensifier distance were kept constant when acquiring image data for all rats (18.9 cm and 87.0 cm, respectively). A polyethylene tubing of a known diameter was inserted at the base of each cast for use in calibration during reconstruction. Reconstruction volumes were rendered using SAO Image DS9 (Version 2.1b6) on a 1.8 MHz Compaq Presario 900 laptop with 1Gbyte of RAM running Mandrake Linux.

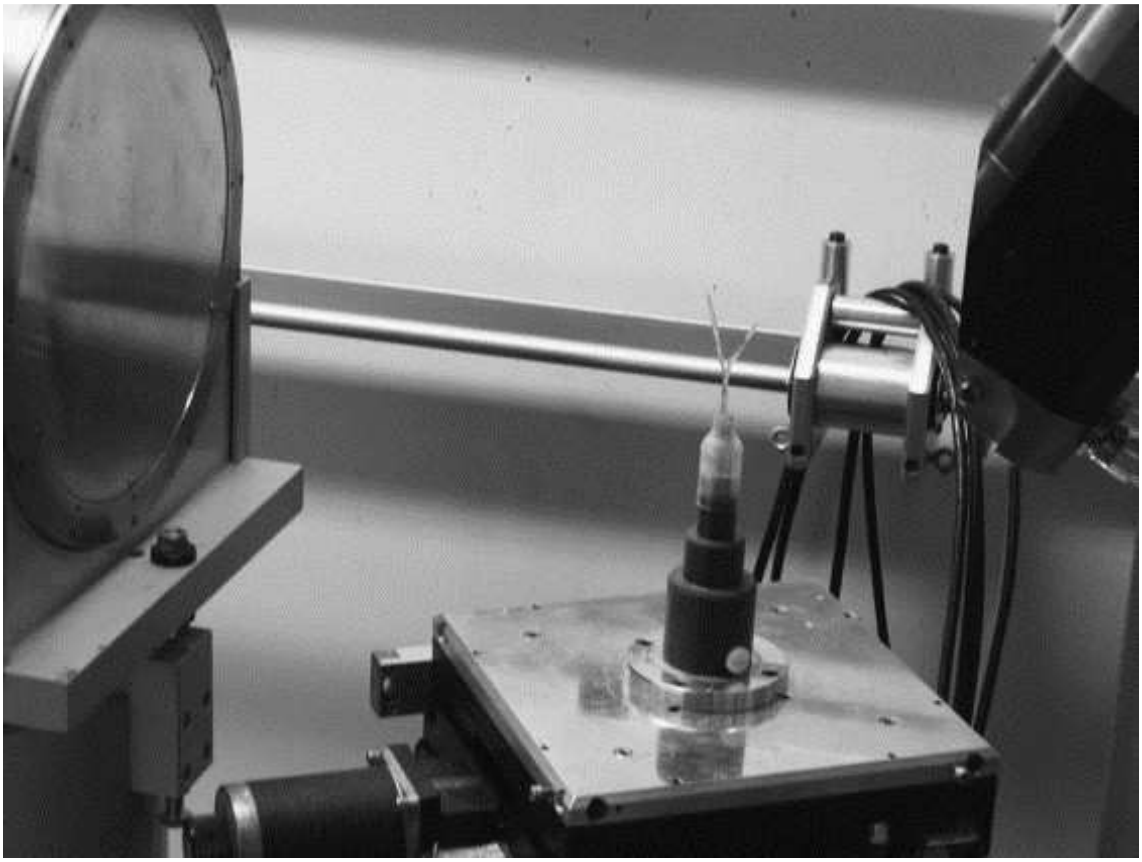

Figure 15. Image of the microfocal x-ray CT imaging system and cast of a rabbit abdominal aorta and iliac arteries. (Adapted from LaDisa et al, [12])

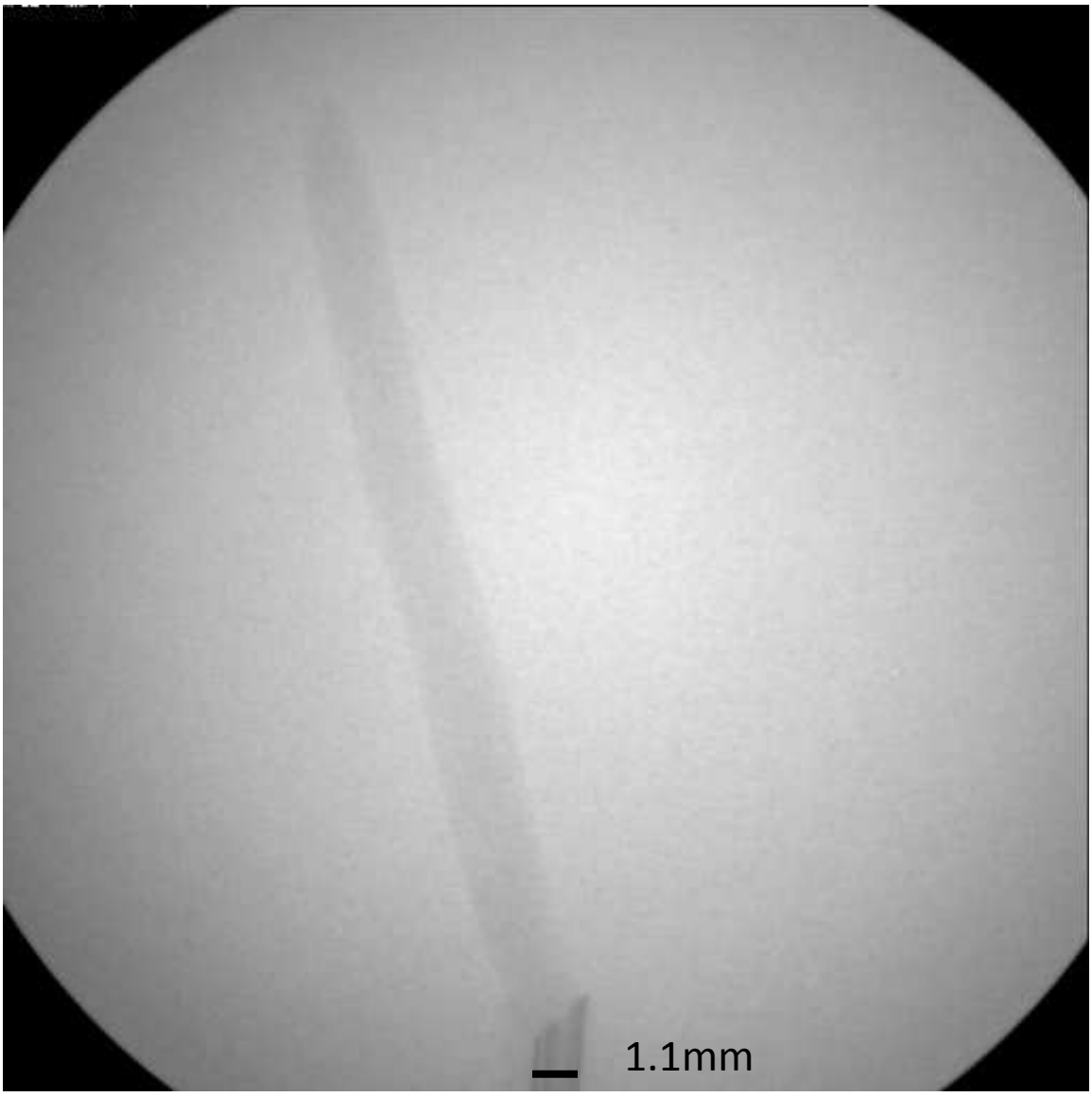

Figure 16. Projection image obtained for the abdominal aorta of a representative rat from the current work. Three hundred and sixty of these images were captured for each casted abdominal aorta in one degree increments to generate isotropic reconstruction volumes. The diameter of the catheter (1.1mm) was used as a scale for calibration.

After ensuring the reconstructed images were without artifacts such as shading around the vessel of interest caused by carelessness in the reconstruction process (**Figure 17**), the reconstructed volumes were loaded into ImageJ (NIH; http://rsb.info.nih.gov/ij/) as raw by selecting width as 497 pixels, height as 497 pixels and 497 images. The raw

reconstructed volumes were digitally sectioned perpendicular to the axis of rotation to generate 497 unsigned 8-bit integer arrays using Unix script files, and additional post-processing of vessel segments was performed as previously described [12]. Briefly, the polyethylene tubing was first used to calibrate the voxel size. Images within the stented region were selected and adjusted to use the full dynamic range (0-255 grayscale levels), and an image threshold was implemented using an automated Matlab program to generate vessel segments from each image slice. Image contours were extracted from each image slice to resolve the vessel wall. To determine the number of circumferential points used in this process, a slice having pronounced concave or convex attributes around its circumference was selected for comparison to versions of the slice with 48, 96, or 120 interpolated circumferential points. Processing was implemented to smooth the circumferential points, but also maintain local geometric features as discussed in detail elsewhere [12]. A z-spacing of 1 (i.e. every reconstructed slice was used) helped to capture detailed geometric information in the longitudinal direction. A moving average filter was also used for longitudinal smoothing to eliminate reconstruction artifact as discussed in more detail below. The smoothed vascular points were saved as a 3-column text file, and the center line was also extracted.

The smoothed vascular points were loaded into SolidWorks (Waltham, MA). Briefly, the “Lofted Boss/Base” function in SolidWorks was used to generate models and their extracted centerline was loaded to trim the inlet as needed. The trimmed model was saved as ParaSolid document for use in CFD simulations.

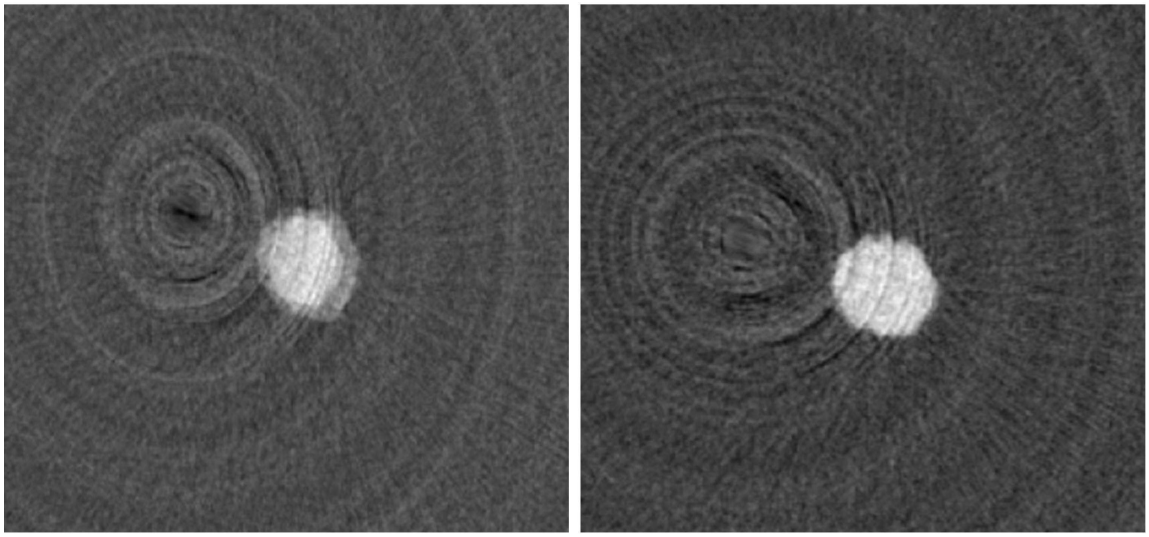

Figure 17. Images showing a cross-sectional slice from the reconstruction volume for the abdominal aorta of a representative rat from the current work. The left image shows an artificial second grey ring shadowing effect around the real reconstructed vessel caused by improper steps in the reconstruction process. The right image shows a correct reconstruction without this artifact. This was in the middle of the reconstruction process, and no scale was available. These images were only used for verifying the accuracy of reconstruction process.

4.2.4 Determination of Windkessel Parameters

Windkessel parameters (Rc, C, and Rp) were determined from measured data using the pulse pressure method [87], then applied for CFD modeling. Briefly, the Rt (which is mostly comprised of Rp) was estimated at Pmean/Qmean. The stiffness caused by AGEs induced collagen cross-linking was used as a surrogate for C, and Rc reflects the stented region that was not quantified since previous research in our lab showed that stenting has no impact on local resistance under resting conditions [134]. An Rc/Rt ratio of 5.6% was assumed initially in order to obtain an estimate of capacitance using the pulse pressure method. The Rc/Rt ratio was based on previous research [135] where the

characteristic resistance is less than 6% of total resistance in human rest conditions. The initial values of Rc, C and Rp were then optimized using an automated Matlab program to match the systolic and diastolic BP of the measured waveform.

4.2.5 CFD Simulations

Computational meshes were created using MeshSim (Simmetrix; Clifton Park, NY), which is integrated within the Simvascular open source software package (simtk.org) used for CFD modeling and simulation. BF data from each rat was ensemble averaged using >10 beats to generate a waveform that was imposed at the inlet mesh face as a Womersley velocity profile. It was assumed that the stented AAo was rigid [134], and blood was assumed to be Newtonian with a density of 1060 kg/m^3 and viscosity of 6.2 cP, consistent with previous research [76].

An in-house stabilized finite element solver with embedded commercial linear solver LESLIB (Altair Engineering, Troy, MI) was used to solve equations for conservation of mass and balance of fluid momentum. Briefly, the model was first discretized into a mesh containing ~500,000 isotropic elements. Mean BF and resistance were used to perform a steady simulation, and adjustment was made by changing vascular resistance to make sure the simulated BF and BP matched previous measurements obtained for the rat at harvest. After this first simulation, localized mesh refinement was applied using an adaptation method in Simvascular for the second simulation. In the second simulation, a mean simulation was performed to initialize the flow domain for a subsequent pulsatile simulation. Four to five successive pulsatile simulations were then conducted until meshes contained 2.5 to 3 million tetrahedral elements, again generated using an adaptive technique for localized refinement. More

specifically, the minimum element edge size was measured to ensure it was three times less than the minimal stent strut edge size [136], so that the calculated TAWSS from CFD simulation could be calculated from elements as close to the arterial wall as possible. TAWSS from three small areas in the proximal, middle, and distal stented region were quantified for each simulation to ensure TAWSS was independent of the element size. The simulated BF in the last cardiac cycle was also queried to ensure it was within 5% of measured mean flow value, and within 5 mmHg of the measured systolic, diastolic and pulsatile BP, consistent with similar previous research [137, 138].

4.2.6 Quantification of TAWSS

The accuracy of TAWSS largely depends on the confidence with which the near wall velocity gradient can be determined. In theory, CFD has the potential to offer much higher resolution than other image methods, but this depends on local features of the mesh as alluded to above.

TAWSS was calculated from the last cycle as described previously [139]. TAWSS was computed at each node on the CFD mesh surface as:

$$TAWSS = \left| \frac{1}{T} \int_0^T \overrightarrow{WSS}\, dt \right|$$

Where $\overrightarrow{WSS}$ is the WSS vector at each node, and T represent time period of one cardiac cycle.

The TAWSS in the proximal stented region is influenced by the transition from the upstream unstented region to the expanded stented region. Conversely, at the outlet of the stent, local flow patterns will also be influenced due to the exit of blood flow from the expanded stented region. Previous research has found that elevated TAWSS was most

pronounced in the inlet and outlet of the stented region corresponding to the greatest NH formation [5]. To avoid those flow influences, we calculated the regional TAWSS and intrastrut TAWSS in the middle of the stented region.

TAWSS (range from 0 – 30 dyn/cm^2) was visualized using Paraview software (Kitware Inc., Clifton Park, NY) after the CFD simulation for each rat was completed. A Matlab program was then used to extract TAWSS within six intrastrut positions as shown in **Figure 18** queried from the middle of the stented region for comparison to NH results obtained as part of Aim 2. Beyond contributions resulting from entrance or exit flow disturbances, the middle portion of the stent is also less susceptible to pronounced vessel injury than the proximal and distal ends experiencing compliance mismatch. TAWSS values were determined from nine neighboring points within each of these intrastrut regions, and collectively averaged to generate a representative TAWSS value from the center of the stented region for each group of rats to be compared with NH quantified as discussed below.

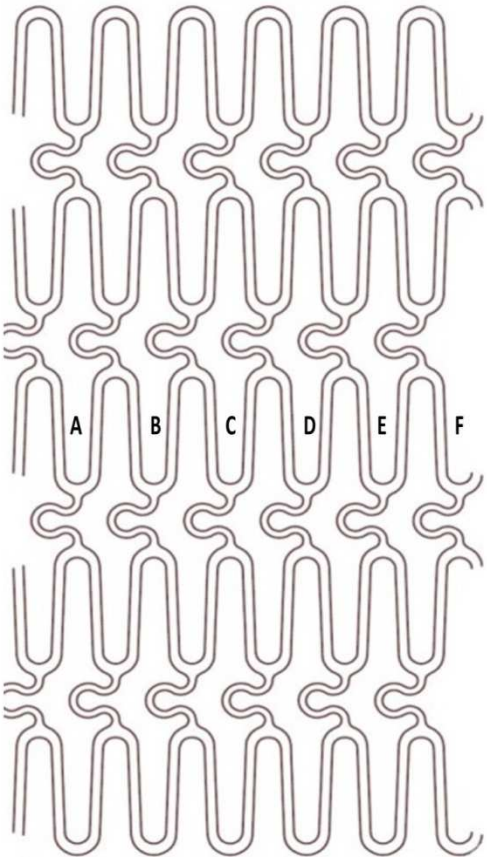

Figure 18. Diagram showing the locations for instrastrut TAWSS quantification after CFD simulations. A through F represent six locations in the middle of the stented region where 9 nearest neighbor values were averaged to quantify TAWSS for ZL, ZO and ZD stented rats.

4.2.7 Statistical Procedures for Data Analysis

At least 6 rats from each group were averaged to compare body weight, HR, blood glucose concentration, mean BF, mean BP and vascular resistance. Regional TAWSS was determined from 3 rats from each ZL, ZO and ZD group before ALT-711 treatment, as well as 3 rats from each group after ALT-711 treatment. Intrastrut TAWSS were compared from 9 nearest neighbor points in the 6 intrastent regions within the middle of the stent for 3 rats from each ZL, ZO and ZD group without ALT-711

treatment. Statistical analysis was conducted based on previously outlined in the common methods to all specific aims.

4.3 Results

4.3.1 Osmotic Pump Control

Implantation of osmotic minipumps loaded with saline alone did not affect body weight (449 ± 5 vs 406 ± 12 g, mean ± SEM), blood glucose (161 ± 38 vs 225 ± 19 mg/dL), or heart rate (HR; 244 ± 14 vs 278 ± 13 beats/min) as compared to stented ZL rats without osmotic minipump as shown in **Figure 19**. The use of osmotic minipumps for delivery of ALT-711 dissolved in saline was therefore deemed appropriate and used to obtain the following results.

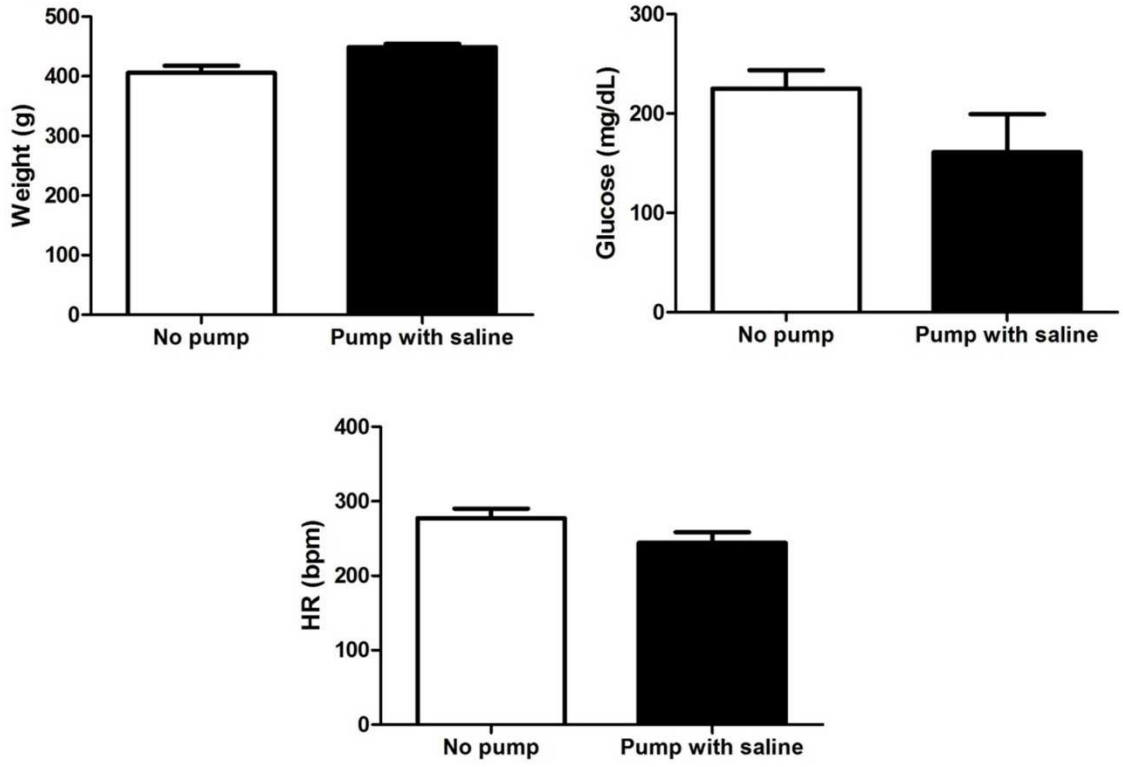

Figure 19. Body weight, blood glucose concentration and HR from stented ZL rats. White bars indicate stented ZL rats, and black bars indicate stented ZL rats implanted with osmotic minipumps containing saline (N = 4/group). No significance was found for these indices.

4.3.2 Body Weight, HR, Mean BP and Blood Glucose

Body weight and HR at the end of the procedure in all ZL, ZO and ZD rats were similar in the absence or presence of ALT-711 treatment as shown in **Figure 20**.

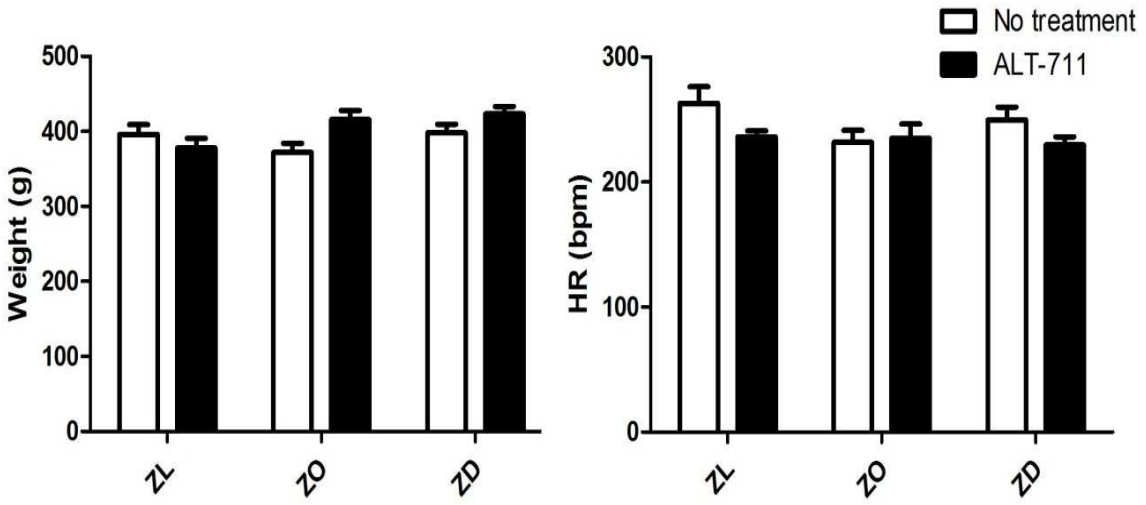

Figure 20. Body weight and heart rate of ZL, ZO and ZD stented rats. White bars represent rats without treatment, and black bar represent rats that received ALT-711 (N=6/group). Body weight and HR were not different for ZL, ZO and ZD rats in the absence or presence of ALT-711.

No significant differences were found for weight difference before the stenting procedure and at harvest for untreated and ALT-711 treated ZL, ZO and ZD rats (**Figure 21**). This result agreed with previous findings showing that body weight was similar for untreated and ALT-711 treated diabetic rats [140].

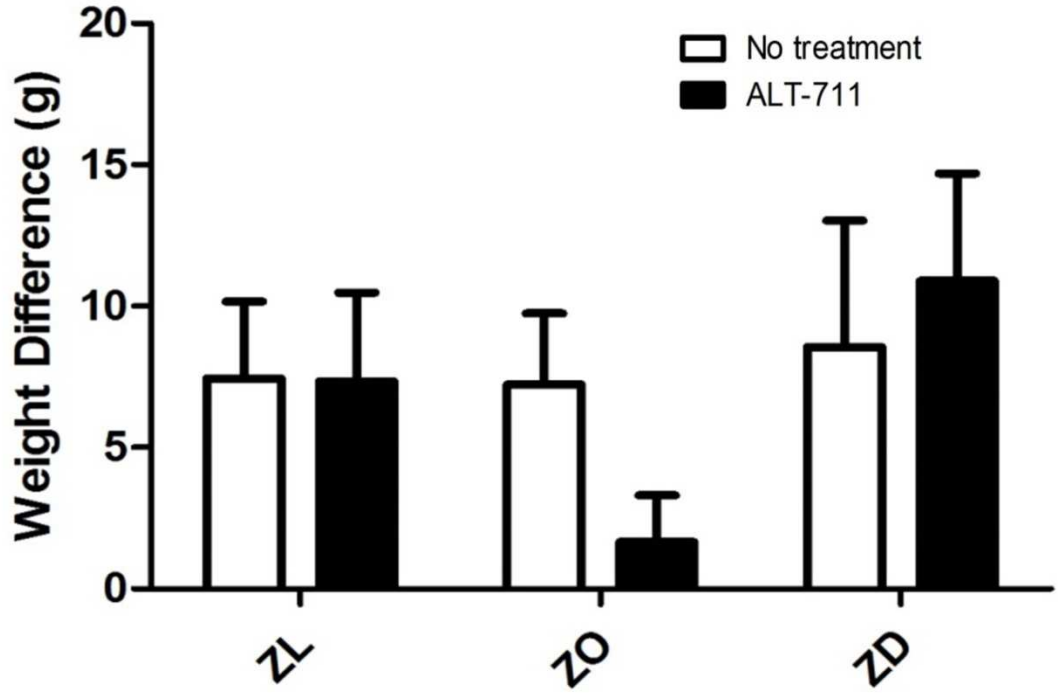

Figure 21. Weight difference before the stenting procedure and at harvest for untreated and ALT-711 treated ZL, ZO and ZD rats. No significant differences were observed.

Mean BP was similar in ZL (100 ± 3 vs 92 ± 5 mmHg), ZO (96 ± 4 vs 100 ± 6 mmHg) and ZD (97 ± 1 vs 94 ± 6 mmHg) rats in the absence or presence of ALT-711 (**Table 5)**. Blood glucose concentration was significantly elevated for ZO and ZD as compared to ZL rats (359 ± 19 and 428 ± 24 vs 232 ± 18 mg/dL, $P<0.05$). Although there was a trend toward decreased blood glucose concentration for all rats with ALT-711 treatment, this decrease did not reach significance and values remained elevated compared to ZL rats (ZO: 276 ± 25 and ZD: 342 ± 18 vs ZL: 171 ± 19 mg/dL, $P > 0.05$) (**Table 5**).

	Mean BP (mmHg)		Glucose (mg/dL)	
	- ALT-711	+ ALT-711	- ALT-711	+ ALT-711
ZL	100 ± 3	92 ± 5	232 ± 18	171 ± 19
ZO	96 ± 4	100 ± 6	359 ± 19*	276 ± 25*
ZD	97 ± 1	94 ± 6	428 ± 24*	342 ± 18*

*Table 5. Mean BP (mmHg) and blood glucose (mg/dL) in the absence (-) or presence (+) of ALT-711 (mean ± SEM) (N=6/group). Significance when P<0.05; * means significantly different from ZL stented rats.*

Mean BF measured from the inlet of the stented region was decreased in ZD as compared to ZL stented rats (6 ± 1 vs 10 ± 2 ml/min, **Figure 22**), but increased to ZL levels after ALT-711 treatment (6 ± 1 to 9 ± 1 ml/min). ALT-711 also increased BF in ZO rats (9 ± 2 from 7 ± 1 ml/min without treatment). ALT-711 treatment reduced distal vascular resistance calculated as mean BP divided by mean BF in ZD rats (16 ± 2 x 10^5 to 8 ± 1 x 10^5 dyn·s/cm^5, **Figure 22**).

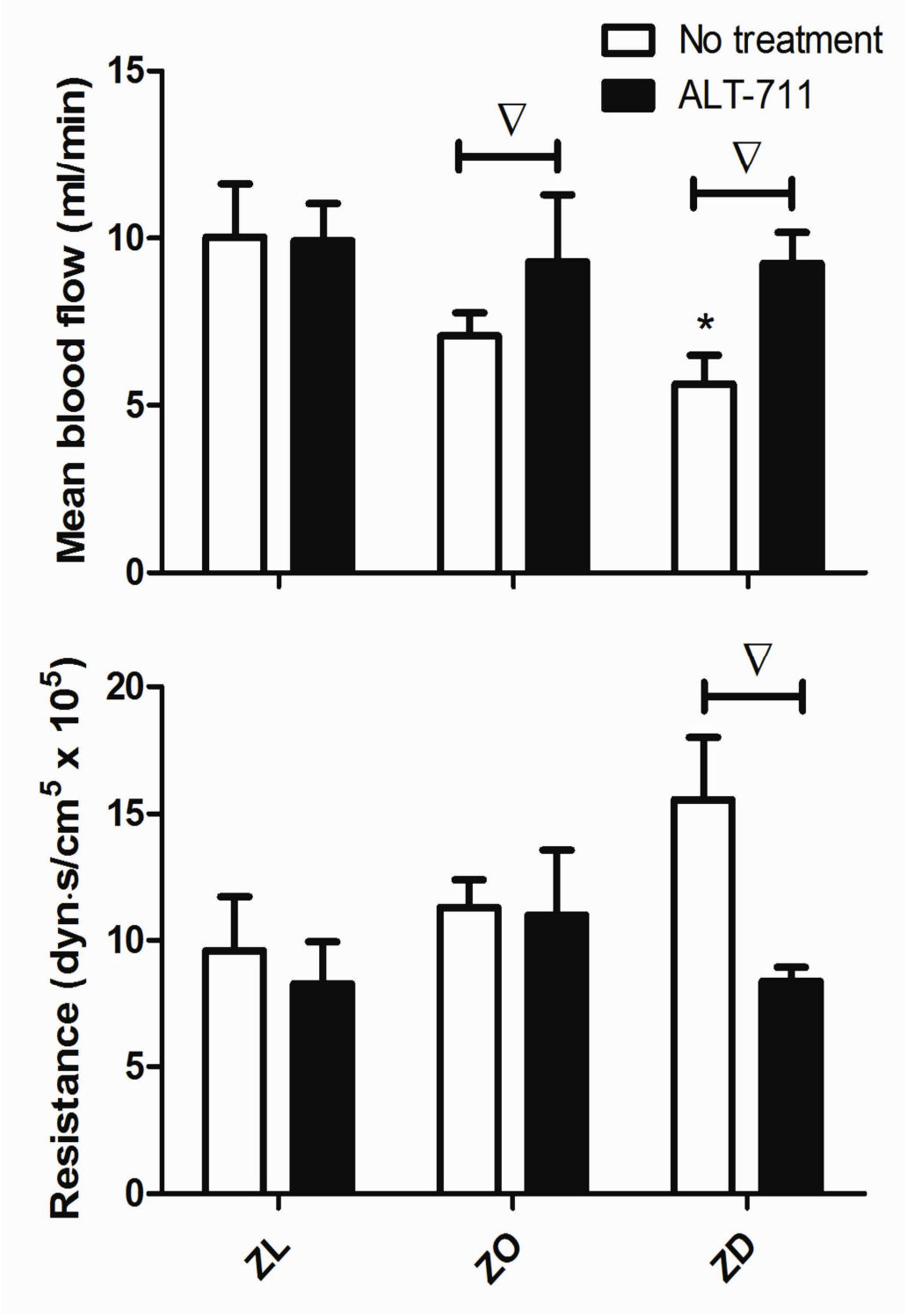

*Figure 22. Mean blood flow and resistance in ZL, ZO, and ZD stented rats in the absence or presence of ALT-711 treatment (N=6/group); * = significantly different from ZL, ∇ = significant difference within group.*

4.3.3 Reconstructed Vessels from SolidWorks

Representative solid models for untreated rats are shown in **Figure 23**. All models were created such that the stented region was located in the center of the model. The inlet and outlet lengths were therefore similar for all models to account for any potential flow disturbances occurring despite the use of a fully developed Womersley velocity profile.

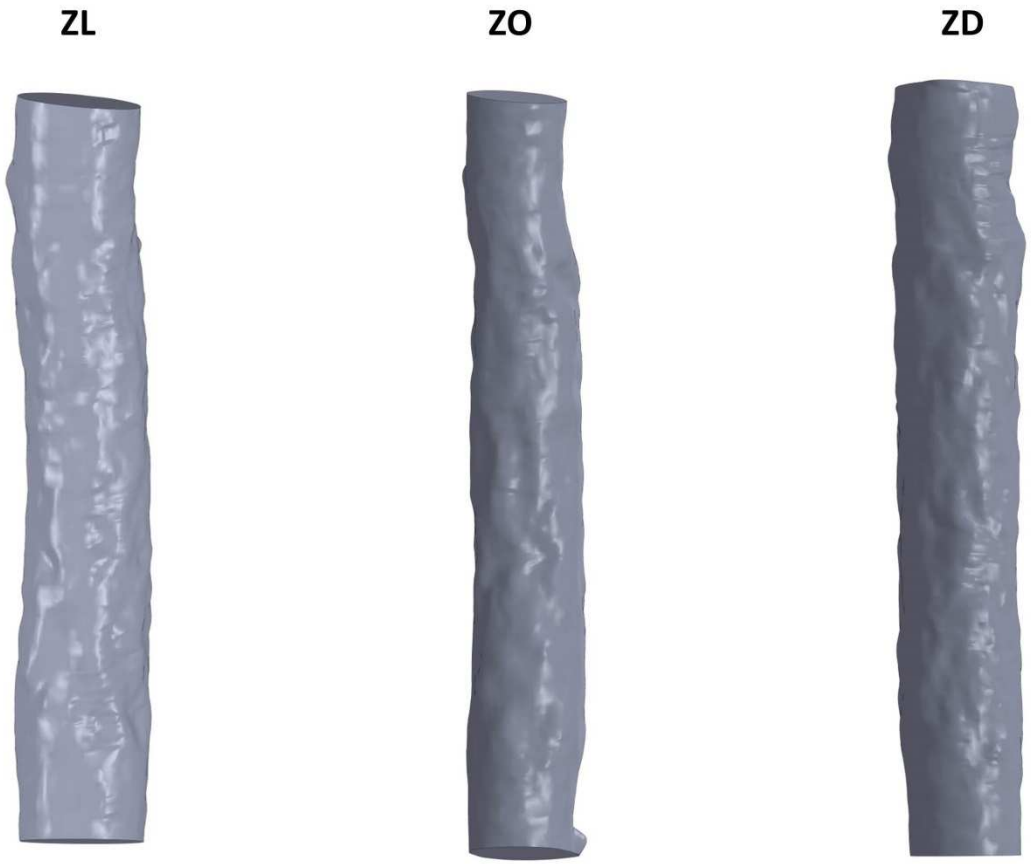

Figure 23. Renderings of the stented region from representative ZL, ZO and ZD rats as produced with SolidWorks after post-processing of reconstructed microfocal x-ray CT data.

4.3.4 Intrastrut TAWSS

Unwrapped TAWSS results are shown in **Figure 24** using a range of 0-30 dyn/cm^2. Quantification of corresponding distributions of TAWSS values from intrastrut regions in the middle of the stent were low for ZD (14.5 ± 1.9 dyn/cm^2) as compared to ZL and ZO rats (30.6 ± 1.6 and 25.4 ± 2.2 dyn/cm^2, respectively) (**Figure 25**). There were no regional differences in TAWSS for casts created in rats receiving ALT-711 treatment, and intrastrut TAWSS was therefore not calculated for these rats.

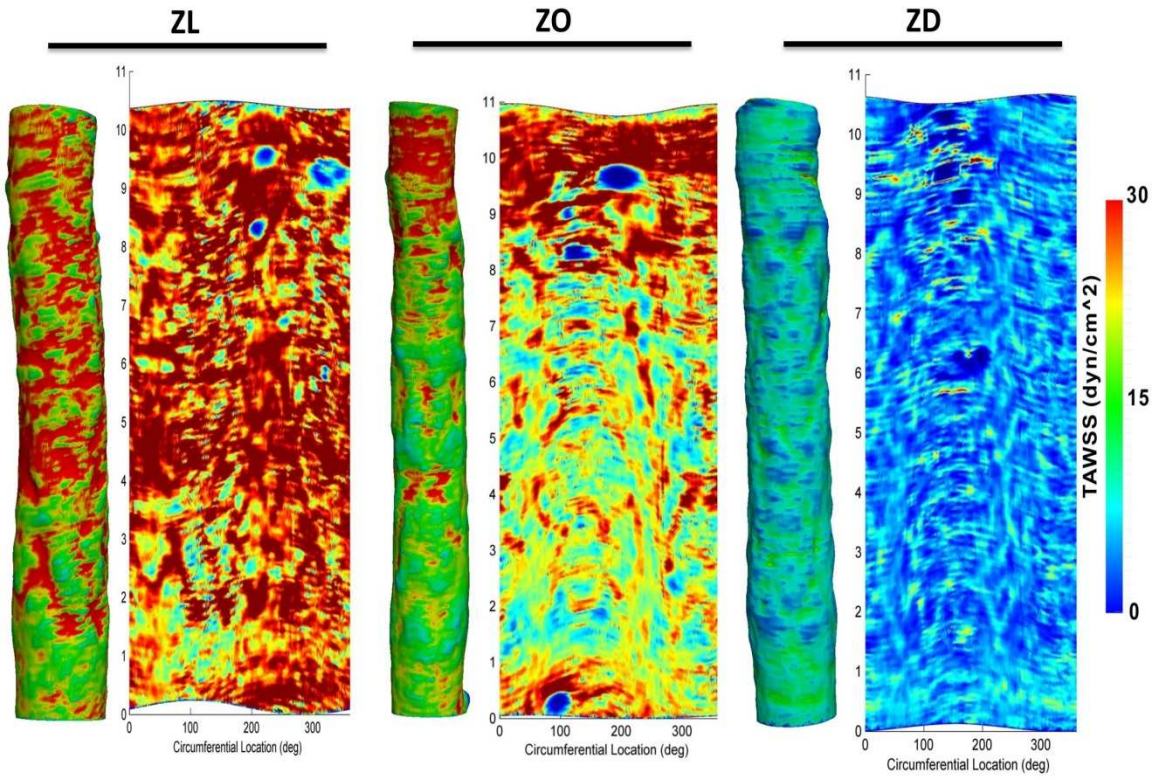

Figure 24. Representative TAWSS results in the ZL, ZO and ZD stented rats. Results from CFD are shown on the left and corresponding unwrapped versions appear to their right.

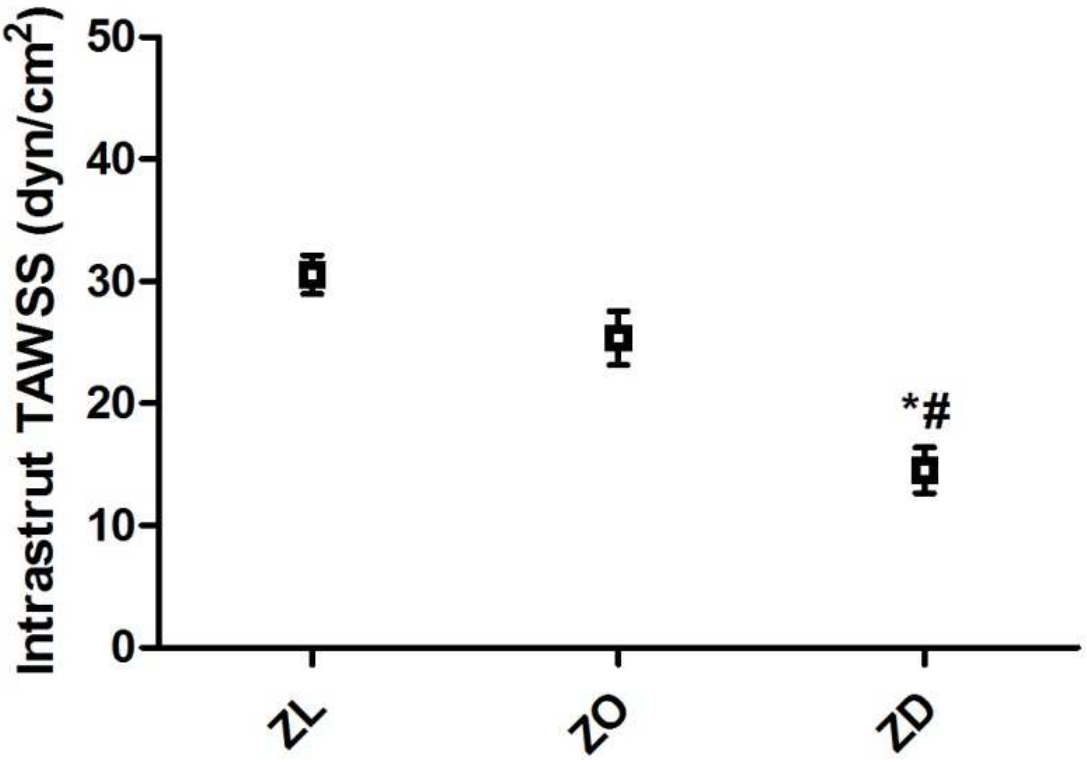

*Figure 25. Corresponding distributions of TAWSS from intrastrut regions within the middle of stents implanted into the abdominal aorta of ZL, ZO and ZD rats (N=6/group); * = significantly different from ZL, # = significantly different from ZO rats.*

4.3.5 Circumferential Smoothing Verification

The spatial distributions of TAWSS from CFD simulation results above have some persistent artifacts from the microfocal x-ray CT scanning and reconstruction process, particularly in the longitudinal direction. It is well known that some perceived pitting accompanies the high spatial resolution of this process [12]. While the postprocessing methods employed attempted to mitigate this potential issue, any persistent artifacts have the potential to influence TAWSS results. To further understand this potential influence, several different operations were evaluated for the longitudinal

smoothing implemented as part of the postprocessing operations discussed in section 4.2.3 (**Table 6**) [12, 118].

Filter name	**Function**
'moving'	Averaging
'lowess'	Local regression using weighted linear least squares and a 1st degree polynomial model
'loess'	Local regression using weighted linear least squares and a 2nd degree polynomial model
'sgolay'	local polynomial regression (of degree k), preserve maxima and minima
'rlowess'	A robust version of 'lowess' that assigns lower weight to outliers in the regression.
'rloess'	A robust version of 'loess' that assigns lower weight to outliers in the regression.

Table 6. Smoothing operations evaluated for longitudinal smoothing of reconstructed microfocal x-ray CT data.

Average filters were deemed most appropriate for their ability to smooth, as compared to create, perturbations and both 5 and 8 point moving average filters were investigated. Corresponding CFD simulation results along with distributions of TAWSS are shown in **Figure 26** below. Of note, both approaches reveal higher values of TAWSS with a pattern that corresponds to the specialized stent used for rats in the current investigation. This is to be expected since the stent protrudes into the flow domain, and suggests the microfocal x-ray CT image processing can capture geometric intricacies within the stented region. The 8 point moving average filter muted detailed information near stent struts, but TAWSS values from intrastrut regions were not different as shown

in **Figure 27**. Postprocessing operations using a 5 point moving average filter for longitudinal smoothing after the reconstruction process were therefore deemed reasonable.

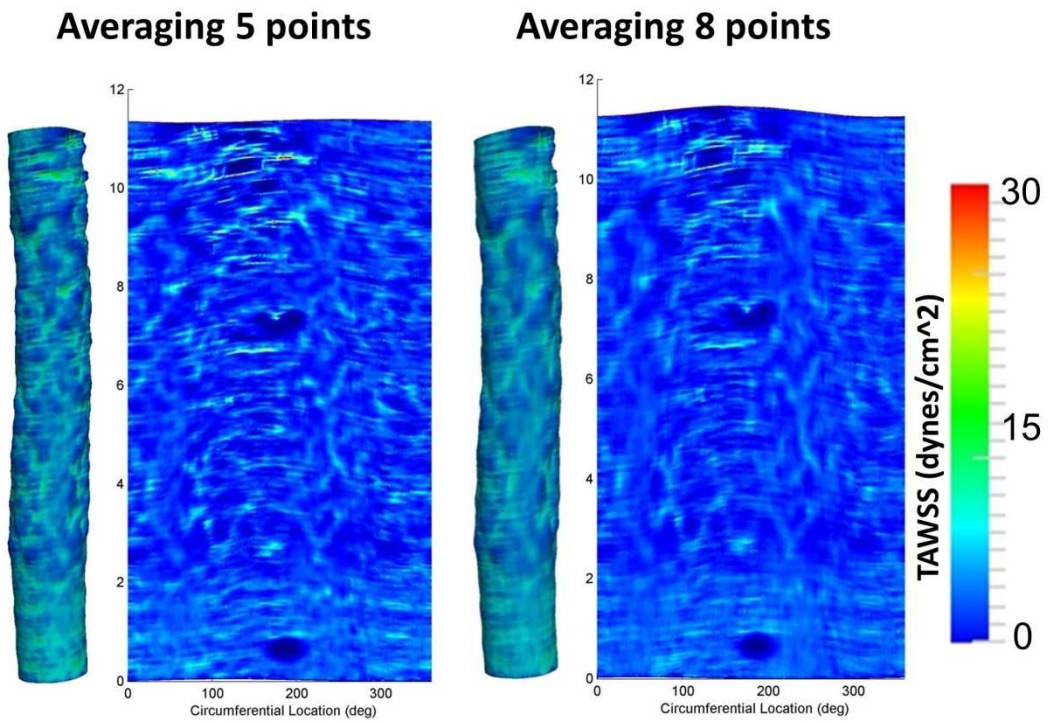

Figure 26. TAWSS CFD results obtained using a filter averaging 5 and 8 points longitudinally as part of the postprocessing operation applied following reconstruction of microfocal x-ray CT data.

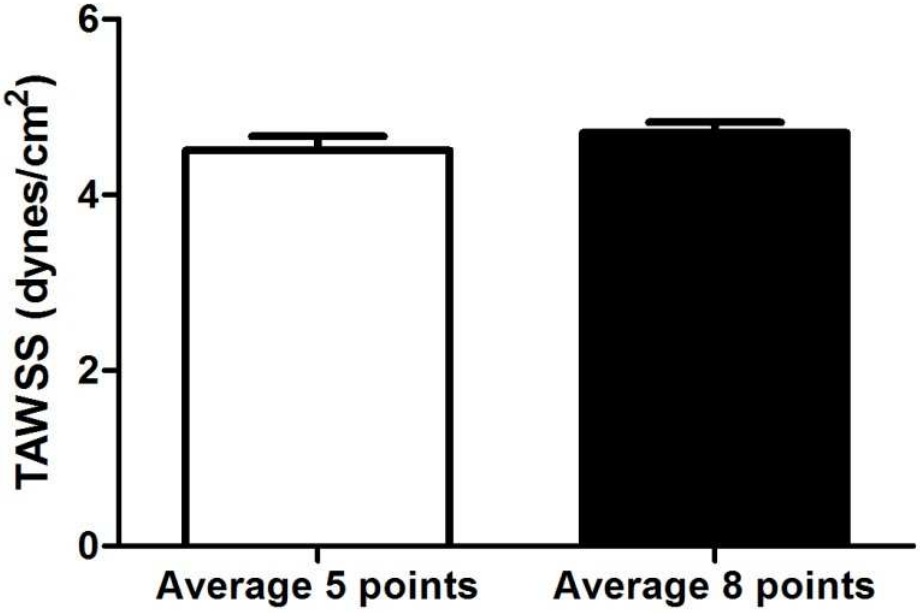

Figure 27. TAWSS values from intrastrut regions in the middle of the stent (N=6/group). No TAWSS difference were observed when results from 9 nearest neighbor elements within the center of six intrastrut regions were averaged for CFD models created from postprocessing operations using longitudinal smoothing operations consisting of a 5 or 8 point moving average filter.

4.4 Summary

The objective of this aim was to quantify the ability of AGE-mediated vascular changes to increase DVR thereby altering mechanical indices known to promote NH in T2DM, and determine whether these adverse changes can be alleviated by ALT-711. There were several important findings.

1) Mean BF decreased in ZD stented rats, concomitantly with a trend toward increases in DVR before treatment as compared to ZL rats. DVR was found to decrease in ZD stented rats after ALT-711 treatment as compared to untreated ZD rats. Mean BF in ZO and ZD stented rats were increased after ALT-711

treatment. Blood pressure was found to be similar before and after ALT-711 treatment which is consistent with previous findings [141] that ALT-711 could alleviate vascular dysfunction and wall stiffness without changing mean blood pressure.

2) Regional TAWSS in the middle of the stented region was quantified before and after ALT-711 treatment. Regional TAWSS within the stented region of untreated ZD rats was low relative to ZL rats in the absence or treatment, but was not different after ALT-711. This finding is likely due to observed reductions in BF, and hence lower velocity and TAWSS, within the stented region afforded by higher downstream resistance.
3) CFD simulations were conducted for untreated ZL, ZO and ZD stented rats. Results demonstrated TAWSS from intrastrut regions within the middle of the stent were reduced for ZD as compared to both ZL and ZO stented rats.

4.5 Potential Limitations

Rats were only stented for 21 days in this investigation. This time point was chosen based on previous literature. The process of restenosis as well as NH formation after stent implantation may be different between diabetic patients' arteries and diabetic rats' arteries. In animal models, previous studies have shown that NH caused by vascular intervention is mixed with extracellular matrix and migrating and proliferating SMC. In humans, NH is primarily mixed by collagen with extracellular matrix [142]. The development of NH after the BMS stenting process occurs faster in animal models, and reendothelialization of the stented region after implantation is usually complete between 21 to 56 days, but this procedure may not have even started after several months in

human [5, 143, 144]. We therefore chose to detect NH in rats after 21 days of stenting in this investigation.

This investigation used an osmotic minipump as a drug delivery system to give ALT-711. The ALT-711 chemical concentration was not monitored in the blood, and this might influence results in this investigation. However, the osmotic minipump has been used widely by other researchers, and it has been previously monitored for drug release to determine if it could be used as a substitute for IP injections [132]. This osmotic minipump was used according to manufacturer instructions and was allowed to equilibrate for one day before use. Success with the minipump in the current investigation may provide support and knowledge for its use in the future research.

The current approach assumes the arterial wall is rigid, but it deforms *in vivo*. This assumption was applied since the experimental approach of casting the stented flow domain and measuring its morphology using high resolution microfocal x-ray CT does not account for *in vivo* deformation. This assumption was deemed reasonable as a prior study showed stent implantation decreases the arterial compliance to zero within the stented region [145].

BP was measured using a fluid-filled catheter placed in the carotid artery, but the BF transducer was positioned just above the stented region for measurement of flow into the stented region. There is a distance between these two measurement locations so the relationship between BP, BF and resistance may not truly reflect reality as a portion of the blood flow distribution is lost to the liver and organs in the abdomen. The alternative approach of obtaining all measurements in the same position would require a fluid-filled needle positioned above the stented region for BP measurement, which is technically

challenging and would add to potential complications for the current experimental protocol. In addition, the stent was deployed below the renal vascular so as to not disturb blood flow to the kidneys. This may also influence BF and BP. Previous researchers have estimated the blood flow distribution for humans at rest as shown in **Table 7** [3] which may provide some reference for use in estimating rat flow distributions applicable to the measurement conditions mentioned above. Under this resting condition, about 43% of blood flow is delivered to liver, intestines, spleen and kidneys.

	Flow into various regions	
Upper body	mL/min	% total
Brain and heart	1000	
Muscle and skin (est.)	500	
	1500	26
Trunk: (4300 mL/min enters descending aorta, 74%)		
Liver, intestines and spleen	1400	
Kidneys	1100	
Muscle and skin (est.)	300	
	2800	48
Terminal aorta		
Pelvic organs and legs	1500	26

Table 7. Distribution of blood flow in humans at rest. (Adapted from Nichols et al, [3])

To preserve funding resources, CFD simulations were performed to quantify intrastrut TAWSS for a given treatment when significant differences in regional TAWSS were detected. However, the results showed differences between Table 4 (regional TAWSS quantification) and Figure 26 (intrastrut TAWSS quantification). Specifically, intrastrut TAWSS values were greater than values for regional TAWSS for corresponding untreated groups of rats. There are several potential reasons for these observations. First, the intrastrut TAWSS quantification used pulsatile flow data, whereas regional TAWSS was calculated from mean blood flow. Second, intrastrut TAWSS quantification was based on reconstructed flow domain data that includes local detailed differences in the radius of the vessel, as compared to caliper measurements for regional TAWSS. The advantage of the CFD approach is that it considers this detailed data reflecting the influence of stent struts on local geometry. However, post processing is performed on the data using a moving-average filter in the longitudinal direction after the image reconstruction step, and this step may modify local radius, which is raised to the third power in the calculation of TAWSS[5].

To detect whether the blood flow or radius contributed to the difference of TAWSS quantification mentioned above, the mean intrastrut TAWSS from mean, as compared to pulsatile, CFD simulation results were extracted from the same locations used to quantify time-averaged intrastrut TAWSS. All calculation conditions were the same as compared to the intrastrut TAWSS quantification from pulsatile simulations. There were no significant differences between intrastrut TAWSS from mean and pulsatile simulations (ZL: 30.6 ± 1.58 vs 34.3 ± 1.51, ZO: 25.4 ± 2.21 vs 24.3 ± 1.68, and ZD: 14.5 ± 1.88 vs 15.1 ± 1.96 dyn/cm^2). Collectively, the information above suggests that

differences in radius account for differences between the regional and intrastrut calculations. Generally speaking, intrastrut TAWSS results are preferred as they consider local stent-induced differences in radius. Importantly, TAWSS trends (ZL > ZO > ZD) were not different regardless of quantification method.

CHAPTER 5. SPECIFIC AIM 2: QUANTIFY AGEs RELATED COLLAGEN CROSS-LINKING AND PROTEIN EXPRESSION IN MULTIPLE ARTERIAL LOCATIONS TO ELUCIDATE MOLECULAR CHANGES CONTRIBUTING TO NH AFTER STENTING FOR T2DM, AND DETERMINE WHETHER THESE ADVERSE CHANGES CAN BE ALLEVIATED BY ALT-711.

5.1 Review of Rationale Applicable to Aim 2

AGEs induced stiffening of central, peripheral and distal vasculature is accentuated by hyperglycemia and could cause an increase in stent-induced vascular damage and changes in the distal vasculature that increase the resistance to BF. Inhibition of AGEs related collagen cross-linking by ALT-711 restores arterial compliance and decreases DVR. The upregulation of RAGE with AGEs has been noted previously, and this interaction also augments the inflammatory response to vascular injury in macrophages, endothelial cells and SMC [6]. TGFβ may be involved in cell proliferation, differentiation, and apoptosis during the stenting process [95]. However, no studies to date have directly examined the interaction between AGEs, hemodynamic indices, protein expression and NH after stenting in T2DM.

The objective of this specific aim was to quantify AGEs related collagen cross-linking and protein expression in multiple arterial locations to elucidate molecular changes contributing to NH after stenting for T2DM, and determine whether these adverse changes can be alleviated by ALT-711. Specifically, NH was quantified in the center of the stented region. AGEs related collagen cross-linking and protein expression were quantified in the carotid arteries, TA, AAo, IF as well as arterioles in cremaster muscle in stented T2DM rats.

5.2 Methods Unique to the Current Aim

5.2.1 Harvest of Arteries

After BP and BF measurement 21 days post stenting, rats were euthanized by an overdose injection of pentobarbital sodium (100 mg/kg). The stented region was carefully removed from the connective tissue and surrounding vessels. Any blood within the stented region was removed before being rinsed with saline, and fixed in 4% paraformaldehyde for >24 hours.

Vessels from carotid arteries, TA, AAo and, IF, and arterioles from cremaster muscle were obtained. The connective tissue and blood were rinsed with 4ºC saline. To avoid protein degradation, these sections were immediately snap frozen in liquid nitrogen and stored in a -80ºC freezer.

5.2.2 Isolation of Cremaster Arterioles

Arterioles are the primary site of resistance in the cardiovascular system. Mesenteric artery and cremaster arterioles have been studied previously [146, 147]. Cremaster muscle arterioles are commonly used to visualize the microcirculation in mice [148]. Advantages to using the cremaster muscle is that the tissue is thin enough to visualize and easy to harvest. Additionally, mesentery arterioles may have a significant amount of fat, especially in larger ZO and ZD rats. Perhaps the most important reasons supporting the use of arterioles from cremaster rather than mesentaric tissue is that the current investigation focuses on detecting the impact of downstream vascular changes on the upstream stented region. The stent was deployed in the abdominal aorta, and the top of the stent was below the mesentery bifurcation. Hence, cremaster arterioles were

deemed more suitable for this investigation.

Cremaster arterioles were isolated according to previous methods (**Figure 28**) [149, 150]. Briefly, the fur around the lower portion of the abdomen was cleaned after euthanasia as described above. An incision was made through the skin, and the cremaster muscle was dissected from the surrounding connective tissue. After isolation, all the muscular tissue was carefully removed from the arterioles to yield about 1.5 cm in length. To avoid protein degradation, arterioles were immediately snap frozen in liquid nitrogen and stored in a -80ºC freezer.

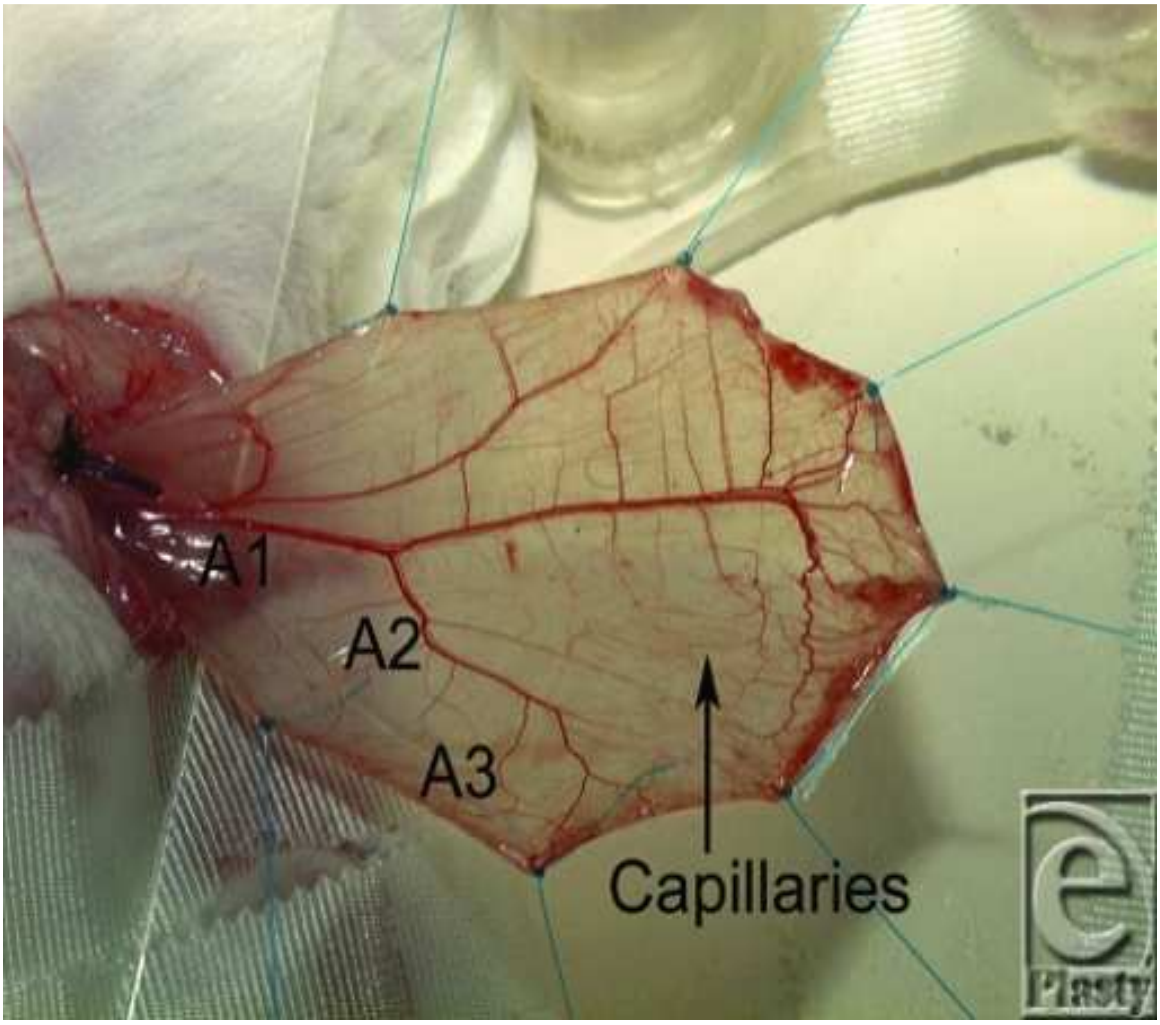

Figure 28. Arterioles from a rat cremaster muscle. A1 is the main cremaster feeding vessel, A2 is the arterioles branch, and A3 is the branch off the A2-arterioles. (Adapted from http://openi.nlm.nih.gov*). A scale is not available for this open source image.*

5.2.3 Stented Vessel Embedding

The stented AAo of rats not undergoing casting was carefully removed from connective tissue and surrounding vessels. The AAo was then rinsed with saline to remove any blood and fixed in 4% paraformaldehyde for >24 hours. Vessels were then dehydrated in 70% ethanol for 2 hours, 95% ethanol for 2 hours, and 100% ethanol twice for 2 hours. Following dehydration, samples underwent pre-infiltration for 2 hours, and

infiltration for 24 hours before being embedded in glycol methyl methacrylate (GMM; Technovit 7100; EB Sciences, Agawam, MA) (**Figure 29 left**) and sectioned at room temperature in 5 micron intervals using a Sorvall MT2 retracting microtome equipped with a tungsten carbide blade that permitted sectioning through the stent (Ted Pella; Redding, CA) (**Figure 29 right**).

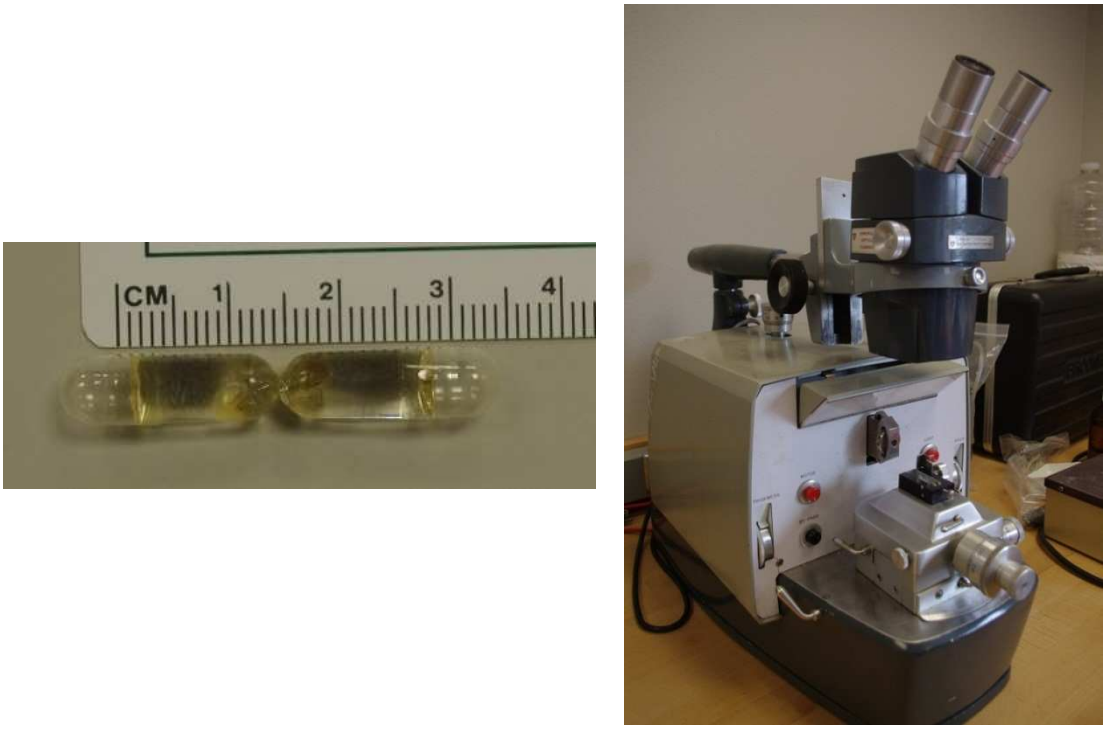

Figure 29. Stented arteries were embedded in glycol methyl methacrylate (left), and a Sorvall MT2 retracting microtome with tungsten carbide blade shown on the right was used for sectioning.

5.2.4 Hematoxylin and Eosin Staining and Image Acquisition

H&E staining was used to identify nuclei, cytoplasmic structures and extracellular components. Briefly, GMM stent sections were stained by Gill's Hematoxylin for 15 minutes followed by three distilled water washes. Scott's tap water was used for 2 minutes followed by an additional three washes with distilled water. Sections were then

counterstained with Eosin for 5 minutes, dehydrated carefully using 96% and 100% ethanol, and cleared in xylene. A xylene based mounting medium was used with glass cover slips to cover sections without bubbles. Histological sections with 12 stent struts at regular circumferential intervals were selected for image quantification as discussed below in order to reduce quantification differences that can manifest from longitudinal changes in scaffolding due to the stent geometry.

Images were obtained using an Olympus IX70 microscope at 4X Zeiss Universal objective lens with a 16-bit Leica DFC 280 camera controlled through PCI board via IPLab for Windows. All images were white balanced and focused to clearly identify the NH boundary. A 2.5X Zeiss Universal objective lens could obtain an image of the entire vessel section, but with low power resolution and less detail. A 4x lens was therefore used to obtain four quadrants of each vessel section thereby yielding higher resolution images. Images contained a slight overlap of sections beyond each quadrant, and specific structures unique to each section were used as markers to recreate a high resolution montage image of each section in Photoshop. In addition, a scale bar obtained at 4x was included on the image montage for later use in calibration.

5.2.5 NH Quantification

NH was quantified from the middle of the stented region to avoid contributions resulting from entrance or exit flow disturbances, or pronounced vessel injury, and for comparison to indices of TAWSS from spatially equivalent regions discussed in Aim 1. To account for potential differences in aortic caliber between rats and offer an accurate representation of NH formation, the percentage of the vascular lumen in which NH occurred was quantified by subtracting the luminal area from that bounded by the stent

with ImageJ software [5]. Random numbers were assigned to section images before quantification to avoid personal influences. Briefly, the vessel image was calibrated using the scale bar (**Figure 30 A**), and converted into 8-bit grayscale image for thresholding as shown in **Figure 30 B**. The freehand tool in ImageJ was used to carefully delineate the lumen area bounded by stent struts and the measure function in ImageJ was used to determine area. Stent struts were then digitally removed as shown in **Figure 30 C**, and the threshold function was applied to encompass the full NH section by adjusting the lower and upper threshold levels (**Figure 30 D**). Any blood particles within the vessel were digitally removed to prevent their influence on the NH quantification process. Finally, the analyze particles (i.e. measure) function in ImageJ was again used to calculate the area of the selected NH region and express it as a function of vascular lumen delineated by stent struts. Intrastrut NH thickness was also quantified as a function of luminal radius to provide confirmation of trends obtained with NH area quantification.

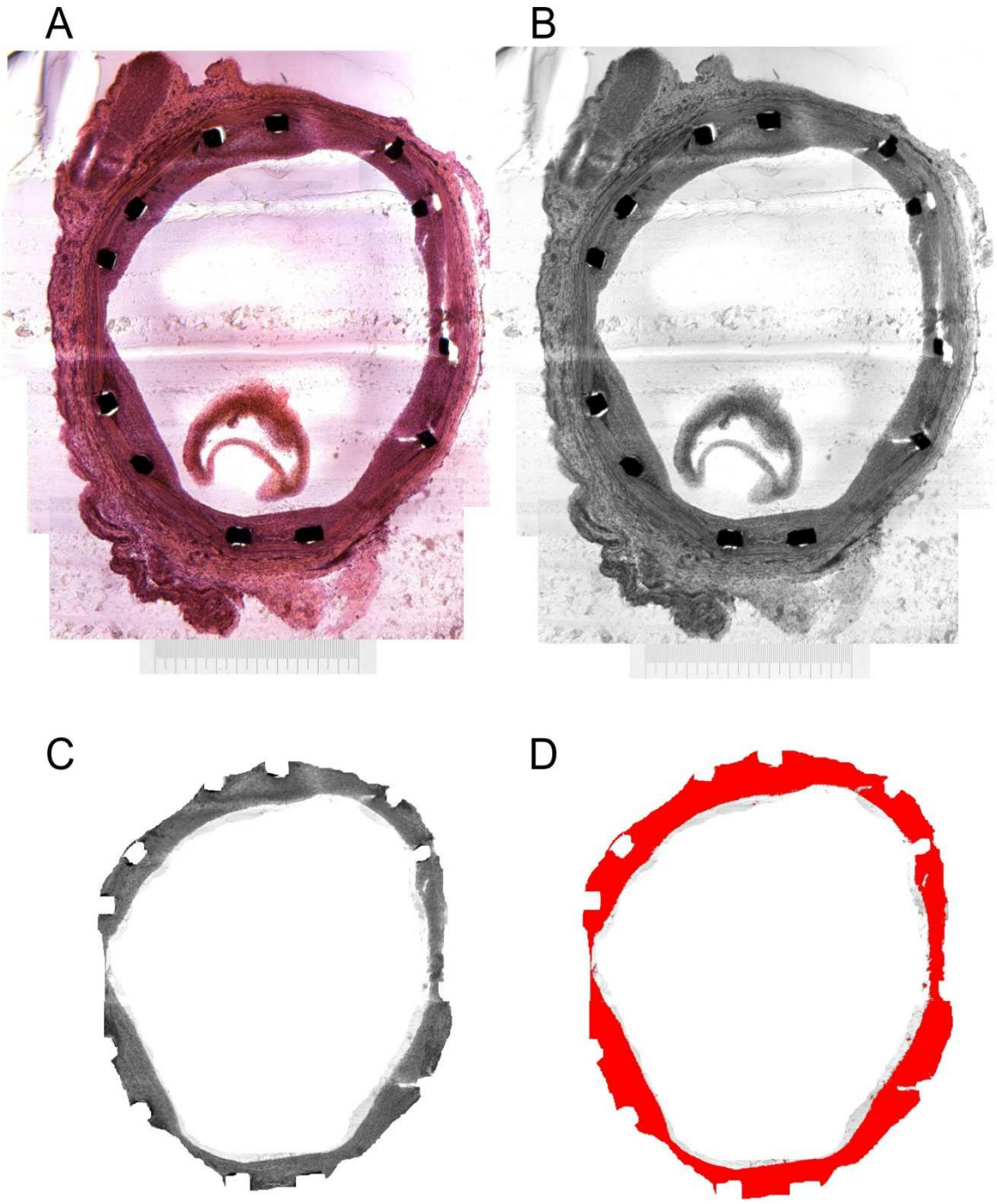

Figure 30. Example of NH quantification methods applied using a representative untreated ZL rat. A shows a montage of a stented vascular section (4X) with a calibration scale on the bottom. B shows the image loaded into ImageJ and converted into an 8-bit grayscale image. C shows an image of NH after digital removal of the vessel outside that bounded by stents struts, blood particles within the vessel region, and stent struts were removed using ImageJ, and D shows thresholding of NH to obtain the area for quantification.

Mean injury scores after stenting were also calculated as previously described [4]. This method allows for the quantification of the severity of the injury imposed on arteries as a result of the stenting process. Briefly, scores were assigned for each strut within the section for each rat as shown in **Table 8**. A mean score was then determined for each stent. These stent injury values where then averaged for each group in the absence and presence of treatment [4].

Score	Description of vascular injury
0	Internal elastic lamina intact; endothelium denuded; media compressed, not lacerated
1	Internal elastic lamina lacerated; media compressed, not lacerated
2	Internal elastic lamina lacerated, media visibly lacerated, external elastic lamina intact but compressed
3	External elastic lamina lacerated; large lacerations of media extending through external elastic lamina; coil wires sometimes residing in adventitia

Table 8. Scoring rubric for assessing stent-induced vessel injury score. (Adapted from Schwartz et al. [4])

5.2.6 AGEs Related Collagen Cross-linking Analysis

Vessel segments analyzed for AGEs related collagen cross-linking underwent pepsin digestion as described previously [151]. Briefly, vessel segments were lyophilized for >8 hours to obtain their dry weight. 10 mg dry samples were then treated with 4M guanidine-HCL in 0.05 M sodium acetate (pH 5.8) at 4^0C for 24 hours to remove proteoglycans. After centrifugation for 30 minutes at 30,000g, the residue was collected

and washed three times using 0.5 M acetic acid. The collagen residue was added to a solution of 1mg/ml pepsin in 0.5M acetic acid at 4^0C for 3 days, and undigested material was discarded by centrifugation for 20 minutes. AGEs related fluorescence of the supernatant was measured by 365nm excitation and 418nm emission before being reacted with Sirius red in 0.5 M acetic acid and incubated at room temperature for 20 minutes. After incubation, samples were centrifuged at 2,500g for 10 minutes and the absorbance of the supernatant was read at 540 nm against a 0.5 M acetic acid blank. A series dilution of collagen I (Life Technologies Corp.; Grand Island, NY) was then used to generate a standard concentration and absorbance curve. Previous studies found a linear relationship between Sirius red and optical density, and that a 0.5 µM concentration of Sirius red was suitable for collagen quantification without saturation [152]. The result was presented as AGEs related fluorescence divided by collagen concentration.

5.2.7 Protein Isolation from Arteries

Protein for Western blotting analysis was isolated as previous described [153]. Briefly, a 2 ml microcentrifuge tube containing a stainless steel bead (5 mm diameter) was placed on dry ice for >15 minutes. The adapter of a simultaneous tissue disrupter/homogenizer (TissueLyser LT; QIAGEN, Valencia, CA) was kept at room temperature, and up to 30 mg of frozen tissue was transferred to the pre-cooled tube and incubated for another 15 min. The tubes were then incubated at room temperature within the adapter for 2 minutes to avoid freezing of lysis buffer. Appropriate volume of lysis buffer was immediately added to each tube and placed the insert with sample tubes into the base of the TissueLyser LT disrupter/homogenizer. The lid of the TissueLyser LT disrupter/homogenizer was placed over the insert, securely fastened, and operated for

10min at 50 Hz.

5.2.8 Western Blot Analysis

The protein sample was then centrifuged three times for 20 minutes to remove DNA, RNA and cellular debris. The amount of protein was quantified using a spectrophotometer (Beckman Coulter; Brea, CA) with the Bradford method using bovine serum albumin (BSA) as a standard [154]. Protein concentration was measured with an UV-VIS spectrophotometer at 595nm. The purified protein was snap frozen immediately and stored at -80°C.

Western blotting procedures were similar to those described elsewhere [153]. Briefly, the quantified vessel protein samples were taken out from the -80°C freezer, and stabilized on ice for 30min. The maximal loading volume was 30 μL for the precast gel used in this investigation, and the loading protein amount was the same for all samples without exceeding 30 μL. The same amount of protein (30 μg in this investigation) from all groups was added to the of Laemmli buffer, and incubated in a Thermomixer for 5 min at 97˚C. The treated protein mix was then loaded to run a 4–20% polyacrylamide gel (Criterion; Bio-Rad, Hercules, CA). The gel was placed in the loading box, and run for 10 min at 100v and then 50 min at 150v for gel electrophoresis. After that, the gel was carefully handled and soaked in transfer buffer for 5 min. The membranes, sponges and papers were soaked in transfer buffer for 5 min as well, and placed in layers inside a cassette. The gel transfer occurred at 100v for one hour in a cold room on a rotator. Following transfer, the membrane was soaked in Tris-Buffered Saline and Tween 20 (TBS-T) (50 mM Tris, 150 mM NaCl, 0.05% Tween 20, pH 7.6) on a shaker for 5 min. The membrane was then incubated on shaker (2 rpm) for 1h at room temperature with 10%

blocking milk using TBS-T to block the membrane, and the membrane was then washed 5x at 5 minutes rinse intervals with TBS-T (~10-20 mL per membrane per rinse). After washing, the primary antibodies (**Table 9**) used for Western blot were added to the appropriate membrane, and incubated on a shaker (2rpm) overnight at 4°C.

Antibody	Company	Catalog	Host	Primary Ab	Secondary Ab
AGEs	Abcam	ab23722	rabbit	1:500	1:2000
RAGE	Santa Cruz	sc-8230	goat	1:300	1:2000
TGFβ	Santa Cruz	sc-146	rabbit	1:400	1:2000
Beta tubulin	Abcam	ab6046	rabbit	1:5000	1:10000

Table 9. Primary and secondary antibodies used for Western blot. Beta tubulin was used as control.

Following treatment with the primary antibodies, the membrane was washed 5x using 5 minute rinse intervals with TBS-T and incubated with secondary antibodies (based on primary antibodies anti-rabbit or anti-goat) in solution on a shaker (2 rpm) for 1 hour at room temperature. The membrane was washed 5x using 5 minutes rinse intervals with TBS-T, and incubated in enhanced chemiluminescence solution (Thermo Fisher Scientific, Rockford, IL) for 5 min to yield signal. Forceps were used to remove the membrane from solution and one side was gently blotted with a KimWipe within a tray. The membrane was then transferred into a plastic developing sheet for processing in a molecular imaging system (Bio-Rad, Hercules, CA, USA).

5.2.9 Housekeeping Gene

The housekeeping gene is a constitutive gene that is necessary for maintenance of basic cellular function. The protein expression level from a housekeeping gene can be used as a control protein level to detect the expression patterns between control and experimental groups. The Western blot results typically present target protein expressions normalized against the housekeeping gene. There are many housekeeping genes, such as glyceraldehyde-3-phosphate dehydrogenase (GAPDH), beta-actin, or beta tubulin [155]. Previous researchers have found that the GAPDH activates pathways in diabetic condition and may influenced AGEs regulation [156] so that in this research we used beta tubulin as control protein.

5.2.10 Statistical Procedures for Data Analysis

Stented regions from 6 rats of each group were averaged to compare the NH area as well as intrastrut NH thickness. Arterial locations such as carotid artery, thoracic aorta, AAo, IF and arterioles from cremaster muscle of 6 rats in each group were averaged to compare the AGEs related collagen cross-linking as well as protein expression such as AGEs, RAGE, and TGFβ. All protein was quantified with the Bradford Method using BSA as a standard, and the same amount of protein was loaded to have a comparable results. Protein beta tubulin was analyzed at the same time, and the result was used as a basic expression level of all proteins. Results from other proteins were divided by the result from beta tubulin to express as fold changes without units. Statistical analysis was then conducted using multiple ANOVA followed by Tukey-Kramer multiple comparison test as listed in Aim 1.

5.3 Results

5.3.1 Osmotic Pump Control

Stented regions were quantified for percentage of NH area and intrastrut NH thickness in stented ZL rats with saline alone as compared to stented ZL rats without osmotic minipump (**Figure 31**). No significant differences were found for either NH index.

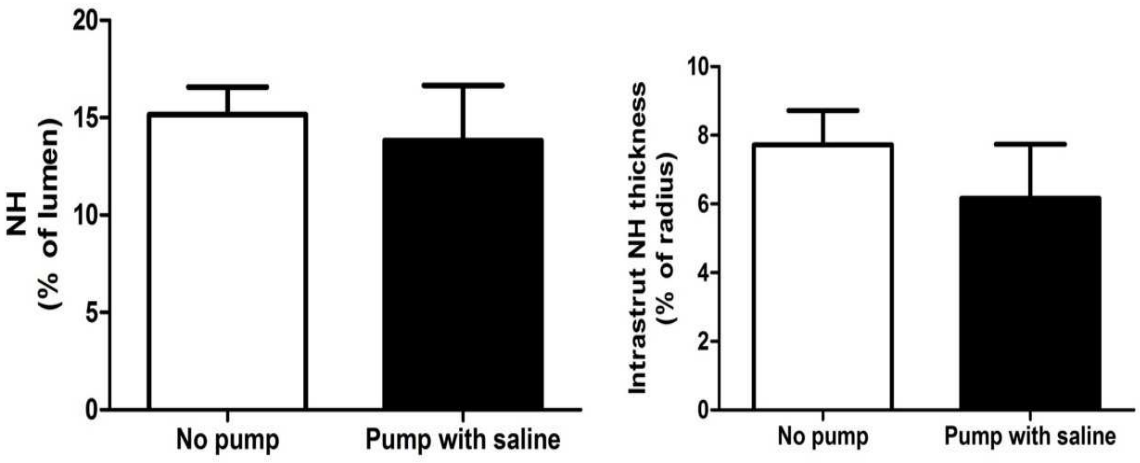

Figure 31. NH quantification for ZL stented rats without osmotic minipump (white bars) and ZL stented rats with osmotic minipump containing saline alone (black bar) (N=4/group); No significance was found for either index of NH.

Implantation of osmotic minipumps loaded with saline alone did not affect AGEs related collagen cross-linking within each vascular segment as compared respective values for in ZL rats without osmotic minipumps (**Figure 32 A**).

Protein expression of AGEs, RAGE, and TGFβ were also quantified in ZL rats with or without osmotic minipumps containing saline alone in the vascular segments mentioned above (carotid arteries, TA, AAo, IF, and arterioles; **Figure 32 B, C and D**).

AGEs, RAGE, and TGFβ protein expression did not affect by the implantation of osmotic minipumps loaded with saline alone as compared to respective values for in ZL rats without osmotic minipumps.

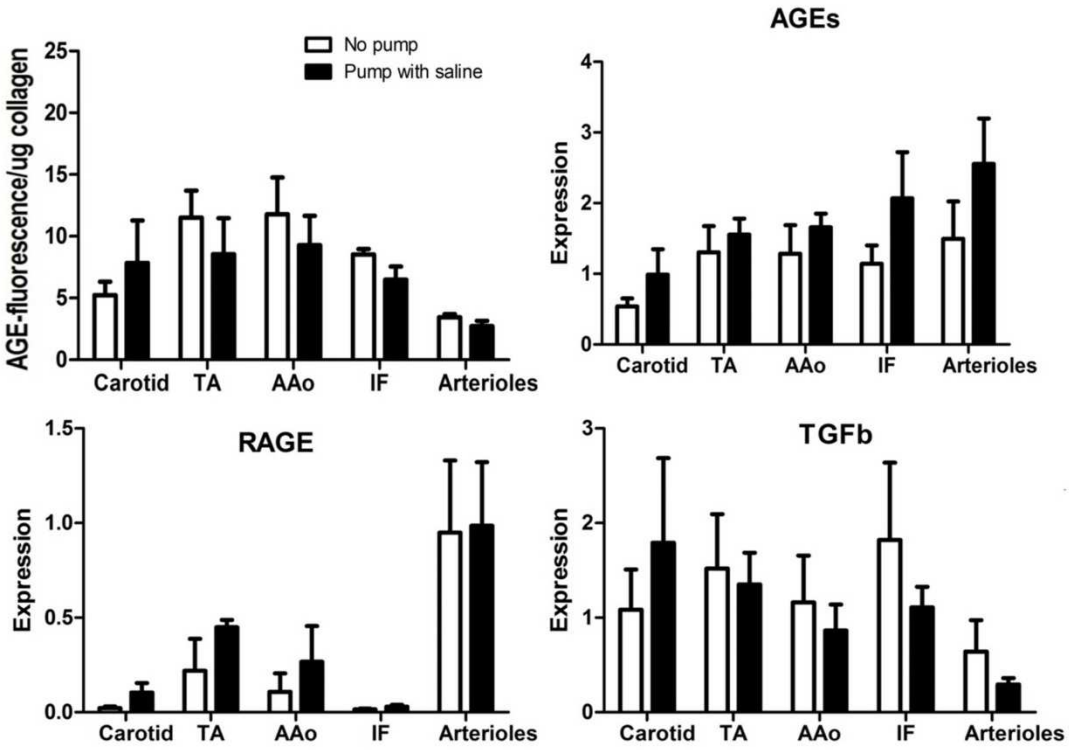

Figure 32. AGEs related collagen cross-linking (A) and protein expression (fold-change over beta tubulin) for (B) AGEs, (C) RAGE and (D) TGFβ in ZL stented rats without osmotic minipump (white bar) and ZL stented rats with osmotic minipump loaded saline along (black bar). There were no significant differences between groups of ZL stented rats receiving minipumps loaded with saline alone as compared to untreated ZL stented rats.

5.3.2 AGEs Related Collagen Cross-linking

AGEs related collagen cross-linking results from the vessels studied are shown in **Figure 33-34** and summarized in **Table 10**. No changes were found in AGEs related collagen cross-linking in the carotid arteries, TA and AAo without and with ALT-711 treatment (**Figure 33**). In addition, no significant differences were found within groups

without or with ALT-711 treatment. However, AGEs related collagen cross-linking was significantly increased in the IF of ZO and ZD rats without ALT-711 treatment (**Figure 34**). No significant differences were found in the IF after ALT-711 treatment.

Increases in AGEs related collagen cross-linking were also present in the arterioles of ZD stented rats as compared to ZL and ZO stented rats ($P<0.05$). However, decreases in AGEs related collagen cross-linking were found in arterioles of ZD stented rats as compared to ZL and ZO stented rats ($P<0.05$) (**Figure 34**). There was also a reduction in AGEs related collagen cross-linking in the arterioles of ZL and ZO rats that received ALT-711 treatment ($P<0.05$).

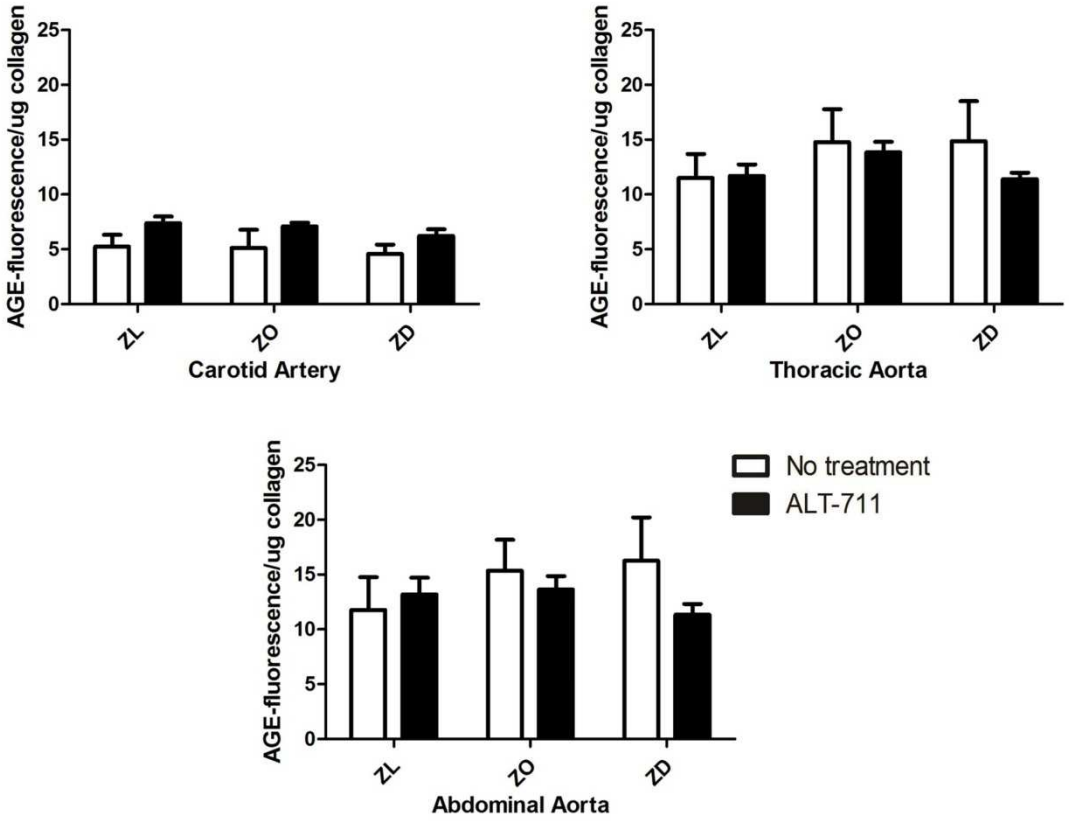

Figure 33. AGEs related collagen cross-linking in carotid artery, TA and AAo (N=6/group). No significant differences were found.

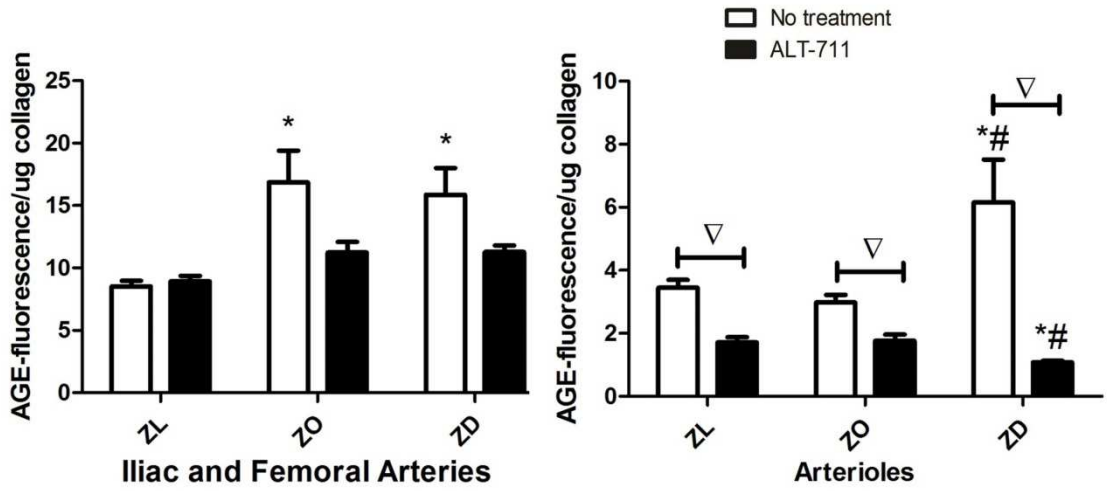

*Figure 34. AGEs related collagen cross-linking in iliac and femoral arteries and arterioles (N=6/group); * = significantly different from ZL stented rats, # = significantly different from ZO stented rats, ∇ = significant difference within group.*

5.3.3 NH Quantification

Representative histological sections from the middle of the stented region in ZL, ZO and ZD stented rats are shown in **Figure 35-41**. Quantification (**Figure 42**) showed elevated NH area (percentage of lumen) and intrastrut NH thickness (percentage of radius) for ZO rats (22 ± 1.3% vs 15 ± 1.4% of the lumen area) compared to ZL rats. ALT-711 treatment reduced NH area (percentage of lumen) in ZL and ZO rats. A decrease in intrastrut NH thickness (percentage of radius) was found in all groups with ALT-711 treatment (ZL: 7.7 ± 1.0 to 4.3 ± 0.9%; ZO: 12 ± 1.5 to 4.9 ± 0.8%; ZD: 9.4 ± 0.7 to 3.7 ± 0.4%, $P<0.05$).

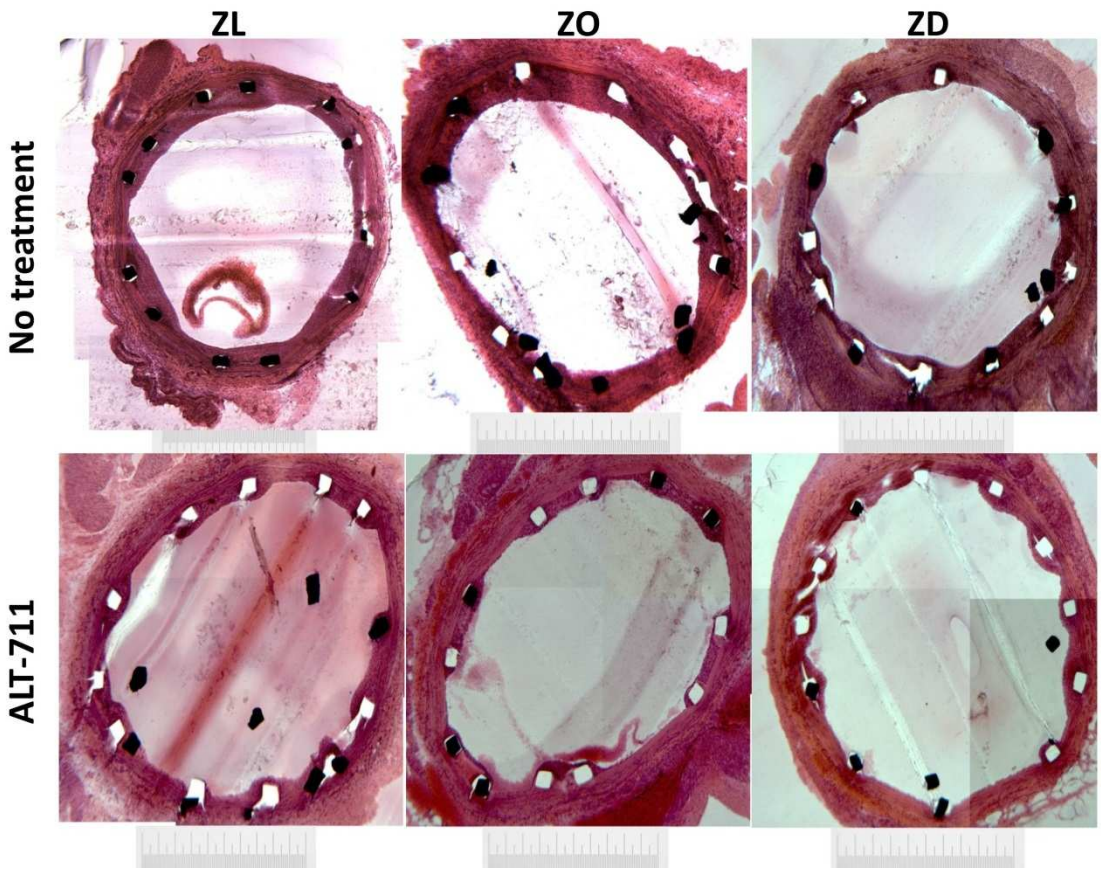

Figure 35. Representative photomicrographs of 5 micron aortic sections from the center of the stented region stained with H&E from ZL, ZO and ZD stented rats (N=6/group). The total length of the scale is 1mm.

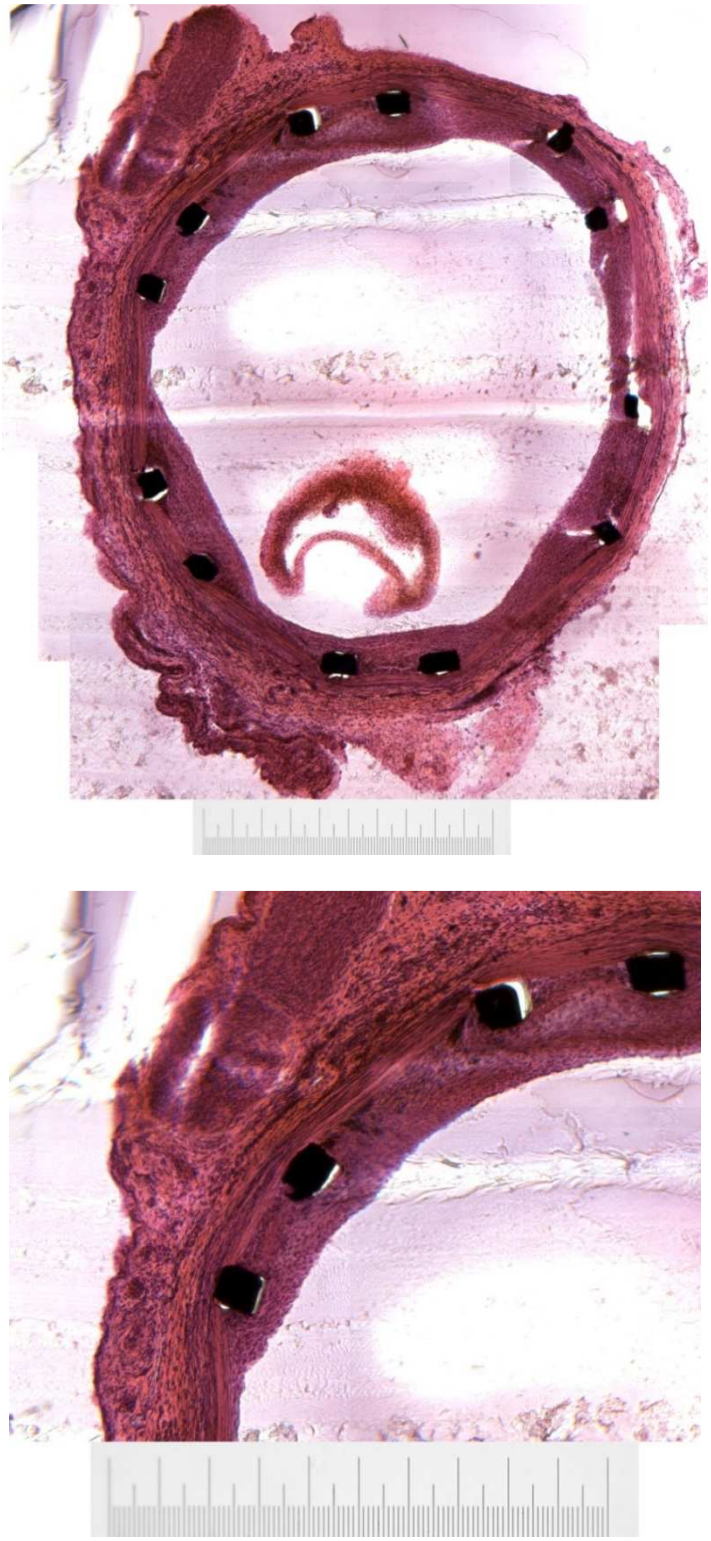

Figure 36. Representative H&E staining of ZL rats without treatment (4X). Whole vessel image (top), and zoomed in image (bottom). The total length of the scale is 1mm.

Figure 37. Representative H&E staining of ZO rats without treatment (4X). Whole vessel image (top), and zoomed in image (bottom). The total length of the scale is 1mm.

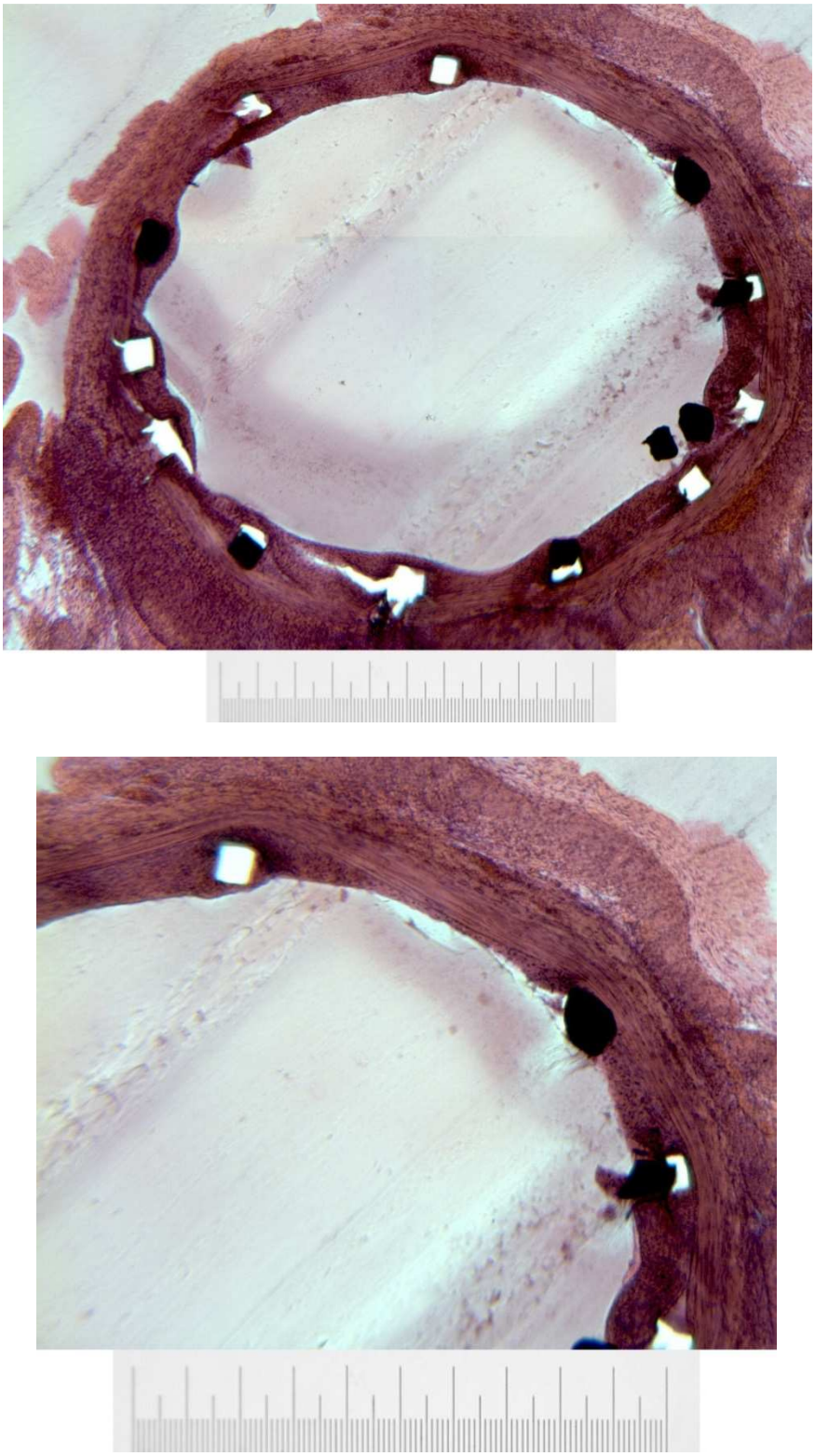

Figure 38. Representative H&E staining of ZD rats without treatment (4X). Whole vessel image (top), and zoomed in image (bottom). The total length of the scale is 1mm.

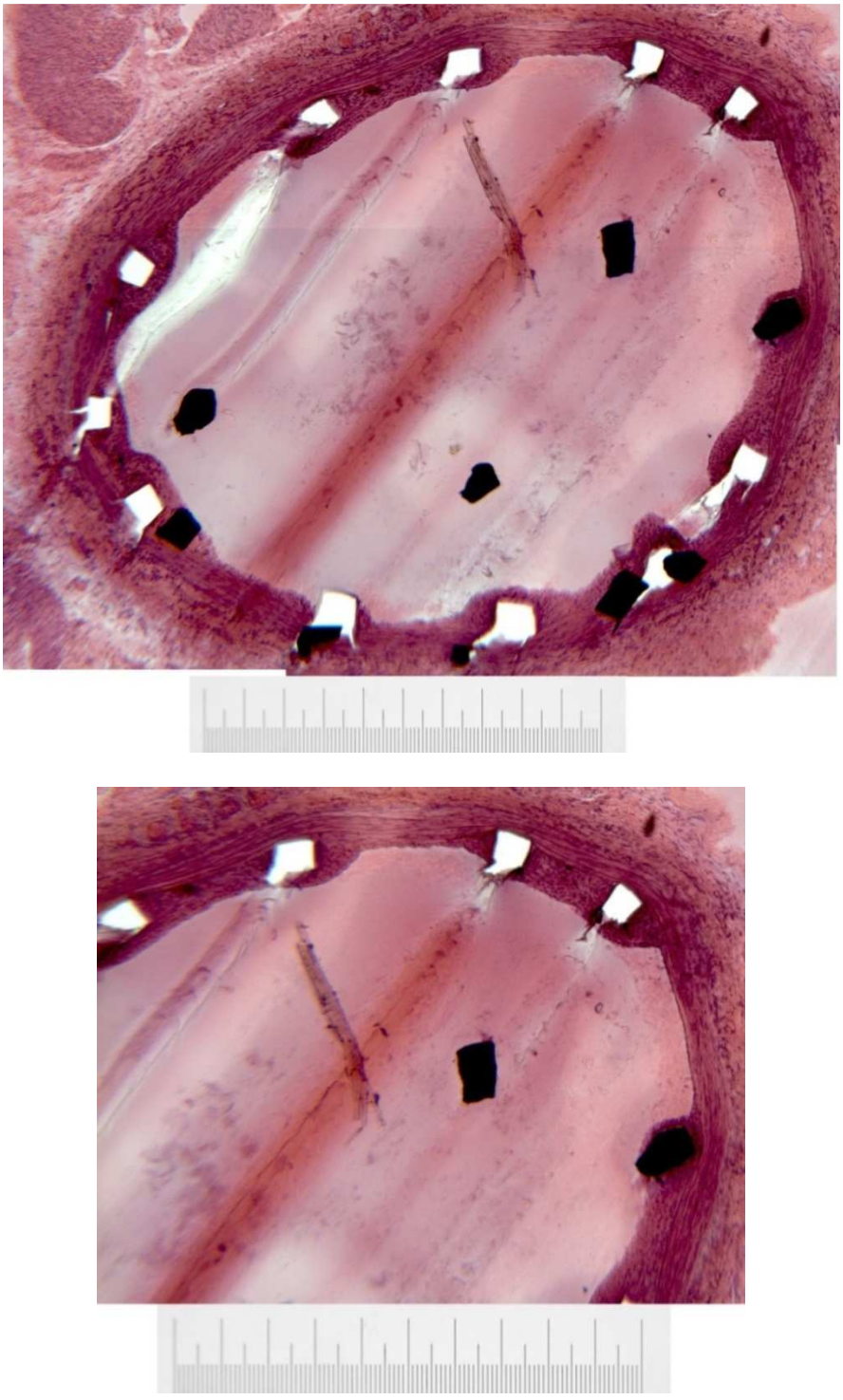

Figure 39. Representative H&E staining of treated ZL rats with ALT-711treatment (4X). Whole vessel image (top), and zoomed in image (bottom). The total length of the scale is 1mm.

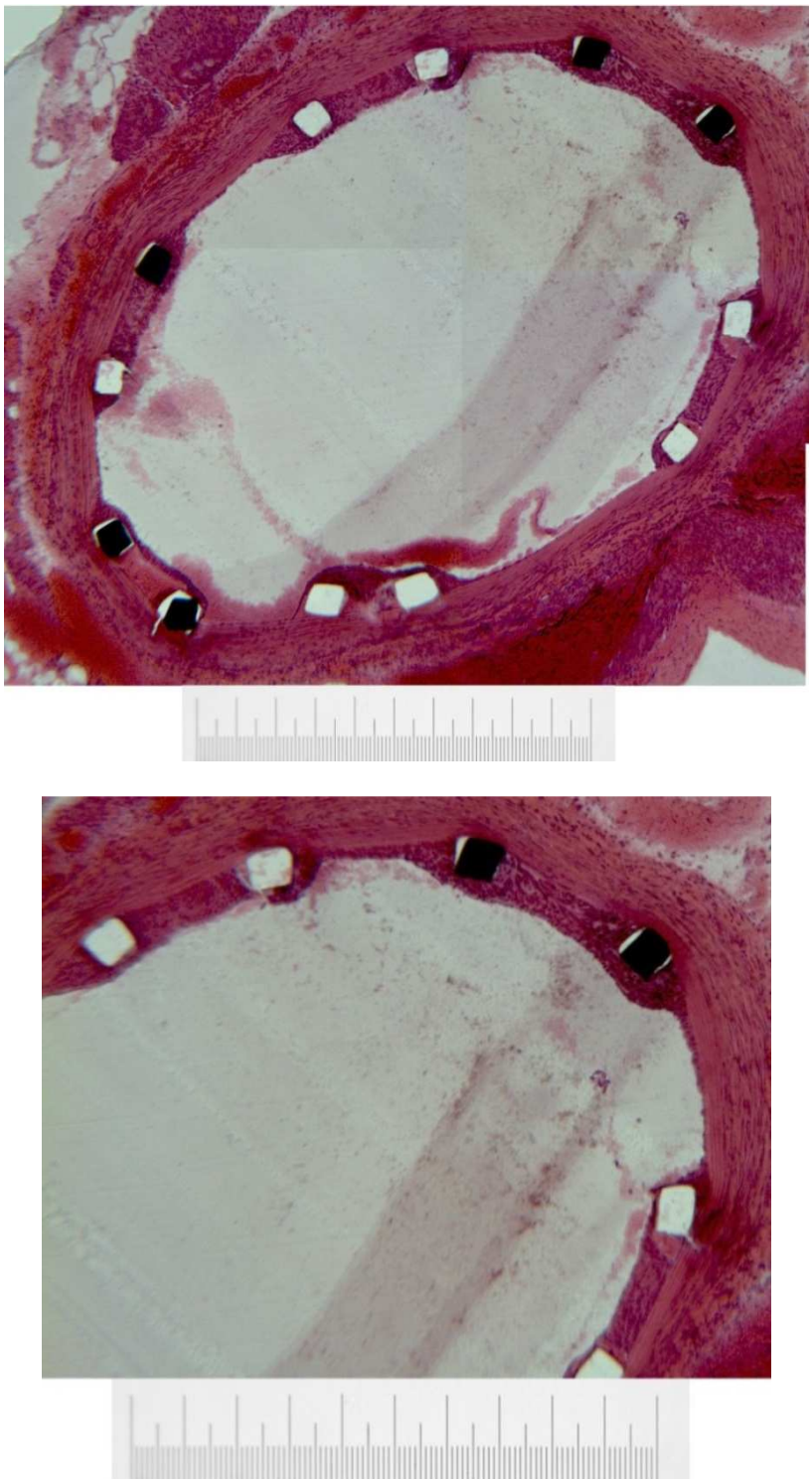

Figure 40. Representative H&E staining of treated ZO rats with ALT-711 treatment (4X). Whole vessel image (top), and zoomed in image (bottom). The total length of the scale is 1mm.

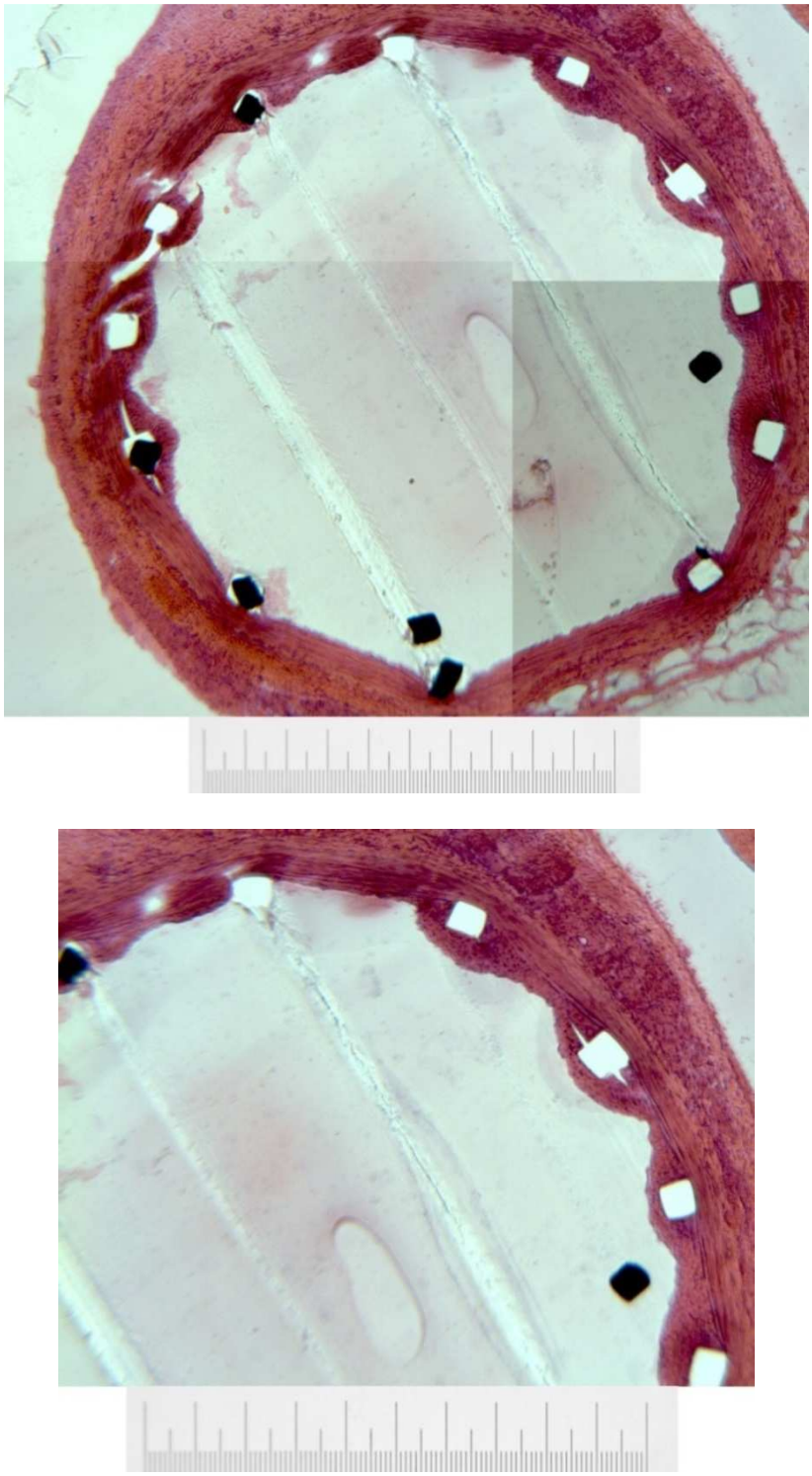

Figure 41. Representative H&E staining of treated ZD rats with ALT-711 treatment (4X). Whole vessel image (top), and zoomed in image (bottom). The total length of the scale is 1mm.

Figure 36 (top) shows blood clots inside of the stented region in a ZL rat without ALT-711 treatment. Care was therefore taken to determine that this was a newly formed blood clot with clear boundaries, as compared to thrombosis generated from blood and stent interaction. Upon microscopic examination of the arterial wall within the section, no significant amount of cell debris or specific inflammatory cells were found before and after ALT-711 treatment.

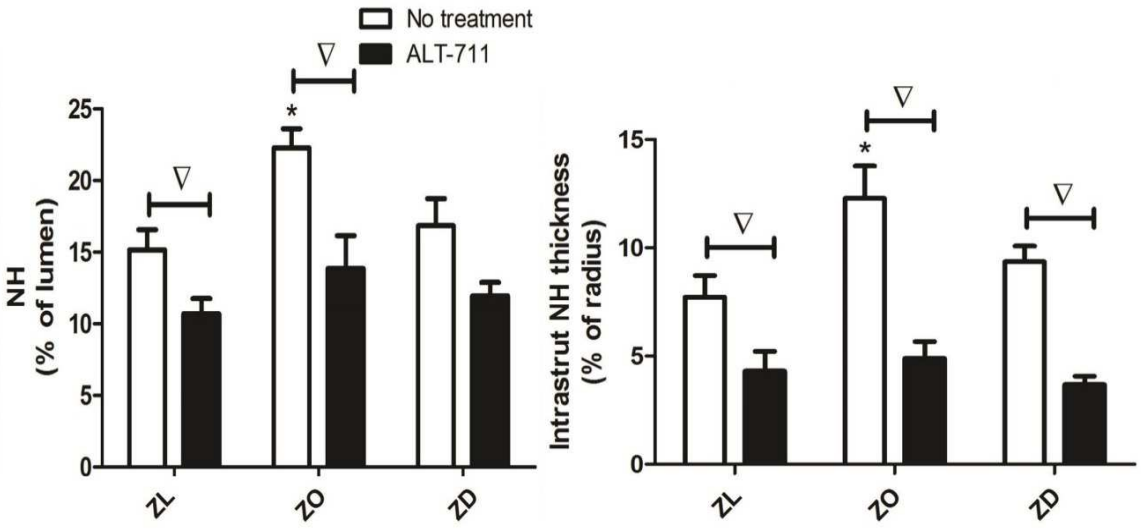

*Figure 42. Histograms depict the percentage of the luminal area bounded by the stent (left) and intrastrut thickness (right) containing neointimal hyperplasia for ZL, ZO and ZD rats (N=6/group); * = significantly different from ZL, ∇ = significant difference within group.*

5.3.4 Vascular Mean Injury Score Analysis

The results of mean injury score analysis are shown in **Figure 43**. No significant differences were found between or within groups of rats before or after treatment. The predominant injury score was less than 1, indicating the internal elastic lamina was generally lacerated, and the media was compressed but not lacerated. This is consistent

with our methods which deployed stents using 3-4 atm in order to achieve a stent-to-vessel deployment ratio in the range of 1.1 to 1.2:1. In contrast, previous research has used deployment pressures of 8 to 10 atm to intentionally introduce injury and the associated arterial response porcine coronary arteries resulting in an average injury score 1.9. Although the endothelial intactness evaluation will be much more clear under a scanning electron microscope, these results suggest that NH findings from the current investigation are more likely associated with mechanical or molecular contributions than the response of arteries to stent-induced vascular injury.

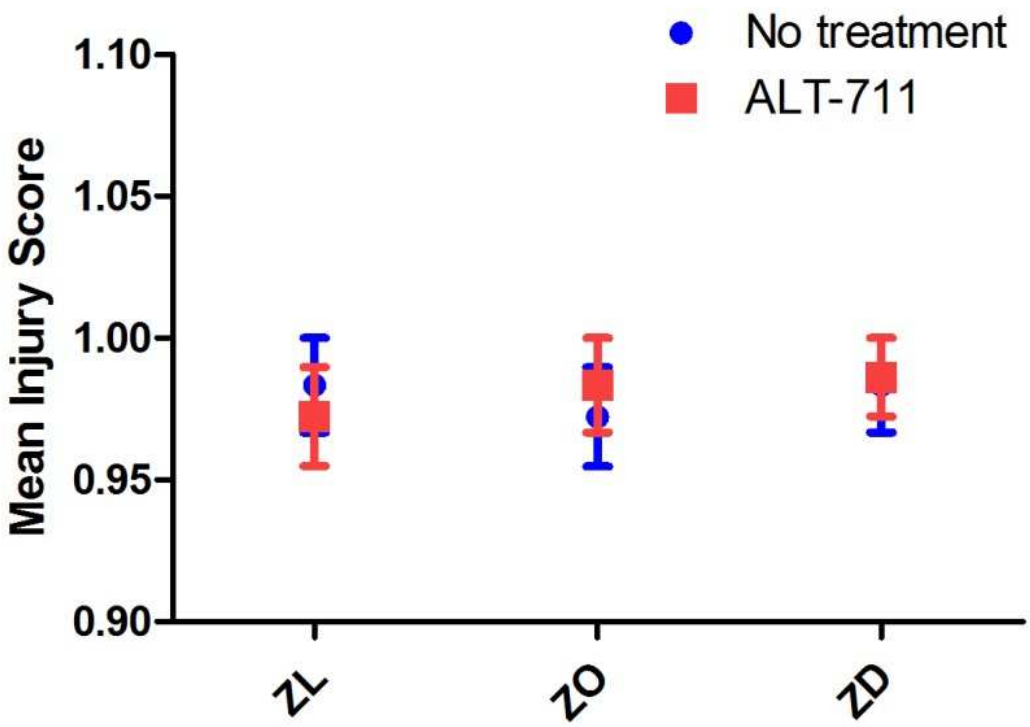

Figure 43. Mean injury score quantified in the middle of the stented region from ZL, ZO and ZD before and after ALT-711 treatment (mean and SEM). No significant differences were found between groups of rats or within groups after treatment.

5.3.5 Protein Expression

An example of AGEs protein expression from three lean rats without ALT-711 treatment is shown in **Figure 44** below. AGEs protein expression results from the vascular segments are shown in **Figure 45-46** and summarized in **Table 10**. AGEs protein expression was increased in the carotid arteries, AAo, and IF of ZD stented rats, but this change was alleviated after ALT-711 treatment with the exception of the AAo as shown in **Figure 45-46**. ALT-711 treatment was also associated with a significant decrease in AGEs expression within the TA and IF of ZO and ZD stented rats. No significant changes for AGEs in arterioles were found for all ZL, ZO and ZD stented rats.

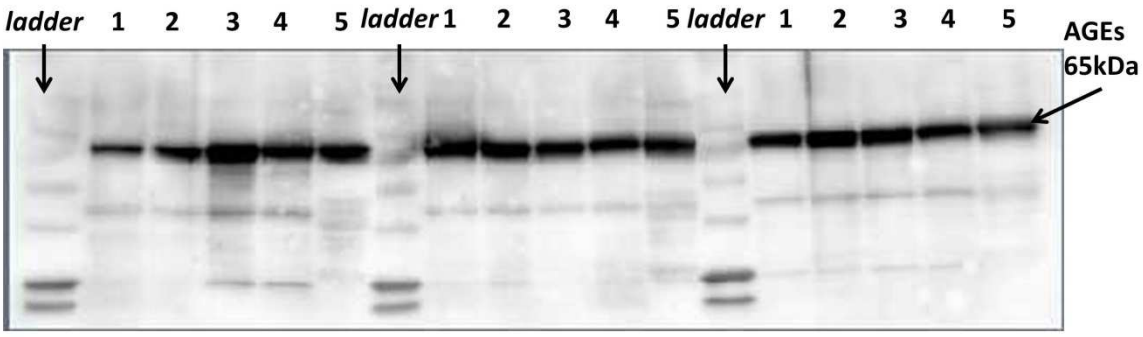

Figure 44. Representative Western Blot image of AGEs protein expression from three ZL rats without ALT-711 treatment. Numbers 1 to 5 correspond to arteries from carotid, thoracic aorta, AAo, IF, and arterioles from cremaster muscle for each rat.

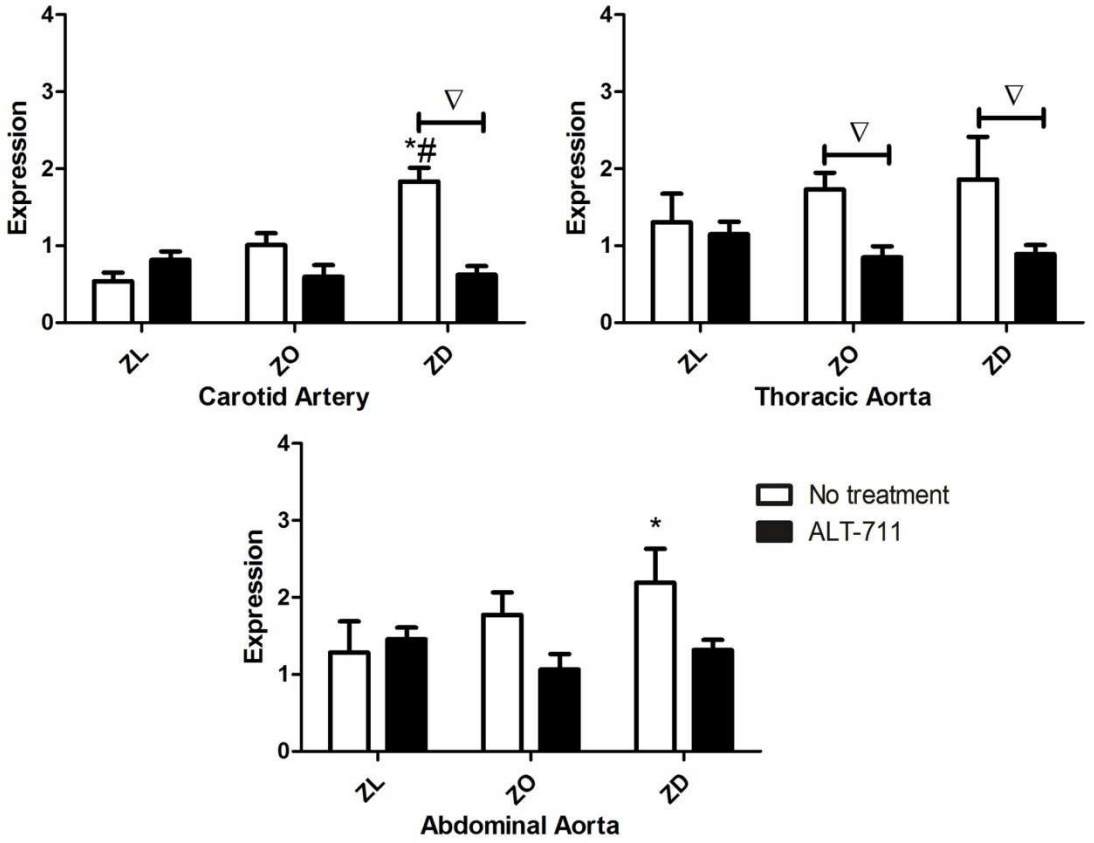

*Figure 45. AGEs protein expression (fold-change over beta tubulin) in carotid artery, TA and AAo (N=6); * = significantly different from ZL stented rats, # = significantly different from ZO stented rats, ∇ = significant difference within group.*

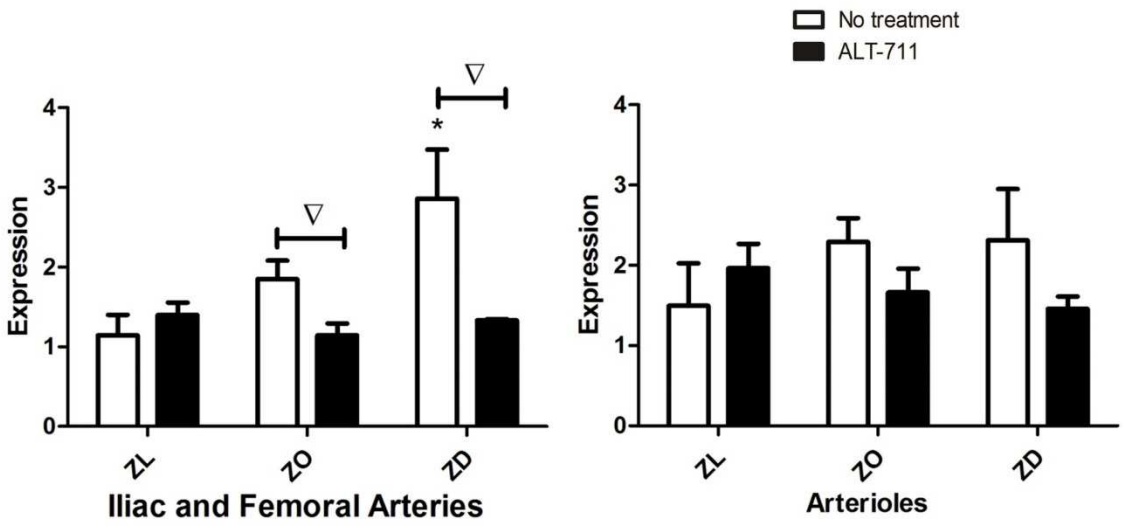

*Figure 46. AGEs protein expression (fold-change over beta tubulin) in IF and arterioles (N=6); * = significantly different from ZL stented rats, and ∇ = significant difference within group.*

Increased RAGE expression was found in the carotid arteries (**Figure 47**), IF, and arterioles (**Figure 48**) of ZD stented rats and was unchanged by ALT-711 treatment. In contrast, RAGE expression was increased in the TA and AAo of ZD stented rats after receiving ALT-711 (**Figure 47**), and decreased in the arterioles for ZL and ZO stented rats after receiving ALT-711.

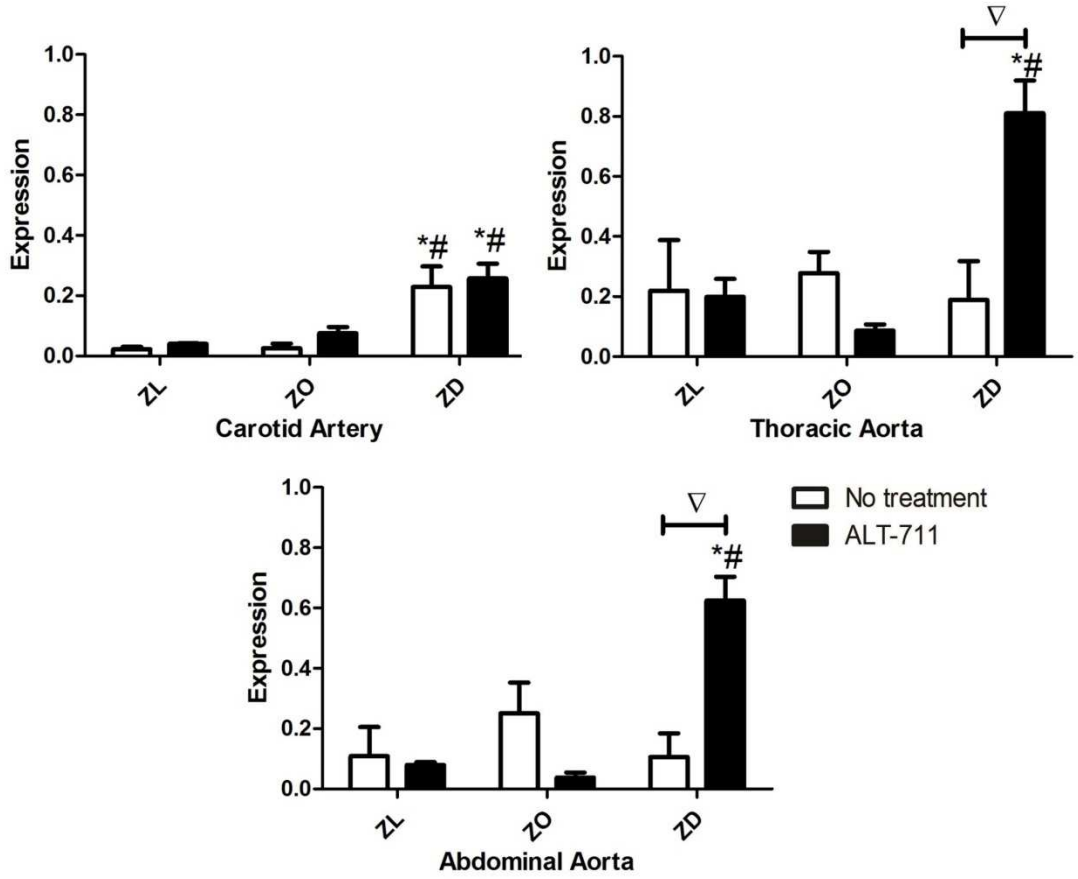

*Figure 47. RAGE protein expression (fold-change over beta tubulin) in carotid artery, TA and AAo (N=6); * = significantly different from ZL stented rats, # = significantly different from ZO stented rats, ∇ = significant difference within group.*

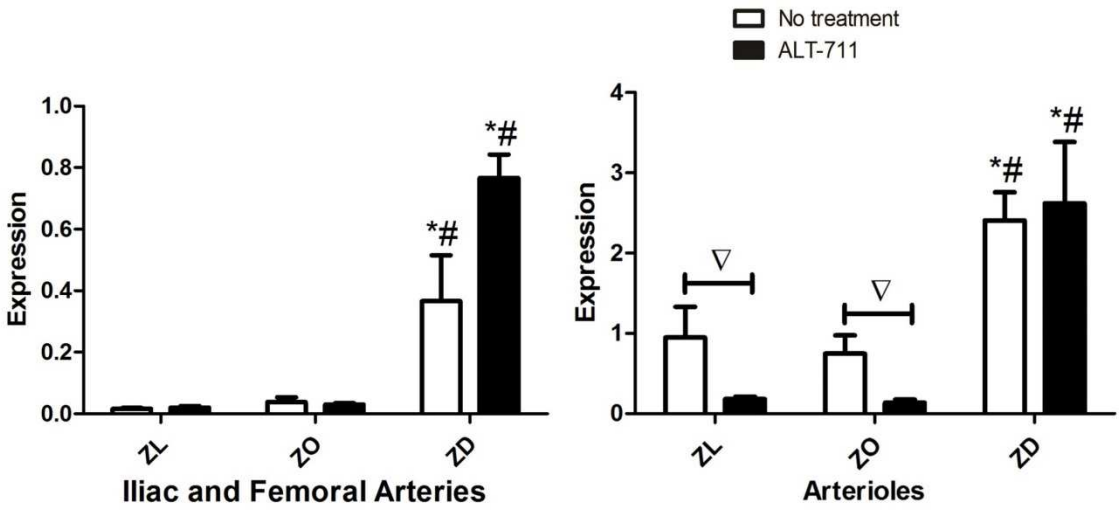

*Figure 48. RAGEs protein expression (fold-change over beta tubulin) in IF and arterioles (N=6); * = significantly different from ZL stented rats, # = significantly different from ZO stented rats, ∇ = significant difference within group.*

TGFβ expression was increased in the TA and IF for ZD stented rats, and was not statistically altered by treatment with ALT-711 (**Figure 49-50**). A significant increase in TGFβ expression was also found in the TA of ZL stented rats after treated with ALT-711.

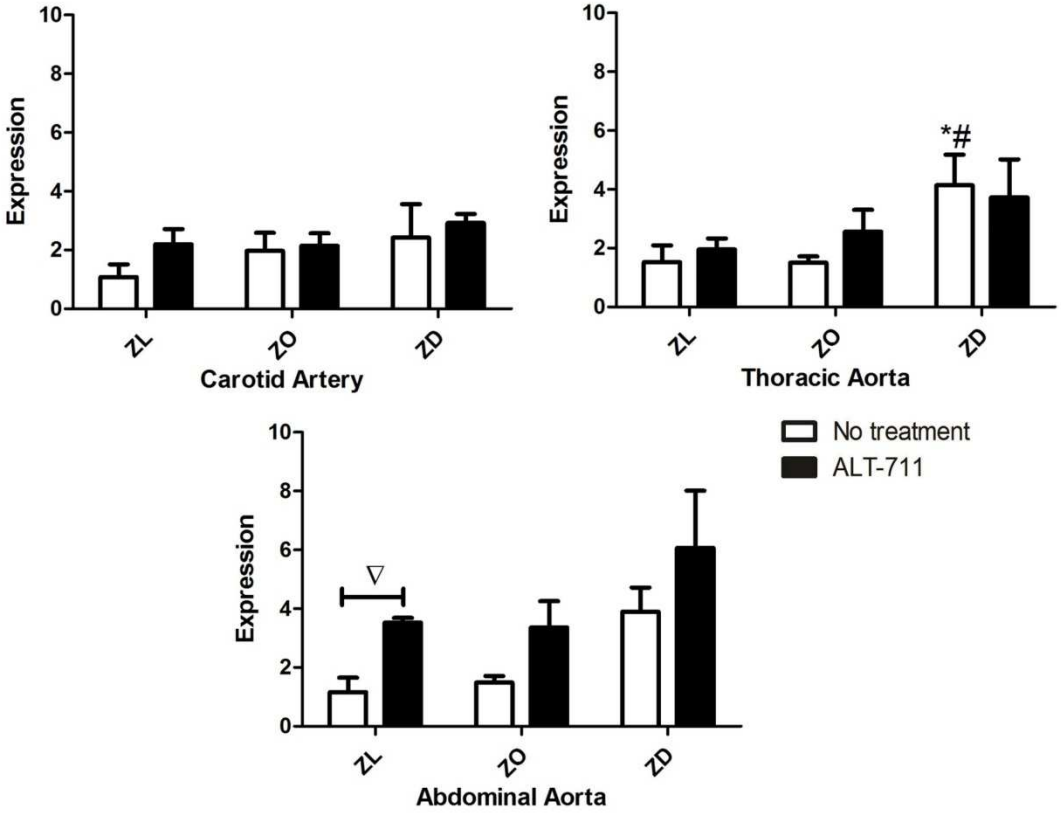

*Figure 49. TGFβ protein expression (fold-change over beta tubulin) in carotid artery, TA and AAo (N=6); * = significantly different from ZL stented rats, # = significantly different from ZO stented rats, ∇ = significant difference within group.*

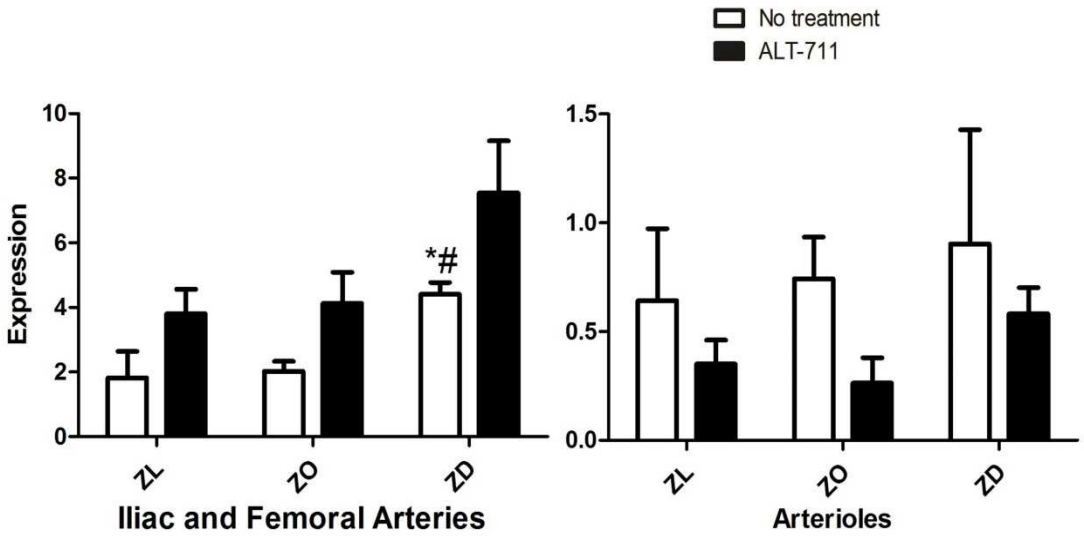

*Figure 50. TGFβ protein expression (fold-change over beta tubulin) in IF and arterioles (N=6); * = significantly different from ZL stented rats, and # = significantly different from ZO stented rats.*

Changes vs. ZL	Carotid Arteries		Thoracic Aorta		Abdominal Aorta		Iliac and Femoral Arteries		Arterioles	
	ZO	ZD	ZO	ZD	ZO	ZD	ZO	ZD	ZO	ZD
Collagen x-linking	NC	NC	NC	NC	NC	NC	↑	↑	NC	↑
AGEs	NC	↑	NC	NC	NC	↑	NC	↑	NC	NC
RAGE	NC	↑	NC	NC	NC	NC	NC	↑	NC	↑
TGFβ	NC	NC	NC	↑	NC	NC	NC	↑	NC	NC

Table 10. Summary of AGEs related collagen cross-linking and protein expression changes for vessels in ZO and ZD rats, relative to respective values in ZL rats. (N=6/group), NC means no change, ↑ means significant increase, diagonal means increase was alleviated by ALT-711

5.4 Summary

The objective of this Aim was to quantify AGEs related collagen cross-linking and protein expression in multiple arterial locations to elucidate molecular changes contributing to NH after stenting for T2DM, and determine whether these adverse changes can be alleviated by ALT-711. There were several important findings.

1) Quantification of protein expression was conducted using Western blotting in the carotid arteries, TA, AAo, iliac and femoral arteries as well as arterioles in stented T2DM rats. AGEs protein expression was located in nearly all vascular locations of ZD stented rats, confirming their elevated presence in

T2DM, which is in agreement with previous research that formation of AGEs occurs more rapidly in diabetic conditions [26, 27].

2) Increases in AGEs related collagen cross-linking within the arterioles of ZD stented rats were absent after treatment, suggesting ALT-711 preferentially reduces vessel AGE-induced stiffness in distal vessels. These findings are consistent with previous studies showing that AGEs related cross-linking is one of the factors in vascular stiffening, and ALT-711 can reduce established AGEs and collagen cross-linking [119], arterial stiffening, while enhancing cardiac output [120, 121, 141].
3) Intra-strut NH within the stented region was found to be greater for ZO stented rats, but not ZD stented rats. Additionally, ALT-711 treatment reduced intra-strut NH in all groups suggesting different pathways may mediate the local NH response.
4) Quantification of TGFβ and RAGE protein expression were also conducted using Western blotting in the carotid arteries, TA, AAo, IF as well as arterioles in stented ZL, ZO and ZD stented rats. TGFβ expression was not influenced by treatment with ALT-711, and RAGE expression was increased in ZD stented rats with or without ALT-711.

5.5 Potential Limitations

The present specific aim used a histological method to analyze NH in the stented region 21 days after stent surgery. NH formation was not captured in real time, but could be obtained by using intravascular ultrasound or optical coherency tomography. However, these approaches are costly and require specialized equipment that was not available for

the current investigation. The rat abdominal aorta is also relatively small, potentially limiting the use of these techniques.

It would be more accurate to quantify collagen using high-performance liquid chromatography. However, this technique requires extra training to perform that is beyond the scope of expectations for the current work. To address this limitation, the procedure described above was generated to quantify collagen cross-links based on a Sirius red method [152], which can detect collagen with reasonable accuracy.

Due to the limited amount of sample that can be obtained from the rat vasculature studied here, it was only possible to detect the expression of some proteins in response to T2DM. However, there are many pathways involved in the NH formation process, and future work should evaluate the protein expression of these pathways. Nonetheless, analysis from AGEs, RAGE and TGFβ as presented should provide fundamental knowledge for future studies and may prompt future investigations in humans.

CHAPTER 6: DISCUSSION

6.1 Discussion of Aim 1 and 2

The objective of this investigation was to test the hypothesis that elevated NH observed after BMS implantation in T2DM is mediated by local changes in hemodynamics within the stented region that arise secondary to vascular remodeling, increased formation of AGEs, and increased DVR. Furthermore, it was hypothesized that a pharmacological strategy to decrease AGEs using ALT-711 could reduce NH in T2DM. There were several important findings of the study that indicate interrelationships between mechanical and mechanistic processes that govern the development of NH in obesity and diabetes. 1) AGEs were located in nearly all vascular locations of ZD rats, confirming their elevated presence in T2DM; 2) increasing stiffness, as indicated by collagen cross-linking, was localized to the arterioles of ZD rats, but alleviated by treatment with ALT-711; 3) mean BF decreased in ZD rats, concomitantly with trends toward increases in arteriolar resistance; 4) TAWSS within the stent was low in untreated ZD rats; 5) NH within the stent was increased in ZO but not ZD rats, but treatment reduced NH in all groups; 6) TGFβ and RAGE expression was not alleviated by ALT-711 suggesting different pathways may mediate the local NH response. These findings are discussed in more detail below.

Formation of AGEs and collagen cross-linking occurs more rapidly during diabetic conditions [26, 27]. Therefore, it is reasonable to propose that associated changes in vascular stiffness alter mechanical properties of vasculature including increase local and distal resistances, and adversely influence NH after stenting. For example, AGEs-

induced remodeling and elevated DVR may lead to pronounced vascular damage during stenting and localized reductions in WSS, which are associated with NH [157, 158]. Increased AGEs expression in the arterioles of ZD rats in the current investigation appears to decrease BF by increasing downstream vascular stiffness and resistance. Increased AGEs related collagen cross-linking within the arterioles of ZD rats were absent after ALT-711 treatment, suggesting that this cross-link antagonist preferentially reduces AGE-induced resistance in distal vessels. These findings are consistent with previous studies showing that AGEs related cross-linking is an important factor that promotes vascular stiffness in arterioles. The current findings are also supported by prior studies showing ALT-711 reduces established AGEs and collagen cross-linking [119], decreases arterial stiffness, and enhances cardiac output [120, 121, 141]. Kass et al. [141] also found that ALT-711 could alleviate vascular dysfunction and wall stiffness without changing mean arterial pressure, which is consistent with the current results.

While local changes in stiffness mentioned above may influence diameter and the neointimal response of an artery to stent-induced injury, low TAWSS within the stented region can also influence NH through mechanotransduction via several signaling pathways [159, 160]. To our knowledge, this is the first investigation comparing TAWSS between lean, obese and T2DM rats. The current results demonstrate TAWSS from intrastrut regions within the middle of the stent were reduced for ZD as compared to both ZL and ZO rats. This finding is likely due to observed reductions in BF, and hence lower velocity and TAWSS, within the stented region concomitant with higher downstream vascular resistance.

Interestingly, NH was highest in ZO, as compared with ZD and ZL rats. These results are consistent with those reported by Jonas et al. [161], who similarly observed elevated NH in ZO as compared to ZL and ZD rats. Several other studies also found severely hyperglycemic animals to have NH equal to or even decreased relative to controls [162, 163]. Thus, the interplay between biomechanical and molecular mechanism during NH, obesity, and diabetes is complex. The ras-raf-MAPK-ERK and phosphoinositide 3-kinase (PI3K) pathways may be involved in NH within the stented region as these kinases play key roles in transducing mitogenic signals from the plasma membrane to the nucleus of cells. Jonas et al. [161] suggested that hyperglycemia in ZD animals may not be sufficient to activate the ERK pathway and increase NH formation. In contrast, very high insulin levels present in obese rats may shift signaling from the Akt pathway toward the ERK pathway resulting in cellular proliferation and migration. Balloon induced arterial injury has been shown to stimulate medial SMC proliferation along with MAPK phosphorylation [164]. In addition, the PI3K - protein kinase B (PKB or Akt) pathway is also important in apoptosis, proliferation and cell migration. Previous findings have suggested that activation of the PI3K pathway in T2DM and the metabolic syndrome is associated with a high risk of atherosclerosis and restenosis [34]. Jonas et al. [161] demonstrated that activation of and the balance (p-ERK/p-Akt ratio) between ERK and Akt activation after rat aortic stenting correlated with NH in diabetes. A decrease in intrastrut NH thickness (percentage of radius) was found in all groups with ALT-711 treatment. This is consistent with previous research by Kim et al. [129] who used ALT-711 to treat balloon injured carotid arteries of diabetic rats and observed a significant decrease in NH [129].

TGFβ is involved in the wound healing process, and has been shown to be activated in human restenotic lesions after porcine coronary artery stenting [94, 95]. TGFβ promotes extracellular matrix production and cellular proliferation as evidenced by enhanced NH when the TGFβ gene was transferred into normal porcine arteries [96]. However, we found that TGFβ expression was not influenced by treatment with ALT-711, which was inconsistent with previous studies showing increased TGFβ protein expression in regions adjacent to stent struts as early as 5 days after stenting [94, 95]. Our results may have differed from prior investigation because we sampled tissue adjacent but not within the stented region. The stented region of rats in the current investigation was used for CFD or quantification of NH.

RAGE was first isolated from bovine lung endothelium and belongs to the immunoglobulin superfamily of cell-surface molecules [165, 166]. RAGE has been proposed to be a key factor leading to AGEs accumulation and subsequent endothelial dysfunction. Specifically, the interaction of AGEs and RAGE activate endothelial adhesion molecules like VCAM-1, NF-kB, PKC, ERK, and TGFβ[6, 98, 167], which accelerate atherosclerosis by enhancing monocyte adhesion and vascular permeability [168, 169]. AGEs expression was increased in the carotid arteries, AAo, and iliac and femoral arteries of ZD rats. These changes were alleviated by ALT-711 and were consistent with previous evidence showing that ALT-711 can reduce AGEs accumulation and attenuate atherosclerosis in diabetic mice [121]. In contrast, RAGE expression was increased in ZD rats with or without ALT-711. Previous studies showed that ALT-711 decreased RAGE protein expression [121, 130]. However, these studies were not tested

in the stented diabetic condition, and the dose may be a factor of RAGE expression since a lesser dose of ALT-711 was used in the current investigation.

Several mechanisms may be responsible for the observed inconsistent RAGE protein expression in the current investigation. From the prospective of ALT-711, this drug reverses collagen cross-linking mediated by AGEs [170], but may not directly alter RAGE expression. RAGE belongs to the immunoglobulin superfamily, composed of one variable-type immunoglobulin domain and two different constant domains [166]. All these domains can bind to different ligands, so that RAGE can be activated not only by AGEs, but also by the S100/calgranulins family of proinflammatory molecules, high-mobility group box-1 (HMGB-1), beta-sheet fibrils, amyloid-beta peptide, and the beta2-ingegrin Mac-1 [171]. These findings suggest that isolated modification of AGEs expression after treatment by ALT-711 many not modulate all pathways that can activate RAGE. In addition, Watson et al. [172] reported that ALT-711 decreased AGEs in a diabetic mouse model with genetic deletion of RAGE (knockout). Thus, AGEs may also signal through RAGE-independent pathways.

However, to our surprise, we observed some vessels had increased RAGE expression after ALT-711 treatment. Interestingly, previous research has suggested more complex regulation for RAGE proteins. RAGE is a common receptor present in the endothelium, vascular cells, and inflammatory cells, and it was found to increase expression in stress or injury conditions [173]. Although only one gene is coding RAGE, there are several variants and results of multiple splicing of this gene were detected including endogenous secretory soluble RAGE (esRAGE) and soluble RAGE (sRAGE) [166]. esRAGE forms as result of alternatively spliced pre-mRNA and has

characteristics of lacking the membrane and intracellular domains, and sRAGE may form by cleaving RAGE from the cell membrane by the action of MMP and A Disintegrin And Metallopeptidase 10 [174, 175]. Recent *in vitro* studies found that soluble RAGE has the ability to block the RAGE pathway which decreases inflammatory reaction, cellular migration and proliferation [100, 102]. In *in vivo* studies, soluble RAGE has been found to decrease atherosclerosis in diabetic and non-diabetic mice without changing glucose, cholesterol or triglyceride levels [103, 176], so that soluble RAGE may provide protection in the cardiovascular system. We found that RAGE expression was increased in some vessels after ALT-711 treatment in ZD rats, which may be because ALT-711 can protect cardiovascular system by increasing the expression of sRAGE. This hypothesis remains to be tested in future follow-up studies.

6.2 Unique Methodological Contributions of the Current Investigation

The abdominal aortic stenting protocol used for the current investigation is a specialized method, and only few labs in the world have demonstrated proficiency with this approach [66, 126, 177]. The methods applied in the current work were adapted from the TSI-Lab, Heart Center and Cardiovascular Research Center, at the University of Hamburg, in Germany. The scarcity of this approach can be appreciated relative to supplies used for the investigation. The size of the AAo (~1.7 mm) is smaller than the tip of a typical ballpoint pen (~2.4 mm), the diameter of the 8-0 suture employed to close the incision used for stenting in this investigation (0.04 mm) is less than half the diameter of a human hair, and the actual working space accessed under microscopic guidance is approximately the area of a penny (**Figure 51**). The need to complete the surgical and stenting procedure quickly to limit the time the rat's BF was blocked further contributed

to the challenge of this approach. Dietary conditions for ZL, ZO and ZD rats were not changed before and after surgery, resulting in an increased risk of intestinal impaction that was also occasionally observed.

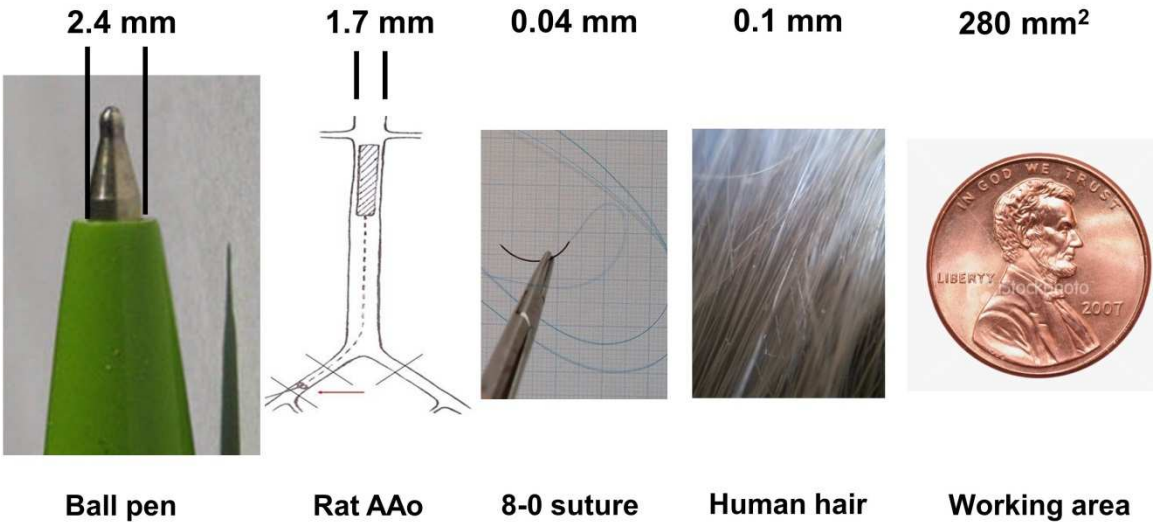

Figure 51. Working scale for the current investigation. The size of the AAo (~1.7 mm) is smaller than the tip of a typical ballpoint pen (~2.4 mm), the diameter of the 8-0 suture employed to close the incision used for stenting in this investigation (0.04 mm) is less than half the size of a human hair, and the actual working area accessed under microscopic guidance is the size of a penny.

Glycol methyl methacrylate H&E staining was optimized several times with guidance by Jeffrey Toth, PhD and Sara Landschoot, BS (histological specialist). Poor initial staining results were remedied using several key steps. First, H&E staining steps needed to be longer to ensure infiltration into the plastic section. Next, the steps for series dehydration needed to be as gentile as possible to keep the plastic sections adhered to the slides. These dehydration steps also needed to be performed rapidly to maintain the eosin color. Care also needed to be taken to avoid air bubbles in the coverslip step that could prevent quantification of NH later.

The process described above for AGEs related collagen cross-linking was also optimized for the current investigation. The procedure was combined from several papers over the past 50 years [151, 178]. The basic idea behind this approach was to expose the collagen first, digest the banded AGEs to measure fluorescence, and use Sirius red to quantify collagen using a spectrophotometer. It would have been more accurate to use high-performance liquid chromatography (HPLC) for quantification. However, HPLC is complex to operate, and requires substantial more time to optimize the procedure. In contrast, the Sirius red method has proved useful to quantify collagen in the solution through prior research [152]. In addition, we used a 0.5 μM concentration of Sirius red to quantify collagen because a linear relationship has been found between Sirius red and optical density, and that a 0.5 μM concentration of Sirius red was suitable for collagen quantification without saturation [152].

The protein isolation steps presented in the methods section have also been optimized for the current work. A mortar and pestle were initially considered to homogenize vascular tissue. However, this was extremely laborious as it was necessary to keep the mortar on ice while the tissue was ground for 2 hours. This method also wastes precious vascular sample when transferring from the mortar to different tubes for subsequent steps. Instead, this work used the TissueLyser LT to homogenize the tissue. This approach reduced the homogenization time to 10 minutes to finish and reduced the loss of sample from transferring. The density of protein bans was similar to prior results thereby confirming this homogenization method was appropriate.

6.3 Glucose, Insulin, NH formation and ALT-711 Treatment

6.3.1 Glucose and NH Formation

Our data show that blood glucose concentrations were similar within groups before and after ALT-711 treatment. However, we observed a significant decrease in intrastrut NH thickness after ALT-711 treatment in all rats. This result is consistent with previous studies [163] that glucose concentration is not predictive of the severity of NH formation, and other mechanisms may be involved after ALT-711 treatment. In addition, Park et al. [163] found that there was no significant correlation between NH formation and glucose, exogenous insulin administration, cholesterol, and triglyceride levels. These results also suggest purely decreasing glucose after ALT-711 treatment may not reduce NH formation.

6.3.2 Glucose and ALT-711

In this investigation, we found that blood glucose concentration was significantly elevated for ZO and ZD as compared to ZL rats. Although there was a trend toward decreased blood glucose concentration for all rats with ALT-711 treatment, this decrease did not reach significance and values remained elevated compared to ZL rats. A similar result was observed for previous research. Asif et al. [120] found that glucose levels were similar in dogs before and after ALT-711 treatment. Research by Candido et al. [130] also showed that glucose levels were higher in diabetic Sprague-Dawley rats than non-diabetic rats; and remained higher in diabetic Sprague-Dawley rats than non-diabetic rats after ALT-711 treatment.

6.3.3 Insulin and NH Formation

There have been a few studies correlating insulin in diabetes with NH formation after vessel injury. Park et al. [163] used balloon angioplasty to injure rat carotid arteries, and compared NH formation in lean as well as T1DM and T2DM rats. They found that NH formation was significantly increased in T2DM rats. In contrast, the NH response for T1DM rats was similar to lean rats. In addition, Park et al. included insulin-treated and insulin-untreated rat groups to study the influence of insulin on NH. There was no significant correlation between NH and exogenous insulin administration, glucose, cholesterol, and triglyceride levels. In contrast, other researchers have also correlated insulin with restenosis formation. Nordt et al. [179] found that insulin can adjust the balance between thrombosis and fibrinolysis. In addition, insulin can promote migration and proliferation of SMC [180]. Marso et al. [181] also reported a > 2 fold increase in revascularization rate with 6-month for insulin resistant as compared to non-insulin resistant diabetic patients. Collectively, these studies suggest insulin-resistance might be a major factor for NH formation in diabetic patients.

6.3.4 Insulin and ALT-711

The influence of ALT-711 on insulin levels has been discussed in several previous studies, but only one is directly related to the current investigation. Hiramatsu et al. [140] found that ALT-711 did not influence insulin secretion, and hence, β-cell function under *in vivo* as well as *in vitro* conditions. In this study[140], ALT-711 was administered at a low concentration (0.1mg/kg/day) by gavage which might be broken down in the digestive tract. It remains to be determined if ALT-711 my influence β-cell

function and insulin at higher concentrations such as that given in the current investigation (1mg/kg/day, IP).

CHAPTER 7: FUTURE DIRECTIONS AND CONCLUSIONS

7.1 Future Directions

This investigation used two specific aims involving mechanical and molecular aspects influenced by T2DM. From a mechanical perspective, CFD modeling was used to quantify the influence of WSS in stented arteries of T2DM rats. From a molecular perspective, analysis of NH in the stented region was performed using H&E for correlation to CFD results. AGEs related collagen cross-linking, and protein expression quantification was also conducted in the carotid arteries, TA, AAo, iliac and femoral arteries as well as arterioles in stented T2DM rats. This multidisciplinary approach leveraged an animal model of T2DM to further elucidate the mechanisms of restenosis that may be applicable to this patient population. The findings in this investigation may lend themselves to future research and treatment of NH in obese and diabetic patients after stent treatment. These may especially include the identification of key inhibitors such as PAR-1 inhibitor, Parstatin, or Metformin, and further uncover the molecular pathways. These are explained in more detail below.

7.1.1 PAR-1 Inhibitor and Parstatin

Platelet activation is an important step in the process of restenosis. It has been found that three major pathways involved in this platelet activation process are 1) thromboxane A_2 ($TBXA_2$) reacting with the $TBXA_2$ receptor; 2) adenosine diphosphate (ADP) reacting with the purinergic receptor ($P2Y_{12}$); 3) thrombin reacting with the protease-activated receptor (PAR1) [182]. Previous researchers have found that thrombin reacting with the PARs may be more important than the other two processes [145]. PAR1

is a G protein-coupled receptor involved in vascular development and can mediate thrombin activities [183, 184]. PAR1 has been found on different cell types such as vascular SMC, endothelial cells, and platelets. PAR1 activation is through cleavage of the Arg41/Ser42 in the N terminal, most likely by thrombin. The new truncated N terminus will serve as the tethered ligand to activate PAR1. RAR1 inhibitors such as vorapaxar and atopaxar, may provide additional treatment method to reduce in stent restenosis. During PAR1 activation, a small size N terminal peptide is separated by thrombin as discussed above. This small 41 peptide was named parstatin, and it has been found that parstatin could be a potent antiangiogenic factor for clinical usage [185]. Parstatin may be useful for alleviating in stent restenosis in T2DM as well.

7.1.2 Metformin

Metformin is mainly used as an anti-hyperglycemic agent especially in obese or overweight T2DM. It works as an insulin sensitizer to decrease endogenous and exogenous insulin and may protect the cardiovascular system [186, 187]. Kao et al. used Metformin for diabetic patients undergoing percutaneous intervention, where decreased death and myocardial infarction were found [188]. It has been also reported that long term use of metformin may cause metabolic disorder or lactic acidosis. However, no lactic acidosis cases were found in data recently collected from 70,490 patients using metformin [189]. Therefore, it is reasonable to hypothesize that using metformin may decrease insulin and influence glucose, which may decrease AGEs formation and NH in T2DM condition. This hypothesis remains to be tested.

7.1.3 Molecular Pathways

The ras-raf-MAPK-ERK and PI3K pathways are likely involved in the NH process within the stent region as they play a key role in transducing mitogenic signals from the plasma membrane to the nucleus of cells. It has been found that ERK pathway activation will result in cellular proliferation and migration, and studies have shown that balloon induced arterial injury will stimulate medial SMC proliferation along with MAPK phosphorylation [164]. In addition, the PI3K - PKB is important in apoptosis, proliferation and cell migration. Studies have found that the PI3K pathway involved in both T2DM and the metabolic syndrome are associated with a high risk of atherosclerosis and restenosis [34]. Jonas et al. [161] studied both of these pathways, and found activation of ERK and Akt after rat aortic stenting, as well as the balance between ERK and Akt activation (p-ERK/p-Akt ratio) correlate with NH in diabetes.

Besides these pathways, Watson et al. [172] reported an experiment using ALT-711 to treat diabetic RAGE knockout mice. Surprisingly, ALT-711 still reduced AGEs levels, suggesting AGEs may also work through RAGE-independent signaling pathways. Investigations about protein expression in stenting RAGE knockout T2DM rats may provide ideas about how these proteins are related and regulated.

7.2 Conclusions

This work used a specialized approach to investigate the problem of restenosis after T2DM stenting from the perspective of engineering and biology whereby CFD modeling was used to demonstrate the influence of local and distal vascular changes caused by AGEs on BF, BP, and distribution of WSS. Histology was used to quantify the

NH in stented region; spectrophotometry was used to quantify AGEs related collagen cross-linking, and Western blotting was applied to quantify protein expression.

In summary (**Figure 52**), the current results demonstrated that the cross-linking antagonist, ALT-711, decreased AGEs related collagen cross-linking and arteriolar stiffness in obese and diabetic rats after stent implantation. ALT-711 deceased AGEs related collagen cross-linking, increased local blood flow, decreased DVR, and was not associated with differences in regional distributions of WSS between groups, suggesting that vascular biomechanics may play a prominent role during NH in stented arteries. The finding that ALT-711 treatment reduced NH in lean, obese and diabetic rats suggests this agent may be effective to decrease stent restenosis regardless of patient glycemic status. However, this hypothesis remains to be further tested.

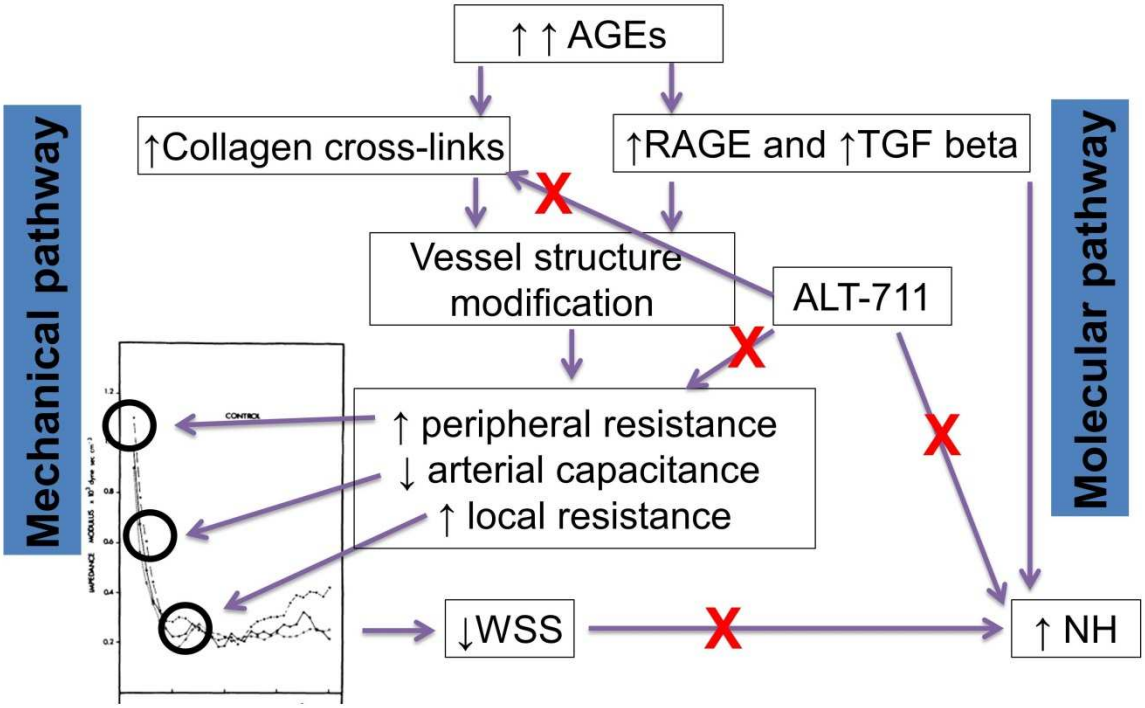

Figure 52. The mechanical and molecular pathways tested for T2DM in this investigation. ALT-711 decreased AGEs related collagen cross-linking and arteriolar stiffness in obese and diabetic rats after stent implantation. "X" indicates a location of inhibition by ALT-711 or difference from previously observed relationships. ALT-711 deceased AGEs related collagen cross-lining, increased local blood flow, decreased DVR, and was not associated with differences in regional distributions of WSS between groups. ALT-711 treatment reduced NH in lean, obese and diabetic rats. No significant differences were noted for RAGE and TGFβ expression. However, other related pathways remain to be tested.

REFERENCES

1. Khan, W., S. Farah, and A.J. Domb, *Drug eluting stents: developments and current status.* J Control Release, 2012. **161**(2): p. 703-12.

2. Zamir, M., *On fractal properties of arterial trees.* J Theor Biol, 1999. **197**(4): p. 517-26.

3. Nichols, W.W., M.F. O'Rourke, and D.A. McDonald, *McDonald's blood flow in arteries : theoretic, experimental, and clinical principles*. 5th ed. 2005, London, New York: Hodder Arnold, Distributed in the U.S.A. by Oxford University Press. xii, 607 p.

4. Schwartz, R.S., et al., *Restenosis and the proportional neointimal response to coronary artery injury: results in a porcine model.* J Am Coll Cardiol, 1992. **19**(2): p. 267-74.

5. LaDisa, J.F., Jr., et al., *Alterations in wall shear stress predict sites of neointimal hyperplasia after stent implantation in rabbit iliac arteries.* Am J Physiol Heart Circ Physiol, 2005. **288**(5): p. H2465-75.

6. Welt, F.G. and C. Rogers, *Inflammation and restenosis in the stent era.* Arterioscler Thromb Vasc Biol, 2002. **22**(11): p. 1769-76.

7. Aronson, D., *Cross-linking of glycated collagen in the pathogenesis of arterial and myocardial stiffening of aging and diabetes.* J Hypertens, 2003. **21**(1): p. 3-12.

8. Nicolaas Westerhof, N.S., Mark I.M. Noble, *Snapshots of Hemodynamics: An Aid for Clinical Research and Graduate Education*. 2 ed. 2010, London: Springer.

9. Westerhof, N., N. Stergiopulos, and M.I.M. Noble, *Snapshots of hemodynamics : an aid for clinical research and graduate education*. Basic science for the cardiologist. 2005, New York, NY: Springer. xi, 192 p.

10. Lin, Y.T., Y.Z. Tseng, and K.C. Chang, *Aminoguanidine prevents fructose-induced arterial stiffening in Wistar rats: aortic impedance analysis.* Exp Biol Med (Maywood), 2004. **229**(10): p. 1038-45.

11. Kohen, R. and A. Nyska, *Oxidation of biological systems: oxidative stress phenomena, antioxidants, redox reactions, and methods for their quantification.* Toxicol Pathol, 2002. **30**(6): p. 620-50.

12. Ladisa, J.F., Jr., et al., *Microfocal X-ray computed tomography post-processing operations for optimizing reconstruction volumes of stented arteries during 3D computational fluid dynamics modeling.* Comput Methods Programs Biomed, 2005. **79**(2): p. 121-34.

13. CDC, *National diabetes fact sheet: general information and national estimates on diabetes in the United States.* 2011.

14. Goldfine, A.B. and J.A. Beckman, *Life and death in Denmark: lessons about diabetes and coronary heart disease.* Circulation, 2008. **117**(15): p. 1914-7.

15. Ryan, J. and D.J. Cohen, *Are drug-eluting stents cost-effective? It depends on whom you ask.* Circulation, 2006. **114**(16): p. 1736-43; discussion 1744.

16. Gilbert, J., J. Raboud, and B. Zinman, *Meta-analysis of the effect of diabetes on restenosis rates among patients receiving coronary angioplasty stenting.* Diabetes Care, 2004. **27**(4): p. 990-4.

17. Moses, J.W., et al., *Sirolimus-eluting stents versus standard stents in patients with stenosis in a native coronary artery.* N Engl J Med, 2003. **349**(14): p. 1315-23.

18. Hakim, D.A., et al., *Serial Gray Scale Intravascular Ultrasound Findings in Late Drug-Eluting Stent Restenosis.* Am J Cardiol, 2012.

19. Hioki, H., S. Kumazaki, and A. Izawa, *Critical In-stent Restenosis Following Fracture of Biolimus-Eluting Stent: A Report of 2 Cases.* J Invasive Cardiol, 2013. **25**(1): p. E11-3.

20. De la Torre Hernandez, J.M., et al., *Comparison of Paclitaxel-Eluting Stents (Taxus) and Everolimus-Eluting Stents (Xience) in Left Main Coronary Artery Disease With 3 Years Follow-Up (from the ESTROFA-LM Registry).* Am J Cardiol, 2012.

21. Stone, G.W., et al., *Differential clinical responses to everolimus-eluting and Paclitaxel-eluting coronary stents in patients with and without diabetes mellitus.* Circulation, 2011. **124**(8): p. 893-900.

22. Berry, C., J.C. Tardif, and M.G. Bourassa, *Coronary heart disease in patients with diabetes: part II: recent advances in coronary revascularization.* J Am Coll Cardiol, 2007. **49**(6): p. 643-56.

23. Kutryk, M.J., et al., *Local intracoronary administration of antisense oligonucleotide against c-myc for the prevention of in-stent restenosis: results of the randomized investigation by the Thoraxcenter of antisense DNA using local delivery and IVUS after coronary stenting (ITALICS) trial.* J Am Coll Cardiol, 2002. **39**(2): p. 281-7.

24. Dudek, D., et al., *L-arginine supplementation does not inhibit neointimal formation after coronary stenting in human beings: an intravascular ultrasound study.* Am Heart J, 2004. **147**(4): p. E12.

25. Peppa, M. and H. Vlassara, *Advanced glycation end products and diabetic complications: a general overview.* Hormones (Athens), 2005. **4**(1): p. 28-37.

26. Peppa, M., J. Uribarri, and H. Vlassara, *The role of advanced glycation end products in the development of atherosclerosis.* Curr Diab Rep, 2004. **4**(1): p. 31-6.

27. Vlassara, H. and M.R. Palace, *Diabetes and advanced glycation endproducts.* J Intern Med, 2002. **251**(2): p. 87-101.

28. Noh, H. and G.L. King, *The role of protein kinase C activation in diabetic nephropathy.* Kidney Int Suppl, 2007(106): p. S49-53.

29. Coughlan, M.T., J.M. Forbes, and M.E. Cooper, *Role of the AGE crosslink breaker, alagebrium, as a renoprotective agent in diabetes.* Kidney Int Suppl, 2007(106): p. S54-60.

30. Bakris, G.L., et al., *Advanced glycation end-product cross-link breakers. A novel approach to cardiovascular pathologies related to the aging process.* Am J Hypertens, 2004. **17**(12 Pt 2): p. 23S-30S.

31. Oldfield, M.D., et al., *Advanced glycation end products cause epithelial-myofibroblast transdifferentiation via the receptor for advanced glycation end products (RAGE).* J Clin Invest, 2001. **108**(12): p. 1853-63.

32. Stergiopulos, N., P. Segers, and N. Westerhof, *Use of pulse pressure method for estimating total arterial compliance in vivo.* American Journal of Physiology-Heart and Circulatory Physiology, 1999. **276**(2): p. H424-H428.

33. Alberti, K.G. and P.Z. Zimmet, *Definition, diagnosis and classification of diabetes mellitus and its complications. Part 1: diagnosis and classification of diabetes mellitus provisional report of a WHO consultation.* Diabet Med, 1998. **15**(7): p. 539-53.

34. Breen, D.M. and A. Giacca, *Effects of insulin on the vasculature.* Curr Vasc Pharmacol, 2011. **9**(3): p. 321-32.

35. Corradino, R.A., *Embryonic chick intestine in organ culture: interaction of adenylate cyclase system and vitamin D3-mediated calcium absorptive mechanism.* Endocrinology, 1974. **94**(6): p. 1607-14.

36. Carlos Lorenzo, M.O., Ken Williams, Michael P. Stern, Steven M. Haffner, *The Metabolic Syndrome as Predictor of Type 2 Diabetes.* Diabetes Care, 2003. **26**(11): p. 3153-3159.

37. Guyton, A., *Textbook of medical physiology*. 8 ed. 1991, Philadelphia: W B Saunders Co.

38. Zhang, Y., et al., *Positional cloning of the mouse obese gene and its human homologue.* Nature, 1994. **372**(6505): p. 425-32.

39. Zhang, F., et al., *Leptin: structure, function and biology.* Vitam Horm, 2005. **71**: p. 345-72.

40. Montague, C.T., et al., *Congenital leptin deficiency is associated with severe early-onset obesity in humans.* Nature, 1997. **387**(6636): p. 903-8.

41. ASSOCIATION, A.D., *Diagnosis and Classification of Diabetes Mellitus.* 2010.

42. Zhang, F., et al., *The rat model of type 2 diabetic mellitus and its glycometabolism characters.* Exp Anim, 2003. **52**(5): p. 401-7.

43. Fujimoto, W.Y., *The importance of insulin resistance in the pathogenesis of type 2 diabetes mellitus.* Am J Med, 2000. **108 Suppl 6a**: p. 9S-14S.

44. Roche, H.M., *Dietary carbohydrates and triacylglycerol metabolism.* Proc Nutr Soc, 1999. **58**(1): p. 201-7.

45. Kellerer, M. and H.U. Haring, *Pathogenesis of insulin resistance: modulation of the insulin signal at receptor level.* Diabetes Res Clin Pract, 1995. **28 Suppl**: p. S173-7.

46. Iozzo, P., et al., *Physiological hyperinsulinemia impairs insulin-stimulated glycogen synthase activity and glycogen synthesis.* Am J Physiol Endocrinol Metab, 2001. **280**(5): p. E712-9.

47. *Peripheral arterial disease in people with diabetes.* Diabetes Care, 2003. **26**(12): p. 3333-41.

48. Ratner, B.D., *Biomaterials Science: An Introduction to Materials in Medicine*. 2 ed. 2004, San Diego: Elsevier Academic Press.

49. Lin, W.C., C.H. Tseng, and M.C. Yang, *In-vitro hemocompatibility evaluation of a thermoplastic polyurethane membrane with surface-immobilized water-soluble chitosan and heparin.* Macromol Biosci, 2005. **5**(10): p. 1013-21.

50. Sarkar, S., et al., *Addressing thrombogenicity in vascular graft construction.* J Biomed Mater Res B Appl Biomater, 2007. **82**(1): p. 100-8.

51. Alahmar, A.E., et al., *Reduction in mortality and target-lesion revascularisation at 2 years: a comparison between drug-eluting stents and conventional bare-metal stents in the "real world".* Int J Cardiol, 2009. **132**(3): p. 398-404.

52. Martin, D.M. and F.J. Boyle, *Drug-eluting stents for coronary artery disease: a review.* Med Eng Phys, 2011. **33**(2): p. 148-63.

53. Farb, A., et al., *Pathological mechanisms of fatal late coronary stent thrombosis in humans.* Circulation, 2003. **108**(14): p. 1701-6.

54. Joner, M., et al., *Pathology of drug-eluting stents in humans: delayed healing and late thrombotic risk.* J Am Coll Cardiol, 2006. **48**(1): p. 193-202.

55. Stone, G.W., et al., *Safety and efficacy of sirolimus- and paclitaxel-eluting coronary stents.* N Engl J Med, 2007. **356**(10): p. 998-1008.

56. Chieffo, A., et al., *Histopathology of clinical coronary restenosis in drug-eluting versus bare metal stents.* Am J Cardiol, 2009. **104**(12): p. 1660-7.

57. Pfisterer, M.E., *Late stent thrombosis after drug-eluting stent implantation for acute myocardial infarction: a new red flag is raised.* Circulation, 2008. **118**(11): p. 1117-9.

58. van der Hoeven, B.L., et al., *Drug-eluting stents: results, promises and problems.* Int J Cardiol, 2005. **99**(1): p. 9-17.

59. Waksman, R., et al., *In vivo comparison of a polymer-free Biolimus A9-eluting stent with a biodegradable polymer-based Biolimus A9 eluting stent and a bare metal stent in balloon denuded and radiated hypercholesterolemic rabbit iliac arteries.* Catheter Cardiovasc Interv, 2011.

60. Lim, W.H., et al., *Stent coated with antibody against vascular endothelial-cadherin captures endothelial progenitor cells, accelerates re-endothelialization, and reduces neointimal formation.* Arterioscler Thromb Vasc Biol, 2011. **31**(12): p. 2798-805.

61. Sommer, C.M., et al., *Impact of stent design on in-stent stenosis in a rabbit iliac artery model.* Cardiovasc Intervent Radiol, 2010. **33**(3): p. 565-75.

62. Fishbein, I., et al., *Local delivery of gene vectors from bare-metal stents by use of a biodegradable synthetic complex inhibits in-stent restenosis in rat carotid arteries.* Circulation, 2008. **117**(16): p. 2096-103.

63. Indolfi, C., et al., *A new rat model of small vessel stenting.* Basic Res Cardiol, 2000. **95**(3): p. 179-85.

64. McMahon, A.C., H. Zreiqat, and H.C. Lowe, *Carotid artery stenting in the Zucker rat: a novel, potentially 'diabetes-specific' model of in-stent restenosis.* Diab Vasc Dis Res, 2008. **5**(2): p. 145-6.

65. Vermeersch, P., et al., *L-arginine administration reduces neointima formation after stent injury in rats by a nitric oxide-mediated mechanism.* Arterioscler Thromb Vasc Biol, 2001. **21**(10): p. 1604-9.

66. Oyamada, S., et al., *Trans-iliac rat aorta stenting: a novel high throughput preclinical stent model for restenosis and thrombosis.* J Surg Res, 2011. **166**(1): p. e91-5.

67. Salomaa, V., et al., *Non-insulin-dependent diabetes mellitus and fasting glucose and insulin concentrations are associated with arterial stiffness indexes. The ARIC Study. Atherosclerosis Risk in Communities Study.* Circulation, 1995. **91**(5): p. 1432-43.

68. Airaksinen, K.E., et al., *Diminished arterial elasticity in diabetes: association with fluorescent advanced glycosylation end products in collagen.* Cardiovasc Res, 1993. **27**(6): p. 942-5.

69. Lehmann, E.D., et al., *Non-invasive assessment of cardiovascular disease in diabetes mellitus.* Lancet, 1997. **350 Suppl 1**: p. SI14-9.

70. Peppa, M., J. Uribarri, and H. Vlassara, *Advanced glycoxidation. A new risk factor for cardiovascular disease?* Cardiovasc Toxicol, 2002. **2**(4): p. 275-87.

71. Ulrich, P. and A. Cerami, *Protein glycation, diabetes, and aging.* Recent Prog Horm Res, 2001. **56**: p. 1-21.

72. Thorpe, S.R. and J.W. Baynes, *Role of the Maillard reaction in diabetes mellitus and diseases of aging.* Drugs Aging, 1996. **9**(2): p. 69-77.

73. Wilmer Nichols, M.O.R., Charalambos Vlachopoulos, *McDonald's Blood Flow in Arteries*. 3 ed. 1990, Philadelphia: Lea & Febiger.

74. Tozzi, P., A. Corno, and D. Hayoz, *Definition of arterial compliance. Re: Hardt et al., "Aortic pressure-diameter relationship assessed by intravascular ultrasound: experimental validation in dogs.".* Am J Physiol Heart Circ Physiol, 2000. **278**(4): p. H1407.

75. Nicolaas Westerhof, N.S., Mark I.M. Noble, *snapshots of hemodynamics an aid for clinical research and graduate education*. 2005, New York: Springer.

76. Windberger, U., et al., *Whole blood viscosity, plasma viscosity and erythrocyte aggregation in nine mammalian species: reference values and comparison of data.* Exp Physiol, 2003. **88**(3): p. 431-40.

77. Rhodin, J.A., *The ultrastructure of mammalian arterioles and precapillary sphincters.* J Ultrastruct Res, 1967. **18**(1): p. 181-223.

78. Liu, Y., et al., *Endothelial cytoskeletal elements are critical for flow-mediated dilation in human coronary arterioles.* Med Biol Eng Comput, 2008. **46**(5): p. 469-78.

79. Waitkus-Edwards, K.R., et al., *alpha(4)beta(1) Integrin activation of L-type calcium channels in vascular smooth muscle causes arteriole vasoconstriction.* Circ Res, 2002. **90**(4): p. 473-80.

80. Haurani, M.J. and P.J. Pagano, *Adventitial fibroblast reactive oxygen species as autacrine and paracrine mediators of remodeling: bellwether for vascular disease?* Cardiovasc Res, 2007. **75**(4): p. 679-89.

81. Di Wang, H., et al., *Adventitial fibroblasts in vascular structure and function: the role of oxidative stress and beyond.* Can J Physiol Pharmacol, 2010. **88**(3): p. 177-86.

82. Bucala, R. and A. Cerami, *Advanced glycosylation: chemistry, biology, and implications for diabetes and aging.* Adv Pharmacol, 1992. **23**: p. 1-34.

83. Monnier, V.M., R.R. Kohn, and A. Cerami, *Accelerated age-related browning of human collagen in diabetes mellitus.* Proc Natl Acad Sci U S A, 1984. **81**(2): p. 583-7.

84. Cerami, A., H. Vlassara, and M. Brownlee, *Role of nonenzymatic glycosylation in atherogenesis.* J Cell Biochem, 1986. **30**(2): p. 111-20.

85. Monnier, V.M., V.J. Stevens, and A. Cerami, *Nonenzymatic glycosylation, sulfhydryl oxidation, and aggregation of lens proteins in experimental sugar cataracts.* J Exp Med, 1979. **150**(5): p. 1098-107.

86. Vishwanath, V., et al., *Glycation of skin collagen in type I diabetes mellitus. Correlation with long-term complications.* Diabetes, 1986. **35**(8): p. 916-21.

87. Stergiopulos, N., P. Segers, and N. Westerhof, *Use of pulse pressure method for estimating total arterial compliance in vivo.* Am J Physiol, 1999. **276**(2 Pt 2): p. H424-8.

88. Westerhof, N., G. Elzinga, and P. Sipkema, *An artificial arterial system for pumping hearts.* Journal of Applied Physiology, 1971. **31**(5): p. 776-81.

89. Figueroa, C.A., et al., *A coupled momentum method for modeling blood flow in three-dimensional deformable arteries.* Computer Methods in Applied Mechanics and Engineering, 2006. **195**(41-43): p. 5685-5706.

90. Vignon-Clementel, I.E., et al., *Outflow boundary conditions for three-dimensional finite element modeling of blood flow and pressure in arteries.* Computer Methods in Applied Mechanics and Engineering, 2006. **195**(29-32): p. 3776-3796.

91. Wesseling, P., *Principles of computational fluid dynamics*. Springer series in computational mathematics,. 2001, Berlin ; New York: Springer. xii, 644 p.

92. Chorin, A.J. and J.E. Marsden, *A mathematical introduction to fluid mechnanics, Universitext*. 1979, New York: Springer.

93. Langille, B.L. and F. O'Donnell, *Reductions in arterial diameter produced by chronic decreases in blood flow are endothelium-dependent.* Science, 1986. **231**(4736): p. 405-7.

94. Nikol, S., et al., *Expression of transforming growth factor-beta 1 is increased in human vascular restenosis lesions.* J Clin Invest, 1992. **90**(4): p. 1582-92.

95. Ward, M.R., et al., *Tranilast prevents activation of transforming growth factor-beta system, leukocyte accumulation, and neointimal growth in porcine coronary arteries after stenting.* Arterioscler Thromb Vasc Biol, 2002. **22**(6): p. 940-8.

96. Nabel, E.G., et al., *Direct transfer of transforming growth factor beta 1 gene into arteries stimulates fibrocellular hyperplasia.* Proc Natl Acad Sci U S A, 1993. **90**(22): p. 10759-63.

97. Yan, S.F., et al., *RAGE and its ligands: a lasting memory in diabetic complications?* Diab Vasc Dis Res, 2004. **1**(1): p. 10-20.

98. Wendt, T., et al., *Glucose, glycation, and RAGE: implications for amplification of cellular dysfunction in diabetic nephropathy.* J Am Soc Nephrol, 2003. **14**(5): p. 1383-95.

99. Prior, R.L. and G. Cao, *In vivo total antioxidant capacity: comparison of different analytical methods.* Free Radic Biol Med, 1999. **27**(11-12): p. 1173-81.

100. Berr, C., et al., *Enzymatic antioxidant balance and cognitive decline in aging--the EVA study.* Eur J Epidemiol, 2004. **19**(2): p. 133-8.

101. Mazur-Kolecka, B., et al., *The effect of oxidative stress on accumulation of apolipoprotein E3 and E4 in a cell culture model of beta-amyloid angiopathy (CAA).* Brain Res, 2003. **983**(1-2): p. 48-57.

102. Rinaldi, P., et al., *Plasma antioxidants are similarly depleted in mild cognitive impairment and in Alzheimer's disease.* Neurobiol Aging, 2003. **24**(7): p. 915-9.

103. Carbone, M.C., et al., *Antioxidant enzymatic defences in human follicular fluid: characterization and age-dependent changes.* Mol Hum Reprod, 2003. **9**(11): p. 639-43.

104. Meister, A. and M.E. Anderson, *Glutathione.* Annu Rev Biochem, 1983. **52**: p. 711-60.

105. Scholz, R.W., et al., *Mechanism of Interaction of Vitamin-E and Glutathione in the Protection against Membrane Lipid-Peroxidation.* Annals of the New York Academy of Sciences, 1989. **570**: p. 514-517.

106. Li, S.Y., et al., *Advanced glycation endproduct induces ROS accumulation, apoptosis, MAP kinase activation and nuclear O-GlcNAcylation in human cardiac myocytes.* Life Sci, 2007. **80**(11): p. 1051-6.

107. Wautier, M.P., et al., *Activation of NADPH oxidase by AGE links oxidant stress to altered gene expression via RAGE.* Am J Physiol Endocrinol Metab, 2001. **280**(5): p. E685-94.

108. Yan, C., et al., *Chronic high blood flow potentiates shear stress-induced release of NO in arteries of aged rats.* Am J Physiol Heart Circ Physiol, 2007. **293**(5): p. H3105-10.

109. Maritim, A.C., R.A. Sanders, and J.B. Watkins, 3rd, *Diabetes, oxidative stress, and antioxidants: a review.* J Biochem Mol Toxicol, 2003. **17**(1): p. 24-38.

110. Baynes, J.W., *Role of oxidative stress in development of complications in diabetes.* Diabetes, 1991. **40**(4): p. 405-12.

111. Baynes, J.W. and S.R. Thorpe, *Role of oxidative stress in diabetic complications: a new perspective on an old paradigm.* Diabetes, 1999. **48**(1): p. 1-9.

112. Ceriello, A., *Oxidative stress and glycemic regulation.* Metabolism, 2000. **49**(2 Suppl 1): p. 27-9.

113. Khan, R., A. Agrotis, and A. Bobik, *Understanding the role of transforming growth factor-beta1 in intimal thickening after vascular injury.* Cardiovasc Res, 2007. **74**(2): p. 223-34.

114. Basta, G., A.M. Schmidt, and R. De Caterina, *Advanced glycation end products and vascular inflammation: implications for accelerated atherosclerosis in diabetes.* Cardiovasc Res, 2004. **63**(4): p. 582-92.

115. Indolfi, C., et al., *Effects of balloon injury on neointimal hyperplasia in streptozotocin-induced diabetes and in hyperinsulinemic nondiabetic pancreatic islet-transplanted rats.* Circulation, 2001. **103**(24): p. 2980-2986.

116. Yoon, Y.W., et al., *Pathobiological role of advanced glycation endproducts via mitogen-activated protein kinase dependent pathway in the diabetic vasculopathy.* Exp Mol Med, 2008. **40**(4): p. 398-406.

117. Karau, K.L., et al., *Microfocal X-ray CT imaging and pulmonary arterial distensibility in excised rat lungs.* Am J Physiol Heart Circ Physiol, 2001. **281**(3): p. H1447-57.

118. Long, Q., et al., *Magnetic resonance image processing and structured grid generation of a human abdominal bifurcation.* Comput Methods Programs Biomed, 1998. **56**(3): p. 249-59.

119. Vasan, S., et al., *An agent cleaving glucose-derived protein crosslinks in vitro and in vivo.* Nature, 1996. **382**(6588): p. 275-8.

120. Asif, M., et al., *An advanced glycation endproduct cross-link breaker can reverse age-related increases in myocardial stiffness.* Proc Natl Acad Sci U S A, 2000. **97**(6): p. 2809-13.

121. Forbes, J.M., et al., *Advanced glycation end product interventions reduce diabetes-accelerated atherosclerosis.* Diabetes, 2004. **53**(7): p. 1813-23.

122. Freidja, M.L., et al., *The AGE-Breaker ALT-711 Restores High Blood Flow-Dependent Remodeling in Mesenteric Resistance Arteries in a Rat Model of Type 2 Diabetes.* Diabetes, 2012. **61**(6): p. 1562-72.

123. Pickavance, L., et al., *The development of overt diabetes in young Zucker Diabetic Fatty (ZDF) rats and the effects of chronic MCC-555 treatment.* Br J Pharmacol, 1998. **125**(4): p. 767-70.

124. Peterson RG, S.W., Neel M, Little LA, Eichberg J, *Zucker diabetic fatty rat as a model for noninsulindependent diabetes mellitus.* ILAR News, 1990. **32**: p. 16-19.

125. Leonard, B.L., et al., *Insulin resistance in the Zucker diabetic fatty rat: a metabolic characterisation of obese and lean phenotypes.* Acta Diabetol, 2005. **42**(4): p. 162-70.

126. Deuse, T., et al., *Imaging in-stent restenosis: an inexpensive, reliable, and rapid preclinical model.* J Vis Exp, 2009(31).

127. Garasic, J.M., et al., *Stent and artery geometry determine intimal thickening independent of arterial injury.* Circulation, 2000. **101**(7): p. 812-8.

128. G.L. Bakris, A.B., D.A. Kass, J. Neutel, R. Preston, *P-261: A clinical trial of an age cross-link breaker, alt-711, in systolic hypertension.* Am J Hypertens, 2004. **17**(S1): p. 127A-128A.

129. Kim, J.B., et al., *Alagebrium chloride, a novel advanced glycation end-product cross linkage breaker, inhibits neointimal proliferation in a diabetic rat carotid balloon injury model.* Korean Circ J, 2010. **40**(10): p. 520-6.

130. Candido, R., et al., *A breaker of advanced glycation end products attenuates diabetes-induced myocardial structural changes.* Circ Res, 2003. **92**(7): p. 785-92.

131. Wolffenbuttel, B.H., et al., *Breakers of advanced glycation end products restore large artery properties in experimental diabetes.* Proc Natl Acad Sci U S A, 1998. **95**(8): p. 4630-4.

132. Cooper, J.D., et al., *Evaluation of an osmotic pump for microdialysis sampling in an awake and untethered rat.* J Neurosci Methods, 2007. **160**(2): p. 269-75.

133. Newman, M.E., et al., *Chronic clomipramine alters presynaptic 5-HT(1B) and postsynaptic 5-HT(1A) receptor sensitivity in rat hypothalamus and hippocampus, respectively.* Neuropharmacology, 2000. **39**(12): p. 2309-17.

134. LaDisa, J.F., Jr., et al., *Stent implantation alters coronary artery hemodynamics and wall shear stress during maximal vasodilation.* J Appl Physiol, 2002. **93**(6): p. 1939-46.

135. Laskey, W.K., et al., *Estimation of total systemic arterial compliance in humans.* J Appl Physiol, 1990. **69**(1): p. 112-9.

136. Muller, J., et al., *Anisotropic adaptive finite element method for modelling blood flow.* Comput Methods Biomech Biomed Engin, 2005. **8**(5): p. 295-305.

137. Wendell, D.C., et al., *Including aortic valve morphology in computational fluid dynamics simulations: Initial findings and application to aortic coarctation.* Med Eng Phys, 2012.

138. LaDisa, J.F., Jr., et al., *Computational simulations for aortic coarctation: representative results from a sampling of patients.* J Biomech Eng, 2011. **133**(9): p. 091008.

139. Les, A.S., et al., *Quantification of hemodynamics in abdominal aortic aneurysms during rest and exercise using magnetic resonance imaging and computational fluid dynamics.* Ann Biomed Eng, 2010. **38**(4): p. 1288-313.

140. Hiramatsu, S., et al., *Improvement by aminoguanidine of insulin secretion from pancreatic islets grafted to syngeneic diabetic rats.* Biochem Pharmacol, 2000. **60**(2): p. 263-8.

141. Kass, D.A., et al., *Improved arterial compliance by a novel advanced glycation end-product crosslink breaker.* Circulation, 2001. **104**(13): p. 1464-70.

142. Puri, R.N. and A. Meister, *Transport of glutathione, as gamma-glutamylcysteinylglycyl ester, into liver and kidney.* Proc Natl Acad Sci U S A, 1983. **80**(17): p. 5258-60.

143. Jensen, G.L. and A. Meister, *Radioprotection of human lymphoid cells by exogenously supplied glutathione is mediated by gamma-glutamyl transpeptidase.* Proc Natl Acad Sci U S A, 1983. **80**(15): p. 4714-7.

144. Meister, A., *Selective modification of glutathione metabolism.* Science, 1983. **220**(4596): p. 472-7.

145. Leonardi, S., P. Tricoci, and K.W. Mahaffey, *Promises of PAR-1 inhibition in acute coronary syndrome.* Curr Cardiol Rep, 2012. **14**(1): p. 32-9.

146. Suzuki, H., B.W. Zweifach, and G.W. Schmid-Schonbein, *Vasodilator response of mesenteric arterioles to histamine in spontaneously hypertensive rats.* Hypertension, 1995. **26**(3): p. 397-400.

147. Bagher, P. and S.S. Segal, *The mouse cremaster muscle preparation for intravital imaging of the microcirculation.* J Vis Exp, 2011(52).

148. Michelson, A.D., *Platelets*. 2002.

149. Bakker, E.N., et al., *Differential structural adaptation to haemodynamics along single rat cremaster arterioles.* J Physiol, 2003. **548**(Pt 2): p. 549-55.

150. Homann, H.H., et al., *Influence of receptor antagonists, local anesthetics, and denervation on microcirculation.* Eplasty, 2011. **11**: p. e2.

151. Stefek, M., et al., *p-Dimethylaminobenzaldehyde-reactive substances in tail tendon collagen of streptozotocin-diabetic rats: temporal relation to biomechanical properties and advanced glycation endproduct (AGE)-related fluorescence.* Biochim Biophys Acta, 2000. **1502**(3): p. 398-404.

152. Taşkiran, D.T., E.; Yercan, H.; Kutay F.Z. , *Quantification total collagen in rabbit tendon by the sirius red.* Tr. J. of Medical Sciences, 1999(29): p. 7-9.

153. Vladic, N., et al., *Decreased tetrahydrobiopterin and disrupted association of Hsp90 with eNOS by hyperglycemia impair myocardial ischemic preconditioning.* Am J Physiol Heart Circ Physiol, 2011. **301**(5): p. H2130-9.

154. Bradford, M.M., *A rapid and sensitive method for the quantitation of microgram quantities of protein utilizing the principle of protein-dye binding.* Anal Biochem, 1976. **72**: p. 248-54.

155. Ferguson, R.E., et al., *Housekeeping proteins: A preliminary study illustrating some limitations as useful references in protein expression studies.* Proteomics, 2005. **5**(2): p. 566-571.

156. Kanwar, M. and R.A. Kowluru, *Role of glyceraldehyde 3-phosphate dehydrogenase in the development and progression of diabetic retinopathy.* Diabetes, 2009. **58**(1): p. 227-34.

157. Brownlee, M., *Advanced protein glycosylation in diabetes and aging.* Annu Rev Med, 1995. **46**: p. 223-34.

158. Morrison, T.M., et al., *Circumferential and longitudinal cyclic strain of the human thoracic aorta: age-related changes.* J Vasc Surg, 2009. **49**(4): p. 1029-36.

159. Yazdani, S.K., et al., *Atheroma and coronary bifurcations: before and after stenting.* EuroIntervention, 2010. **6 Suppl J**: p. J24-30.

160. LaDisa, J.F., Jr., et al., *Axial stent strut angle influences wall shear stress after stent implantation: analysis using 3D computational fluid dynamics models of stent foreshortening.* Biomed Eng Online, 2005. **4**: p. 59.

161. Jonas, M., et al., *Vascular neointimal formation and signaling pathway activation in response to stent injury in insulin-resistant and diabetic animals.* Circ Res, 2005. **97**(7): p. 725-33.

162. Indolfi, C., et al., *Effects of balloon injury on neointimal hyperplasia in streptozotocin-induced diabetes and in hyperinsulinemic nondiabetic pancreatic islet-transplanted rats.* Circulation, 2001. **103**(24): p. 2980-6.

163. Park, S.H., et al., *Neointimal hyperplasia after arterial injury is increased in a rat model of non-insulin-dependent diabetes mellitus.* Circulation, 2001. **104**(7): p. 815-9.

164. Pyles, J.M., et al., *Activation of MAP kinase in vivo follows balloon overstretch injury of porcine coronary and carotid arteries.* Circ Res, 1997. **81**(6): p. 904-10.

165. Schmidt, A.M., et al., *Isolation and characterization of two binding proteins for advanced glycosylation end products from bovine lung which are present on the endothelial cell surface.* J Biol Chem, 1992. **267**(21): p. 14987-97.

166. Neeper, M., et al., *Cloning and expression of a cell surface receptor for advanced glycosylation end products of proteins.* J Biol Chem, 1992. **267**(21): p. 14998-5004.

167. Cortizo, A.M., et al., *Advanced glycation end-products (AGEs) induce concerted changes in the osteoblastic expression of their receptor RAGE and in the activation of extracellular signal-regulated kinases (ERK).* Mol Cell Biochem, 2003. **250**(1-2): p. 1-10.

168. Kunt, T., et al., *Alpha-lipoic acid reduces expression of vascular cell adhesion molecule-1 and endothelial adhesion of human monocytes after stimulation with advanced glycation end products.* Clin Sci (Lond), 1999. **96**(1): p. 75-82.

169. Meerwaldt, R., et al., *The clinical relevance of assessing advanced glycation endproducts accumulation in diabetes.* Cardiovasc Diabetol, 2008. **7**: p. 29.

170. Cooper, M.E., *Importance of advanced glycation end products in diabetes-associated cardiovascular and renal disease.* Am J Hypertens, 2004. **17**(12 Pt 2): p. 31S-38S.

171. Schmidt, A.M., et al., *The biology of the receptor for advanced glycation end products and its ligands.* Biochim Biophys Acta, 2000. **1498**(2-3): p. 99-111.

172. Watson, A.M., et al., *Alagebrium reduces glomerular fibrogenesis and inflammation beyond preventing RAGE activation in diabetic apolipoprotein E knockout mice.* Diabetes, 2012. **61**(8): p. 2105-13.

173. Ramasamy, R., S.F. Yan, and A.M. Schmidt, *RAGE: therapeutic target and biomarker of the inflammatory response--the evidence mounts.* J Leukoc Biol, 2009. **86**(3): p. 505-12.

174. Yonekura, H., et al., *Novel splice variants of the receptor for advanced glycation end-products expressed in human vascular endothelial cells and pericytes, and their putative roles in diabetes-induced vascular injury.* Biochem J, 2003. **370**(Pt 3): p. 1097-109.

175. Raucci, A., et al., *A soluble form of the receptor for advanced glycation endproducts (RAGE) is produced by proteolytic cleavage of the membrane-bound form by the sheddase a disintegrin and metalloprotease 10 (ADAM10).* FASEB J, 2008. **22**(10): p. 3716-27.

176. Meister, A., *Transport and metabolism of glutathione and gamma-glutamyl amino acids.* Biochem Soc Trans, 1983. **11**(6): p. 793-4.

177. Langeveld, B., et al., *Rat abdominal aorta stenting: a new and reliable small animal model for in-stent restenosis.* J Vasc Res, 2004. **41**(5): p. 377-86.

178. Stegemann, H. and K. Stalder, *Determination of hydroxyproline.* Clin Chim Acta, 1967. **18**(2): p. 267-73.

179. Nordt, T.K., et al., *Augmentation of arterial endothelial cell expression of the plasminogen activator inhibitor type-1 (PAI-1) gene by proinsulin and insulin in vivo.* J Mol Cell Cardiol, 1998. **30**(8): p. 1535-43.

180. Murphy, L.J., A. Ghahary, and S. Chakrabarti, *Insulin regulation of IGF-I expression in rat aorta.* Diabetes, 1990. **39**(6): p. 657-62.

181. Marso, S.P., et al., *Optimizing the percutaneous interventional outcomes for patients with diabetes mellitus: results of the EPISTENT (Evaluation of platelet IIb/IIIa inhibitor for stenting trial) diabetic substudy.* Circulation, 1999. **100**(25): p. 2477-84.

182. Leonardi, S. and R.C. Becker, *PAR-1 inhibitors: a novel class of antiplatelet agents for the treatment of patients with atherothrombosis.* Handb Exp Pharmacol, 2012(210): p. 239-60.

183. Coughlin, S.R., *Protease-activated receptors in hemostasis, thrombosis and vascular biology.* J Thromb Haemost, 2005. **3**(8): p. 1800-14.

184. Ma, L., et al., *Proteinase-activated receptors 1 and 4 counter-regulate endostatin and VEGF release from human platelets.* Proc Natl Acad Sci U S A, 2005. **102**(1): p. 216-20.

185. Zania, P., et al., *Parstatin, the cleaved peptide on proteinase-activated receptor 1 activation, is a potent inhibitor of angiogenesis.* J Pharmacol Exp Ther, 2009. **328**(2): p. 378-89.

186. Mather, K.J., S. Verma, and T.J. Anderson, *Improved endothelial function with metformin in type 2 diabetes mellitus.* J Am Coll Cardiol, 2001. **37**(5): p. 1344-50.

187. Sirtori, C.R. and C. Pasik, *Re-evaluation of a biguanide, metformin: mechanism of action and tolerability.* Pharmacol Res, 1994. **30**(3): p. 187-228.

188. Kao, J., et al., *Relation of metformin treatment to clinical events in diabetic patients undergoing percutaneous intervention.* Am J Cardiol, 2004. **93**(11): p. 1347-50, A5.

189. Salpeter, S.R., et al., *Risk of fatal and nonfatal lactic acidosis with metformin use in type 2 diabetes mellitus.* Cochrane Database Syst Rev, 2010(4): p. CD002967.